Ken Vidar Falch

# High-energy X-ray Transmission Microscopy based on Compound Refractive Lenses

Ken Vidar Falch

Doctoral thesis

**NTNU**
Norwegian University of Science and Technology
Thesis for the Degree of
Philosophiae Doctor
Faculty of Natural Sciences
Department of Physics

**NTNU**
Norwegian University of
Science and Technology

**NTNU**
Norwegian University of
Science and Technology

NTNU

Ken Vidar Falch

# High-energy X-ray Transmission Microscopy based on Compound Refractive Lenses

**◻NTNU**

Norwegian University of
Science and Technology

# Acknowledgements

I consider myself fortunate to have had Prof. Ragnvald Mathiesen as my main supervisor. Ragnvald is one of the most patient, understanding, and reasonable people I know, and I sincerely appreciate the efforts he has for me over the past few years.

Thanks also to Marco De Michiel for sharing his extensive synchrotron knowledge and experience. It goes without saying that without his presence during experiments, things would have been a lot more difficult.

I appreciate Anatoly Snigirev for lessons, assistance and advice, and for granting me the opportunity to work at the ESRF. Irinia Snigireva have been very helpful with assistance on sample preparation and, of course, for putting the lenses in the lens box. I also thank Carsten Detlefs for support, discussion, and for keeping a tidy and functioning beam line. I am grateful to Maxim Polykarpov for showing me how to operate the beam line, and for company at the pub.

I have had the privilege of collaborating with Wajira Mirihanage and Daniele Casari. Lars Arnberg and Yanjun Li, who were my co-supervisors in my first year, have my gratitude as well.

Thanks also to Thomas Buslaps, Christian Morawe, Alexander Rack, Pierre Watterkamps, Veijo Honkimäki, and Pascal Thevenot for Technical assistance and facilitation.

Sender hilsener til min familie i Vardø: Cato, Katrine, Mamma, Pappa, Bestemor og bestefar i Vardø. Enda en hilsen går og ut til Bestemor og Bestefar i Oslo. Benjamin og Katariina skal jo selvsagt få hver sin hilsen de og. Tanter, onkler og søskenbarn må nok nøye seg med en felles hilsen, men jeg lover at jeg har husket på dere alle.

I deeply appreciate IGK for exotic conversation and exceptionally fruitless discussion.

# Abstract

In the results of the work presented in this thesis it has been shown theoretically and demonstrated experimentally that lateral chromatic aberration in hard X-ray transmission microscopy can be significantly reduced by focusing the illumination into the center of the objective lens. Utilizing pink beam microscopy, radiography with spatial resolutions better than 200 nm could be achieved at millisecond frame rates, and tomography with the same resolution could be acquired in less than two seconds.

Furthermore, Zernike phase contrast has been implemented for the first time in compound refractive lens based microscopy, and estimations are presented that indicates that the use of this phase contrast technique with non-monochromatic illumination is possible, and is compatible with the lateral chromatic correction scheme. It is also shown that with the illumination focused in the objective, Zernike phase contrast can be achieved using modified CRLs, exemplified by employing a lenslet with a circular hole as a negative phase plate. This is essential for pink beam imaging since the localization of a positive phase plate in the focal spot could become quite challenging, considering the focal spot heat load.

Demonstrations of both monochromatic and non-monochromatic imaging with HXTM are presented for various test cases, including in-situ eutectic solidification, colloidal crystals from micron sized polymer spheres, and ultra-fast high resolution tomogram data collections.

Taking into account the effects of partial coherent illumination chromatic transmission cross-coefficients have been derived, and expressions for optimal coherence lengths and numerical apertures for any bandwidth and resolution requirement, are obtained. In addition, some convenient relations between numerical aperture and longitudinal chromatic aberration have been derived linking the severity of chromatic aberration of compound refractive lenses to their numerical aperture. Finally, a modelling tool for fast evaluation of image quality was implemented and described.

# Preface

This thesis is submitted to the Norwegiean University of Science and Technology (NTNU) as partial fulfilment of the requirements for the degree of Philosophiae Doctor (Ph.D.). The work was carried out at the Department of Physics (IFY), at NTNU, from August 2013 to December 2016. The experimental work was conducted at The European Synchrotron Radiation Facility (ESRF).

The thesis consists of a collection of papers, preceded by an introduction to the necessary background knowledge.

# Papers Included in the Thesis

1. Ken Vidar Falch, Carsten Detlefs, Marco Di Michiel, Irina Snigireva, Anatoly Snigirev, and Ragnvald H. Mathiesen. Correcting lateral chromatic aberrations in non-monochromatic x-ray microscopy. *Applied Physics Letters*, 109 (5):054103, 2016. doi: doi:http://dx.doi.org/10.1063/1.4960193

2. K. V. Falch, M. Lyubomirskij, D. Casari, C. Detlefs, A. Snigirev, I. Snigireva, M. Di Michiel, and R. Mathiesen. Zernike phase contrast in high-energy x-ray transmission microscopy based on refractive optics. *Ultramicroscopy*, Under Review, 2016

3. Ken Vidar Falch, Daniele Casari, Marco Di Michiel, Carsten Detlefs, Anatoly Snigireva, Irina Snigireva, Veijo Honkimäki, and Ragnvald H. Mathiesen. In situ hard x-ray transmission microscopy for material science. *Journal of Materials Science*, 2016. ISSN 1573-4803. doi: 10.1007/s10853-016-0643-8

4. K. V. Falch, C. Detlefs, A. Snigirev, and R. Mathiesen. Analytical transmission cross-coefficients for pink beam x-ray microscopy based on compound refractive lenses. *Ultramicroscopy*, To be submitted, 2016

## Other publications

5. W. U. Mirihanage, K. V. Falch, I. Snigireva, A. Snigirev, Y. J. Li, L. Arnberg, and R. H. Mathiesen. Retrieval of three-dimensional spatial information from fast in situ two-dimensional synchrotron radiography of solidification microstructure evolution. *Acta Materialia*, 81:241–247, 2014. ISSN 1359-6454. doi: http://dx.doi.org/10.1016/j.actamat.2014.08.016

6. D. Casari, W. U. Mirihanage, K. V. Falch, I. G. Ringdalen, J. Friis, R. Schmid-Fetzer, D. Zhao, Y. Li, W. H. Sillekens, and R. H. Mathiesen. alpha-mg primary phase formation and dendritic morphology transition in solidification of a mg-nd-gd-zn-zr casting alloy. *Acta Materialia*, 116:177–187, 2016. ISSN 1359-6454. doi: 10.1016/j.actamat.2016.06.035

# Statement of Author contributions

## Paper 1

K. V. Falch conceived the idea for the experiments, and contributed to designing and planning the experiments, with the assistance of A. Snigirev, I. Snigireva, and C. Detlefs. The experiment was executed by K. V. Falch, M. D. Michiel, R. H. Mathiesen, and C. Detlefs. Data analysis and image processing was performed by K. V. Falch, and the manuscript was written by K. V. Falch, with the assistance of R. H. Mathiesen.

## Paper 2

The project was conceived and initiated by K. V. Falch, with the assistance of M. Lyuboriskij. Planning and designed of the experiment was done by K. V. Falch, with help from M. Lyuboriskij, and A. Snigirev. Preporatory work was done by K. V. Falch, M. Lyuboriskij, A. Snigirev, I. Snigireva, M. D. Michiel. The experiment was executed by K. V. Falch, A. Snigirev, I. Snigirev, D. Casari, C. Detlefs, and R. H. Mathiesen. The manuscript was written by K. V. Falch with the assistance of R. H. Mathiesen.

## Paper 3

The manuscript was written by K. V. Falch, with the assistance of D. Casari, and R. H. Mathiesen. Experimental results presented in the manuscript were mainly produced by K. V. Falch, M. D. Michiel, D. Casari, and R. H. Mathiesen, with assistance and facilitation by C. Detlefs, V. Honkimäki, I. Snigireva, and A. Snigirev.

## Paper 4

K. V. Falch initiated the project and carried out the analytical derivations. He also performed analysis of the implications of those derivations, as well as comparison of the theory with experimental data. The manuscript was written by K.V. Falch, with the assistance of R. H. Mathiesesn, and with suggestions and corrections from C. Detlefs. and A. Snigirev.

## Paper 5

The study was initiated by R. H. Mathiesen. Experiments were planned by R. H. Mathiesen and L. Arnberg, and carried out by R.H. Mathiesen, Y.J. Li, I. Snigireva and A. Snigirev. The analysis work was carried out by W. U. Mirihanage, with assistance from K.V. Falch and R.H. Mathiesen. The publication was written by W. U. Mirihanage with assistance from R.H. Mathiesen

## Paper 6

The study was planned and designed by D. Casari and R. H. Mathiesen. Experiments were carried out by D. Casari, W. U. Mirihanage, K.V. Falch, W. H. Silikens and R. H. Mathiesen. Thermodynamic calculations were done by R. Schmid-Fetzer, while DFT calculations were performed by I. Ringdalen, J. Friis, D. Zhao and Y.J. Li. The publication was written by D. Casari with assistance from R.H. Mathiesen.

# Contents

# List of Symbols

| | | |
|---|---|---|
| $c$ | - | Speed of light in vacuum. |
| $n$ | - | Refractive index. |
| $\psi$ | - | Scalar field. |
| $k$ | - | X-ray wavenumber. |
| $\lambda$ | - | X-ray wave length. |
| $t$ | - | time. |
| $\mathbf{r}$ | - | Position in 3-dimensional real space. |
| $x, y, z$ | - | Components of $\mathbf{r}$. |
| $\mathbf{k}$ | - | Position in 3-dimensional reciprocal space. |
| $k_x, k_y, k_z$ | - | Components of $\mathbf{k}$. |
| $\tilde{\psi}$ | - | Fourier transform of $\psi$. |
| $h(x, y)$ | - | Fresnel propagation kernel. |
| $H(k_x, K_y)$ | - | Fourier transform of the Fresnel propagation kernel, $h$. |
| $\alpha$ | - | Ratio of photon energy to a reference energy. |
| $\mathcal{F}$ | - | Fourier transform operator. |
| $\bar{\psi}(x, y, z)$ | - | envelope function, i.e. $\psi(x, y, z) = \bar{\psi}(x, y, z)\mathrm{e}^{ikz}$. |
| $\delta$ | - | Refractive index decrement. |
| $\beta$ | - | Imaginary part of refractive index. |
| $t(x, y)$ | - | Thickness function. |
| $S$ | - | Optical path length. |
| $\mathbf{x}$ | - | Vector containing the position and angle of a ray as its first and second component, respectively. |
| $w$ | - | Ray angle |
| $Q\,[c]$ | - | quadratic phase shift operator/matrix. |
| $R\,[d]$ | - | Propagation operator/matrix. |
| $\nu\mathcal{M}^{-1}$ | - | Scaling operator/matrix |
| $\mathcal{M}$ | - | magnification. |
| $p$ | - | Distance between the sample and the entrance plane of the objective CRL. |
| $q$ | - | Distance between Objective exit plane and detector. |

| | | |
|---|---|---|
| $S_{\mathrm{TL}}$ | - | Ray transfer matrix/operator for a thin lens microscope. |
| $f$ | - | The focal length of a single lens. |
| $\psi_i(x, y),$ | - | Scalar field in the image and object plane, respectively. |
| $\psi_o(x, y)$ | | |
| $\mathbf{r}_i, \mathbf{r}_o$ | - | 2 dimensional real space vector in the image and object plane, respectively. |
| $I_i(x, y), I_o(x, y)$ | - | 2 dimensional real space vector in the image and object plane, respectively. |
| $G(\mathbf{r_i}, \mathbf{r_o})$ | - | Greens function. |
| $\mathrm{PSF}(x, y)$ | - | Point spread function. |
| $\mathrm{LSF}(x)$ | - | Line spread function. |
| $\mathrm{ESF}(x)$ | - | Edge spread function. |
| $\mathbf{q}$ | - | 2-dimensional reciprocal space vector. |
| $\mathrm{MTF}(\mathbf{q})$ | - | Modulation transfer function. |
| $\mathrm{TCC}(\mathbf{q}', \mathbf{q}'')$ | - | Transmission cross-coefficients. |
| $f(\mathbf{r})$ | - | Complex transmission function. |
| $F(\mathbf{q})$ | - | Fourier transform of the complex sample transmission function. |
| $P(\mathbf{q})$ | - | Pupil function. |
| $J(\mathbf{q})$ | - | Angular source distribution in terms of spatial frequencies. |
| $R$ | - | Apex radius of a refractive lenslet. |
| $R_0$ | - | Radius of the geometrical aperture of a refractive lenslet. |
| $T$ | - | Thickness of a lenslet. |
| $T_w$ | - | Web thickness of a lenslet. |
| $F$ | - | Back foical length. |
| $L$ | - | Total length of a CRL. |
| $\omega$ | - | Parameter that describes the refractive power density of a CRL. |
| $M_{\mathrm{CRL}}$ | - | Ray transfer for propagation through a CRL. |
| $S_{\mathrm{CRL}}$ | - | Ray transfer matrix for CRL microscope. |
| $L_{F=0}$ | - | The CRL length that makes the back focal length equal to zero. |
| $L_{\mathrm{max}}$ | - | The CRL length that for a given $q$ places the object plane at the CRL entrance plane i.e. it sets $p = 0$. |
| N.A. | - | Numerical aperture. |
| $\theta_m$ | - | Marginal ray angle. |
| $A_{\mathrm{eff}}$ | - | Effective aperture. |
| $\mu$ | - | Linear attenuation constant. |
| $N$ | - | Number of lenslets in a CRL. |
| $t_0$ | - | transmission through lenslet web. |
| $t(x, w)$ | - | Transmission of a ray through an optical system. |
| $O$ | - | Matrix related to attenuation in a lenslet. |
| $\gamma$ | - | Ratio between complex part of the refractive index and the refractive index decrement, i.e. $\beta/\delta$. |
| $\Sigma$ | - | Matrix describing attenuation of a ray through a CRL. |
| $\Sigma_o$ | - | Matrix describing attenuation of a ray through a CRL microscope. |

| | | |
|---|---|---|
| $\sigma_{\mathrm{N.A.}}$ | - | R.m.s. numerical aperture in units of radians. |
| $D_a$ | - | Aperture diameter. |
| $\rho$ | - | Diffraction limited resolution. |
| $w_{\mathrm{opt}}(x_o)$ | - | Ray angle that maximizes transmission through an optical system at from initial position $x_o$. |
| $g$ | - | Distance from the sample at which the illumination comes to a focus, disregarding the objective lens. |
| $g_{\mathrm{ideal}}$ | - | Value of $g$ that optimizes transmission of the illumination through the optical system. |
| $\mathcal{B}(\mathcal{E})$ | - | Source brilliance. |
| $\Delta\Omega$ | - | Bending magnet radiation cone angle. |
| $\sigma_x, \sigma_y$ | - | R.m.s. source size in horizontal and vertical direction, respectively. |
| $\sigma_{\theta_x}, \sigma_{\theta_y}$ | - | R.m.s. divergence in horizontal and vertical direction, respectively. |
| $B$ | - | Magnetic field. |
| $\nu$ | - | Radiation frequency. |
| $\nu_c$ | - | The critical frequency of bending magnet radiation. |
| $\nu_n$ | - | Radiation frequency of the $n$th harmonic. |
| $\mathcal{P}$ | - | Radiated power. |
| $\lambda_u$ | - | Undulator period. |
| $\bar{\beta}$ | - | Average electron velocity along the optical axis, in units of $c$. |
| $K$ | - | Ratio between maximum angle of electron path with respect to the optical axis, and the bending magnet radiation cone angle. |
| $e$ | - | Electron charge. |
| $m_e$ | - | Electron mass. |
| $\varepsilon_e$ | - | Energy of an orbiting electron, including rest energy. |
| $S(\mathbf{k})$ | - | Spatio-temporal Fourier transform the lattice of times and locations at which the electron passes a magnet pair, evaluated at frequency $\nu = ck$. |
| $\zeta_{\mathrm{D}}$ | - | Darwin width. |
| $r_0$ | - | Classical electron radius. |
| $v_c$ | - | Crystal unit cell volume. |
| $F_{\mathbf{h}}$ | - | Structure factor of unit cell at reciprocal lattice vector h. |
| $j$ | - | Integer indicating harmonic number. |
| $\theta_j$ | - | Angle of $j$th harmonic reflection. |
| $\Lambda$ | - | Multilayer period. |
| $\tau$ | - | Time delay. |
| $\mathbf{r}_1, \mathbf{r}_2$ | - | 2-dimensional real space vector in the observation plane. |
| $\Gamma(\mathbf{r}_1, \mathbf{r}_2, \tau)$ | - | Mutual coherence function. |
| $\tilde{\Gamma}(\mathbf{r}_1, \mathbf{r}_2, \nu)$ | - | Cross-spectral density. |
| $\tilde{\Gamma}_o(\mathbf{r}_1, \mathbf{r}_2, \nu)$, $\tilde{\Gamma}_s(\mathbf{r}_1, \mathbf{r}_2, \nu)$ | - | Cross-spectral density in object- and source plane, respectively. |
| $U_i(z_o, z_s, \nu)$ | - | The propagation operator that advances the field from $z_s$ to $z_o$. |
| $\mu_\nu(\mathbf{r}_1, \mathbf{r}_2)$ | - | Complex coherence factor. |

| | | |
|---|---|---|
| $\boldsymbol{\xi}$ | - | 2-dimensional vector in the source plane. |
| $I_{s,\nu}(\boldsymbol{\xi})$ | - | Intensity in the source plane at frequency $\nu$. |
| $l_c$ | - | Coherence length. |
| DQE | - | Detective quantum efficiency. |
| SNR | - | Signal to noise ratio. |
| $\eta_{\mathrm{abs}}$ | - | Fraction of x-ray photons absorbed scintillator. |
| $\eta_{\mathrm{col}}$ | - | Fraction of visible light photons that reach the pixel array. |
| $E_x, E_v$ | - | Energy of x-ray and visible light photon, respectively. |
| $\eta_{x/v}$ | - | Fraction of x-ray energy converted to visible light. |
| $\eta_{v/e}$ | - | Average number of electrons per visible light photon. |
| $r$ | - | Detector resolution. |
| $t_s$ | - | Scintillator thickness. |
| $t_{s,opt}$ | - | Optimal scintillator thickness. |
| $f(x,y)$ | - | Function to be reconstructed. |
| $p_\theta(\xi)$ | - | Projection of $f$ at angle $\theta$. |
| $\xi, \eta$ | - | Coordinates along the axis perpendicular and parallel to the direction of projection, respectively. |
| $h$ | - | Filter kernel for the filtered back projection algorithm. |
| $\tilde{h}$ | - | Filter function in the filtered back projection algorithm. |
| $I_\theta(\xi)$ | - | Intensity of x-ray projection image. |
| $I_0(\xi)$ | - | Intensity of incident beam. |
| $\psi'(x,y)$ | - | scalar field immediately downstream of sample. |
| $\psi_{\mathrm{BG}}(x,y)$ | - | Background scalar field. |
| $\psi_{\mathrm{SC}}(x,y)$ | - | Scalar field scattered by sample. |
| $\Delta\delta, \Delta\beta$ | - | Deviation from the mean value of $\delta$ and $\beta$. |
| $\phi$ | - | Phase shift induced by phase plate. |
| $R_q$ | - | Radius of region in reciprocal space affected by the phase plate. |
| $\lambda_{\mathrm{fringe}}$ | - | Period of ringing artefact. |
| $d$ | - | Defocus distance. |
| $E_0$ | - | In-focus reference energy. |
| $\omega_0$ | - | In-focus reference frequency. |
| $\Delta\alpha$ | - | Deviation of $\alpha$ from 1, i.e. $\Delta\alpha = \alpha - 1$. |
| $\sigma_\alpha$ | - | R.m.s. value of relative bandwidth. |
| $\sigma_d$ | - | R.m.s. value of distribution of defocus. |
| $I_{\mathrm{f}}$ | - | Transmitted intensity through a feature to be detected. |
| $n_p x$ | - | Number of pixels making up the feature to be detected. |
| $I_{\mathrm{bg}}$ | - | Background intensity. |
| $\sigma_n$ | - | R.m.s. of noise. |
| $v$ | - | Feature visibility. |
| $t_e$ | - | Camera exposure time. |
| CNR | - | Contrast to noise ratio. |
| $P_o$ | - | Point in the object plane of the system. |
| $P_i, P_i'$ | - | Original and perturbed image point of $P_o$. |
| $W, W'$ | - | Wave front of original and perturbed system, respectively |
| $\Phi$ | - | Optical path length along the rays connecting $W$ and $W'$. |

| | | |
|---|---|---|
| $\kappa$ | - | Tangent point of $W$ and $W'$, and minimum of $\Phi$. |
| $\rho_{\mathrm{CRL}}$ | - | CRL material density ($\frac{x^2}{R}$ inside the CRL). |
| $O'$ | - | Matrix related to the amount of phase shift imposed by a lenslet. |
| $V$ | - | Matrix related to the amount of phase shift imposed by the CRL on a ray originating from the CRL entrance plane. |
| $V_o$ | - | Matrix related to the amount of phase shift imposed by the CRL on a ray originating from the object plane. |
| $A, B, C, D$ | - | Elements of a ray transfer matrix. |

**Part I**

# Introduction

# Chapter 1

# Motivation

With the constant advance of materials to meet with increasingly stringent and specific demands, more attention is shifted to multi-scale and multiphase materials. Gradually, increasing focus has been given to control material structure on the mesoscopic scale, with characteristic lengths ranging from nanometers to micrometers. This is typically a spatiotemporal domain that connects ab-initio models to continuum models. Experiments on the mesoscopic scale are vital for the guiding and validation of simulation models, and of particular relevance for successful linking of models working at different scales. Ultimately, such experiments are essential to understand the physics behind the processes in question.

An important example of such is eutectic metal microstructure formation. Eutectic microstructure can be classified into various categories, such as lamellar, rods, platelets, fibers, and regular/irregular, depending on both the appearance of the structures and the process through which they form. Significant research efforts have been made into refining the microstructure to smaller characteristic length scales in order to improve ductility while at the same time preserving strength [63]. Ultra-fine eutectics may turn out to be a very promising route for production of superplastic materials that could be cast directly into various shapes. The most important eutectic systems, in terms of commercial market share, are Al-Si and Fe-C. These are both irregular eutectics, meaning that one of the phases involved grows faceted. Accurate theoretical models for irregular eutectics do not currently exist due to the complexity of the system [6]. Only the simplest of eutectic solidification scenarios, namely regular, near isothermal directional solidification, can be described adequately theoretically by the existing Jackson Hunt model [36] and extenstions to it [44, 45]. The matter becomes even more complicated if more than two phases are to be considered.

The study of eutectic microstrucure is also of great interest in the development of lead free soldering alloys. The most widely used soldering alloy is the lead based Sn–Pb alloy, however, the Pb content of soldering alloys has become restricted by legislation in the European union (RoHS2 and WEEE), mainly due to its toxicity. In response to this, Pb-free soldering alloys, such as Sn-based [77], and Bi based alloys [20] have received increased attention. Successful soldering depends on several factors. Aside from being economically viable, the alloy needs to adequately wet the metal surfaces commonly encountered in electronics, and have a suitable melting temperature. In addition to this, the mechanical integrity of the final soldering result is of critical importance. A very important determinant of the mechical integrity is the interface microstructure. A good understanding of the reaction dynamics near the interface is crucial to achieve the desired result reliably. In-situ observation of the actual formation of the interface microstructure is therefore potentially very interesting [7, 83, 32].

Another interesting area of research is the study of colloidal particle systems. Colloidal particles are of interest to several research fields such as soft matter [48], biology [65], photonic crystals [59], and fundamental solidification science [85]. Many experiments have been performed using visible-light confocal microscopy [67, 68, 81], but it is desirable to be able to improve the resolution beyond the visible light wavelength limit. Given the 3-dimensional nature of many colloid systems, the capability to do tomographic imaging is an advantage. While confocal microscopy can provide some depth information, being able to do proper full resolution rapid tomograms would open up new avenues for experimental in-situ investigation.

These are just a few examples of science cases where 2 and 3D time-resolved microscopy with mesoscale spatial resolution would be of major importance. The linking between first principle based and continuum based models is a rather general challenge in materials science, and would apply to most scenarios involving phase transitions of any kind or material response to external physical fields (mechanical, thermal, electromagnetic, etc.). Typically, phase transitions propagates in systems departed from thermodynamic equilibrium, often with a spatiotemporally varying phase front where attachment kinetics, heat- and mass transport conditions across the interface are local, and ultimately decisive for the final material microstructure that forms. The ability to perform time resolved in situ microscopy at the most relevant spatiotemporal scales set by the transport dynamics and transformation kinetics is of high relevance across the field.

X-radiography would be a reasonable approach to conducting in-situ experiments of the processes mentioned above, if not for the fact that state-of-the-art detectors for X-radiography and tomography experiments consist of a thin transparent

scintillator that converts X-rays to visible light, and a visible light microscope that casts a magnified image of the scintillator onto a CCD or CMOS array. Hence, the nominal spatial resolution is, at best, comparable to that of optical microscopy. Sub-optical resolution can be obtained by increasing the magnification with an X-ray microscope that casts an image of the sample onto the scintillator.

The construction of a hard X-ray microscope at the ID6 beamline at the ESRF has opened up the field of Hard X-ray Transmission Microscopy (HXTM). Although X-ray microscopes in the soft- and intermediate X-ray regime are available [18, 84], HXTM is the first full field transmission microscope operating with 100 nm resolution at X-ray energies above 15 keV [74].

Spatial resolution is always relevant when it comes to microscopy, but another challenge is posed by the time scale of the phenomena to be studied. This is especially true for tomography, which requires longer total exposure time compared to single image radiography. This thesis introduces pink beam microscopy as a possible solution to this problem. Until now, microscopy based on CRLs has been conducted exclusively with monochromatic beams. The monochromatic beam is produced by filtering down the beam produced by undulators or bending magnets, typically with a crystal monochromator. It is possible to increase temporal resolution by forgoing the monochromator, and instead use a full undulator harmonic as illumination. Broadening the bandwidth, however, begs the question: To what extent will chromatic aberration affect image quality? The focus of this thesis will be on how to best exploit the increased bandwidth by minimizing the loss of spatial resolution, and maximizing the gain in temporal resolution for pink beam microscopy.

Another important factor for temporal resolution is contrast. A common method of optimizing absorption contrast is to use photon energies just above an absorption edge of the sample material. However, as increased absorption implies more beam induced heating damage, using an absorption edge may not be a solution for all case studies with pink beam microscopy. The fact that phase modulation induced by samples on X-rays is much stronger than the amplitude modulation, constitutes a good argument to adapt some of the many phase contrast techniques already popular in other branches of microscopy to HXTM. The present thesis will explore the possibility of applying the well-known Zernike Phase Contrast technique to CRL microscopy.

# Chapter 2

# Fundamental X-ray Optics

This chapter will introduce the relevant fundamentals of optical systems. At the heart of optics is the propagation of electromagnetic waves, and closely related to waves is the concept of rays. A short description of the relevant theory of wave propagation will be made, followed by a description of rays and ray transfer matrices (RTMs) as they apply to microscopes based on refractive optics. It will also be shown how wave propagation and RTMs may be combined via operator notation. Another important concept related to waves is the notion of coherence. This chapter will also present the basic principle of coherence, as well as the Van Cittert-Zernike theorem, which is an important tool for intuitive understanding of how the photon source influences coherence. Finally, once coherence have been described, the concept of transfer functions will be described and defined. Transfer functions functions are very useful for optimization of microscopes.

## 2.1  Wave propagation

As electromagnetic waves, X-rays obey Maxwell's equations. While the electromagnetic field is vectorial, each orthogonal component behaves according to the d'Alambert equation [9]

$$\left(\nabla^2 - \frac{n^2}{c^2}\frac{\partial^2}{\partial t^2}\right)\psi(\mathbf{r}, t) = 0, \tag{2.1}$$

where $\psi$ is a scalar field, $c$ is the speed of light in vacuum and $n$ is the refractive index of the medium in which the wave is propagating. For a monochromatic wave in vacuum, (2.1) is reduced to the Helmholtz equation

$$\left(\nabla^2 + k^2\right)\psi(\mathbf{r}) = 0. \tag{2.2}$$

with solutions on the form

$$\psi(\mathbf{r}) = \int_W \tilde{\psi}(\mathbf{k})e^{i\mathbf{kr}}\mathrm{d}^2\mathbf{k}, \tag{2.3}$$

where $\tilde{\psi}(\mathbf{k})$ is an arbitrary complex function, and $W$ is a spherical surface with radius $|\mathbf{k}| = k$. It is useful to define an optical axis, which here is labelled as the $z$-axis. If $\psi(x, y, z)$ is known in a plane defined by $z = 0$, then

$$\psi(x, y, \Delta z) = \int_W \tilde{\psi}(\mathbf{k})e^{ik_z\Delta z}e^{i\mathbf{kr}}\mathrm{d}^2\mathbf{k}. \tag{2.4}$$

Using the small angle approximation,

$$k_z = \sqrt{k^2 - k_x^2 - k_y^2} \approx k - \frac{k_x^2 + k_y^2}{2k}, \tag{2.5}$$

in (2.4) yields

$$\psi(x, y, z_1 + \Delta z) \approx e^{ik\Delta z} \int \tilde{\psi}(k_x, k_y)H(k_x, k_y)e^{ik_x x + ik_y y}\mathrm{d}k_x\mathrm{d}k_y, \tag{2.6}$$

where

$$H(k_x, k_y) = e^{-\frac{i\Delta z}{2k}\left(k_x^2 + k_y^2\right)}. \tag{2.7}$$

Note that changing the value of $k$ to $\alpha k$ would be equivalent to changing the propagation distance from $\Delta z$ to $\Delta z/\alpha$. The form of (2.6) is computationally convenient because it represents propagation in terms of Fourier transforms and multiplications. Using $\mathcal{F}$ to symbolize the Fourier transform operation in the $xy$-plane, (2.6) can be written as

$$\psi(x, y, z_1 + \Delta z) = e^{ik\Delta z}\mathcal{F}^{-1}H\mathcal{F}\psi(x, y, 0) \tag{2.8}$$

Another convenient representation of propagation can be obtained by applying the convolution theorem to (2.8). By substituting

$$h(x, y) = \mathcal{F}^{-1}H(k_x, k_y) = \frac{ik}{2\pi\Delta z}e^{\frac{ik}{2\Delta z}\left(x^2 + y^2\right)} \tag{2.9}$$

into (2.8), one obtains:

$$\psi(x, y, z_1 + \Delta z) = e^{ik\Delta z}\left(h * \psi(x, y, 0)\right) \tag{2.10}$$

$$= \frac{ike^{ik\Delta z}}{2\pi\Delta z}e^{\frac{ik}{2\Delta z}\left(x^2+y^2\right)}\int \psi(x', y')e^{\frac{ik}{2\Delta z}\left(x'^2+y'^2\right)}e^{-\frac{ik}{2\Delta z}\left(xx'+yy'\right)}\mathrm{d}x'\mathrm{d}y' \tag{2.11}$$

Like (2.6), this can be expressed as a sequence of multiplication and Fourier transform operations, but with (2.11), only one numerical Fourier transform is needed.

## 2.2   X-ray interaction with bulk material

In the small angle approximation, already made in (2.5), propagation through an inhomogeneous medium can be modelled by the inhomogeneous paraxial equation [61].

$$2ik\frac{\partial}{\partial z}\bar{\psi}(x,y,z) = \left[\nabla_\perp^2 + k^2(n^2(x,y,z) - 1)\right]\bar{\psi}(x,y,z) \qquad (2.12)$$

where $\bar{\psi}(x,y,z)$ is an envelope function defined so that $\psi(x,y,z) = \bar{\psi}(x,y,z)\mathrm{e}^{ikz}$, and $\nabla_\perp$ is the Laplace operator in the xy-plane. X-ray interaction with a sample is often modelled sufficiently well with the so-called projection approximation, where one assumes that the inhomogeneous medium is sufficiently thin along the optical axis so that any change in $\bar{\psi}$ due to propagation can be neglected. This is equivalent to suspending the $\nabla_\perp^2$-term in (2.12). Letting $\psi(x,y,z)$ and $\psi'(x,y,z)$ be the field, immediately upstream and downstream of the refracting object, respectively, the projection approximation yields

$$\psi'(x,y,z) = \mathrm{e}^{-\frac{ik}{2}\int\left(1-n^2(x,y,z)\right)\mathrm{d}z}\psi(x,y,z). \qquad (2.13)$$

When considering imaging with X-rays, (2.13) provides a useful tool for modelling the effect of a sample in the path of the beam. As the refractive index for X-rays is close to 1, it is common to express it

$$n = 1 - \delta + i\beta, \qquad (2.14)$$

and use the approximation $1 - n^2 \approx 2\delta - 2i\beta$ [61]. If the object is homogenous, with a thickness $t(x,y)$ along the optical axis, (2.13) may be expressed as

$$\psi'(x,y) = \mathrm{e}^{-ik(\delta-i\beta)t(x,y)}\psi(x,y). \qquad (2.15)$$

## 2.3   Rays and Ray Transfer Matrices

The concept of rays is a very useful and flexible tool for reasoning about optical systems, particularly when refractive optical elements are involved. In order to describe rays, it is necessary first to define the optical path length

$$S = \int_C n(s)\mathrm{d}s \qquad (2.16)$$

where the integral is along the path $C$. A ray is defined by Fermat's principle as the curve that minimizes $S$, i.e. the path that satisfies [11]

$$\delta S = 0 \qquad (2.17)$$

where $\delta S$ is a virtual displacement. For a paraxial optical system, considering only 1 dimension to simplify notation, a ray has a transversal position, $x$, and forms an angle $w$ with the optical axis for any given value of $z$, To simplify further, $x$ and $w$ can be combined into a vector

$$\mathbf{x} = \begin{pmatrix} x \\ w \end{pmatrix}. \tag{2.18}$$

A major reason for the utility of the ray picture are ray transfer matrices (RTMs). In a paraxial system, the transformation of $\mathbf{x}$ along the optical axis can be described by multiplying $\mathbf{x}$ with an RTM. The most important RTMs for X-ray optics are the free space propagation matrix $R(d)$, where $d$ is the distance propagated along the optical axis, and $Q\left(-\frac{1}{f}\right)$, which represents refraction by a lens with focal length $f$.

$$R(d) = \begin{bmatrix} 1 & d \\ 0 & 1 \end{bmatrix}, \tag{2.19}$$

$$Q\left(-\frac{1}{f}\right) = \begin{bmatrix} 1 & 0 \\ -\frac{1}{f} & 1 \end{bmatrix} \tag{2.20}$$

It will also be useful to define the scaling matrix,

$$\nu\left(\mathcal{M}^{-1}\right) = \begin{bmatrix} \mathcal{M} & 0 \\ 0 & \mathcal{M}^{-1} \end{bmatrix}, \tag{2.21}$$

which multiplies the position of a ray with $\mathcal{M}$, and multiplies the angles by $\mathcal{M}^{-1}$. The utility of RTMs lies in that they can be combined to form new RTMs representing larger systems. For example, a microscope consisting of a thin lens, placed a distance $p$ from the sample plane, and a distance $q$ from a camera can be represented by

$$S_{\mathrm{TL}} = R(q)Q\left(-\frac{1}{f}\right)R(p) = \begin{bmatrix} 1 - \frac{q}{f} & pq\left(\frac{1}{p} + \frac{1}{q} - \frac{1}{f}\right) \\ -\frac{1}{f} & 1 - \frac{p}{f} \end{bmatrix} \tag{2.22}$$

The microscope is said to be in imaging condition when $S_{\mathrm{TL},1,2} = 0$. When that is the case, all rays intersecting a point $x_i$ on the input plane of the system will congregate at $x_o = S_{\mathrm{TL},1,1}x_i$ in the output plane. This also suggests that $S_{\mathrm{TL},1,1}$ can be regarded as the magnification of the system. In a paraxial imaging system, all rays can be expressed as a linear combination of the principle and marginal ray. In order to define these two special rays, it is necessary to define the field stop and

aperture stop. The field stop limits the real space area of the sample that will be permitted through the optical system, while the aperture stop defines the angular acceptance from the sample plane. The marginal ray passes through the center of the field stop, and touches the edge of the aperture stop, while the principle ray is defined as the ray that starts at the edge of the field stop, and passes through the center of the aperture stop.

The aperture stop of the CRL microscope is not necessarily determined by an actual pinhole or pair of slits. If the pupil function is Gaussian, then the aperture stop is effectively defined by absorption in the CRL. In this case of CRLs, the principle ray will be defined as the ray emanating from the edge of the field stop that suffers the least attenuation.

## 2.4   Operators

A potent approach to studying optical systems is through the operator notation presented by Nazrathy and Shamir. [49, 50, 51, 30, 52, 53]. In this work, three operators, representing propagation, quadratic phase-shift, and scaling will be used. The propagation operator is denoted $R\,[d]$. It represents a convolution of the input field $\psi$, with the empty space propagator of the monochromatic wave equation.

$$R\,[d]\,\psi(x) = \left(\frac{k}{i2\pi d}\right)^{\frac{1}{2}} \int \psi(x') \exp\left(i\frac{k}{2d}(x-x')^2\right) \mathrm{d}x'. \qquad (2.23)$$

The quadratic phase-shift operator is denoted $Q\,[c]$, and is simply a multiplication of the input field with an exponential function.

$$Q\,[c]\,\psi(x) = \exp\left(\frac{1}{2}ickx^2\right)\psi(x). \qquad (2.24)$$

The scaling operator is represented by $\nu\,[t]$, and defined as

$$\nu\,[t]\,\psi(x) = \psi(tx). \qquad (2.25)$$

Note that $|t| > 1$ corresponds to de-magnification, while $|t| < 1$ corresponds to magnification. Many interesting relationships between these operators are tabulated in [53]. However, only one identity will be needed here, namely

$$R\,[d]\,Q\,[c] = Q\left[\left(c^{-1}+d\right)^{-1}\right]\nu\left[\left(1+cd\right)^{-1}\right]R\left[\left(c+d^{-1}\right)^{-1}\right]. \qquad (2.26)$$

Comparing (2.26) to (3.1), it is clear that the effect of a lenslet with focal length $f$ can be represented by $Q\left[-\frac{1}{f}\right]$, if absorption is ignored. The operator for a

thin lens microscope, $S_{\text{TLM}}$, can be synthesized from the above operators in the following way:

$$S_{\text{TLM}} = R\,[q]\,Q\left[-\frac{1}{f}\right]R\,[p] \tag{2.27}$$

Making use of (2.26), (2.27) can be rewritten as

$$S_{\text{TL}} = Q\left[\frac{1}{q-f}\right]\nu\left[\left(1-\frac{q}{f}\right)^{-1}\right]R\left[p - \left(\frac{1}{f}-\frac{1}{q}\right)^{-1}\right] \tag{2.28}$$

It is evident that the microscope can be thought of as free-space propagating the field a distance (0 if in focus), followed by a magnification, and applying a quadratic phase shift. More generally, if a system of lenses can be represented by the a ray transfer matrix,

$$M = \begin{bmatrix} A & B \\ C & D \end{bmatrix}, \tag{2.29}$$

The output field, $\psi'$, as given in [50][1] becomes

$$\psi' = Q\left[\frac{C}{A}\right]\nu\left[\frac{1}{A}\right]R\left[\frac{B}{A}\right]\psi, \tag{2.30}$$

where $\psi$ is the input field. Thus, for any system represented by an RTM, the magnification of the system is

$$\mathcal{M} = A, \tag{2.31}$$

and the argument of the propagation operator, which will be referred to as the defocus distance, is

$$d = \frac{B}{A}. \tag{2.32}$$

In this chapter, $A$, $B$, $C$, and $D$ was assumed to be real numbers. A real CRL microscope may in fact be more accurately represented by complex numbers. See Appendix B for more on this topic.

## 2.5   Coherence

Coherence plays an important role in X-ray microscopy. Consider the image of two point objects separated by the distance $\Delta x$. Let $\psi_1$ and $\psi_2$ be the signal on the image plane produced by the two points, individually. The intensity in the image plane is

$$I_i(\mathbf{r}) = \langle\psi_1(\mathbf{r},t)^*\psi_1(\mathbf{r},t)\rangle + \langle\psi_2(\mathbf{r},t)^*\psi_2(\mathbf{r},t)\rangle + 2\text{Re}\left(\langle\psi_2(\mathbf{r},t)^*\psi_1(\mathbf{r},t)\rangle\right) \tag{2.33}$$

---

[1]There are several ways to represent the system. This is one out of four fundamental representation given in [50].
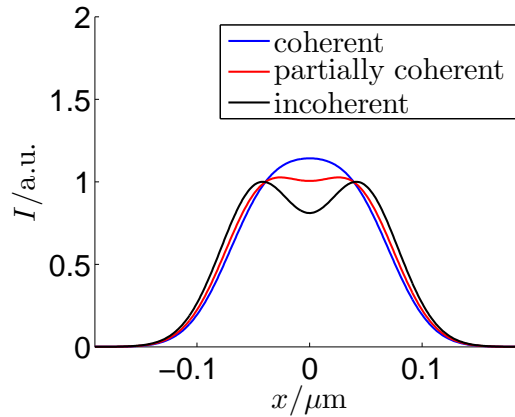
**Figure 2.1:** Illustration of effect of coherence on resolution.

The two first terms on the right hand side is simply the individual intensity images, while the third term is an interference term. If the two signals $\psi_1(t)$ and $\psi_2(t)$ are uncorrelated, i.e. the interference term is 0, the image is incoherent, whereas it is coherent if they are perfectly correlated. Anything in between these two extremes is partial coherence. The effect of coherence on the image contrast is illustrated in Figure 2.1.

It is common to describe coherence in terms of the mutual coherence function. Let $\psi(\mathbf{r}, t)$ be a time dependent, but statistically stationary signal. The mutual coherence function is defined as

$$\Gamma(\mathbf{r}_1, \mathbf{r}_2, \tau) = \langle \psi(\mathbf{r}_1, t)^* \psi(\mathbf{r}_2, t + \tau) \rangle \tag{2.34}$$

where $\langle \psi(\mathbf{r}_1, t)^* \psi(\mathbf{r}_2, t+\tau) \rangle$ is the expected value of $\psi(\mathbf{r}_1, t)^* \psi(\mathbf{r}_2, t+\tau)$, which under the assumption of ergodicity is also the time average. In the context of polychromatic X-ray microscopy, it is more useful to consider the cross-spectral density function, which is the spectral transform of the mutual coherence function.

$$\tilde{\Gamma}(\mathbf{r}_1, \mathbf{r}_2, \nu) = \int \Gamma(\mathbf{r}_1, \mathbf{r}_2, \tau) e^{-i\nu\tau} d\tau. \tag{2.35}$$

This function has the property that it obeys a pair of Helmholtz equations [60]

$$\left(\nabla_1^2 + k^2\right) \tilde{\Gamma}(\mathbf{r}_1, \mathbf{r}_2, \nu) = 0 \tag{2.36}$$

$$\left(\nabla_2^2 + k^2\right) \tilde{\Gamma}(\mathbf{r}_1, \mathbf{r}_2, \nu) = 0 \tag{2.37}$$

$$, \tag{2.38}$$

where the $\nabla_i^2$-operator is with respect to the argument $\mathbf{r}_i$. If the cross spectral density at the source plane is $\tilde{\Gamma}_s(\mathbf{r}_1, \mathbf{r}_2, \nu)$, then at the observation plane, $z = z_0$, it will be

$$\tilde{\Gamma}_o(\mathbf{r}_1, \mathbf{r}_2, \nu) = U_1(z_o, z_s, \nu) U_2(z_o, z_s, \nu) \tilde{\Gamma}_s(\mathbf{r}_1, \mathbf{r}_2, \nu) \qquad (2.39)$$

where $U_i(z_o, z_s, \nu)$ is the propagation operator that advances the field from $z_s$ to $z_o$. It is sometimes convenient to describe coherence in terms of the complex coherence factor,

$$\mu_\nu(\mathbf{r}_1, \mathbf{r}_2) = \frac{\tilde{\Gamma}(\mathbf{r}_1, \mathbf{r}_2, \nu)}{\sqrt{I(\mathbf{r}_1) I(\mathbf{r}_2)}}. \qquad (2.40)$$

## 2.5.1   The Van Cittert-Zernike Theorem

In the special case when the source can be considered as a collection of incoherent point sources, and the source plane is far enough from observation plane that the Greens function may be approximated by plane waves, the spectral density at the observation plane is

$$\tilde{\Gamma}_o(\mathbf{r}_1, \mathbf{r}_2, \nu) = \frac{k^2}{4\pi^2 \Delta z^2} \int I_{s,\nu}(\boldsymbol{\xi}) \, e^{\frac{ik}{\Delta z} \boldsymbol{\xi} \boldsymbol{\Delta r}} d^2 \boldsymbol{\xi} \qquad (2.41)$$

where $I_{s,\nu}(\boldsymbol{\xi}) = \tilde{\Gamma}_s(\boldsymbol{\xi}, \boldsymbol{\xi}, \nu)$ is the intensity in the source plane at frequency $\nu$, $\Delta z$ is the distance between the source and observation planes, $\boldsymbol{\xi}$ refers to position in the source plane, and $\boldsymbol{\Delta r} = \mathbf{r}_1 - \mathbf{r}_2$. This is the Van Cittert-Zernike theorem [86][2], and is often given in terms of angles as

$$\tilde{\Gamma}_o(\mathbf{r}_1, \mathbf{r}_2, \nu) = \int I_{s,\nu}(w_x, w_y) \, e^{ik(w_x \Delta x + w_y \Delta y)} dw_x dw_y \qquad (2.42)$$

where $w_x$ and $w_y$ are angles, and $I_{s,\nu}(w_x, w_y)$ is the intensity of the point source at position $\Delta z w_x \hat{x} + \Delta z w_y \hat{y}$. The right hand side of (2.42) can be regarded as the Fourier transform of the angular intensity distribution.

## 2.5.2   The Generalized Van Cittert-Zernike Theorem

Rather than assuming that the source consists of independent point sources, the so-called Generalized Van Cittert-Zernike Theorem [31, 15] takes partial coherence into account by modelling the source as quasi-homogeneous. A quasi-homogeneous source is a partially coherent source whose intensity distribution remains fairly

---

[2]The Van Cittert-Zernike theorem is often written for the mutual intensity function, $J(\mathbf{r}_1, \mathbf{r}_2) = \Gamma(\mathbf{r}_1, \mathbf{r}_2, 0)$, rather than the cross spectral density. However, as the propagation rules for the cross-spectral density is the same as for the mutual intensity, it applies to both [31].

constant over distances comparable to the coherence length. Accordingly it's cross spectral density can be expressed as

$$\tilde{\Gamma}_s(\mathbf{r}_1, \mathbf{r}_2) = I_{s,\nu}(\bar{\boldsymbol{\xi}}, \nu)\mu_{s,\nu}\left(\boldsymbol{\Delta\xi}\right), \tag{2.43}$$

with $\boldsymbol{\Delta\xi} = \boldsymbol{\xi}_2 - \boldsymbol{\xi}_1$, and $\bar{\boldsymbol{\xi}} = \left(\boldsymbol{\xi}_2 + \boldsymbol{\xi}_1\right)/2$, where $\boldsymbol{\xi}_1$ and $\boldsymbol{\xi}_2$ are the positions of two points in the source plane. When this is the case, the cross-spectral density in the observation plane

$$\tilde{\Gamma}_o(\mathbf{r}_1, \mathbf{r}_2, \nu) = \frac{k^2 e^{-\frac{ik}{2\Delta z}\left(|\mathbf{r}_2|^2 - |\mathbf{r}_1|^2\right)}}{4\pi^2\Delta z^2}\kappa_\nu(\bar{\mathbf{r}})\int I_{s,\nu}\left(\bar{\boldsymbol{\xi}}\right)e^{-\frac{ik}{\Delta z}\boldsymbol{\Delta}\mathbf{r}\bar{\boldsymbol{\xi}}}d^2\bar{\boldsymbol{\xi}} \tag{2.44}$$

where

$$\kappa_\nu(\bar{\mathbf{r}}) = \int \mu_{s,\nu}\left(\boldsymbol{\Delta\xi}\right)e^{-\frac{ik}{\Delta z}\boldsymbol{\Delta\xi}\bar{\mathbf{r}}}d^2\boldsymbol{\Delta\xi}. \tag{2.45}$$

## 2.6   Transfer functions

As an optical imaging system will have finite N.A., not all spatial frequencies will be permitted through the system. This results in a blurring of the image. The amount defines the resolution of the system. In the coherent case, the field amplitude in the image plane, $\psi_i$, is linear in terms of the object plane amplitude, $\psi_o$, and may accordingly be expressed

$$\psi_i = \int G(\mathbf{r}_i, \mathbf{r}_o)\psi_o(\mathbf{r}_o)d^2\mathbf{r}_o, \tag{2.46}$$

where $G(\mathbf{r}_i, \mathbf{r}_o)$ is the Greens function of the system. If $G(\mathbf{r}_i, \mathbf{r}_o)$ can be expressed as $G(\mathbf{r}_i/\mathcal{M} - \mathbf{r}_o)$, the system is said to be shift invariant.

In the case of incoherent illumination, the image will be linear in intensity, and one may express it

$$I_i = \int \text{PSF}(\mathbf{r}_i/\mathcal{M} - \mathbf{r}_o)I_o(\mathbf{r}_o)d^2\mathbf{r}_o, \tag{2.47}$$

where $\text{PSF}(\mathbf{r}) = |G(\mathbf{r})|^2$ is the intensity point spread function. The PSF can be thought of as the image of a point object. Similarly, the line spread function (LSF), and edge spread function (ESF) are the resulting images of lines and edges, respectively. A convenient way of writing (2.47) is

$$\mathcal{F}\left[I_i\right](\mathbf{q}) = \text{MTF}(\mathbf{q})\mathcal{F}\left[I_o(\mathbf{r}_o)\right](\mathbf{q}), \tag{2.48}$$

Where $\text{MTF}(\mathbf{q}) = \mathcal{F}\left[\text{PSF}(\mathbf{r})\right](\mathbf{q})$ is the modulation transfer function.

In the case of partial coherence, a topic that will be revisited later, neither of (2.46) and (2.47) are correct, and it may be necessary to express the image intensity in terms of the transmission cross-coefficients (TCC) [35, 10], as follows:

$$I_i(\mathbf{r}) = \int \int \mathrm{TCC}(\mathbf{q}', \mathbf{q}'') F(\mathbf{q}') F(\mathbf{q}'')^* \mathrm{e}^{-i\boldsymbol{\Delta}\mathbf{q}\mathbf{r}} \mathrm{d}^2 \boldsymbol{\Delta}\mathbf{q} \mathrm{d}^2 \bar{\mathbf{q}} \tag{2.49}$$

$$\mathrm{TCC}(\mathbf{q}', \mathbf{q}'') = \int J(\mathbf{q}) P(\mathbf{q} + \mathbf{q}') P(\mathbf{q} + \mathbf{q}'')^* \mathrm{d}^2 \mathbf{q} \tag{2.50}$$

where $J(\mathbf{q})$ relates to the angular extension of the source, $P$ is the pupil function, $\boldsymbol{\Delta}\mathbf{q} = \mathbf{q}' - \mathbf{q}''$, $\bar{\mathbf{q}} = (\mathbf{q}' + \mathbf{q}'')/2$, and $F(\mathbf{q}) = \mathcal{F}[f(\mathbf{r})](\mathbf{q})$, with $f(\mathbf{r})$ as the complex sample transmission function. The application of (2.49) and (2.50) to CRL-based X-ray microscopy is investigated in Paper 4 [25].

# Chapter 3

# Compound Refractive Lenses

This chapter will briefly justify the choice to use CRLs, as opposed to other types of optical components. It will then define some CRL parameters and provide some useful equations. From there on, the Numerical Aperture (N.A.) of a CRL will be discussed in terms of ray paths, and connected to the so-called Rayleigh Criterion. The conditions of optimal transmission will also be presented using the same ray paths formalism. Finally, a vary brief discussion on the optimal CRL geometry for maximum resolution.

## 3.1   Choice of X-ray optics

There are three main categories of X-ray optics, namely reflective, diffractive, and refractive.

A strength of reflective optics is that they are achromatic, and can achieve resolution below 50 nm [46]. A drawback is the difficulty of alignment. A microscope based on reflective optics is not easily reconfigured.

Diffractive lenses, i.e. Fresnel zone plates, can achieve very high resolution, however, due to the necessary aspect ratio of structures it becomes difficult to produce efficient zone plates for high photon energies. Fresnel zone plates become problematic at photon energies above 15 keV, and are therefore not a feasible choice for HXTM. It is worth mentioning that in the future, so-called multilayer Laue lenses could be a solution to this problem. With Multilayer Laue lenses, spatial resolution in the range of 15-50 nm could potentially be obtained[55, 57, 54].

Refractive optical elements, although currently limited in terms of resolution to about 100 nm [74], have the strength of being efficient and flexible. All experi-
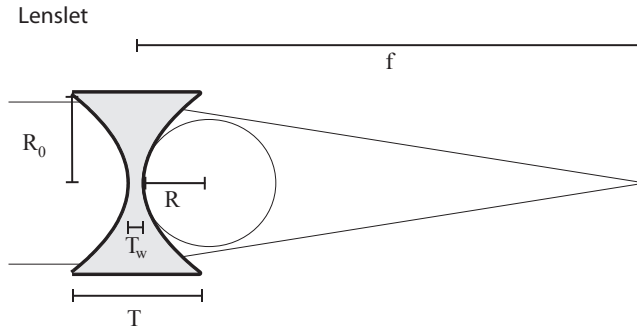
Lenslet



**Figure 3.1:** Illustration of Lenslet.
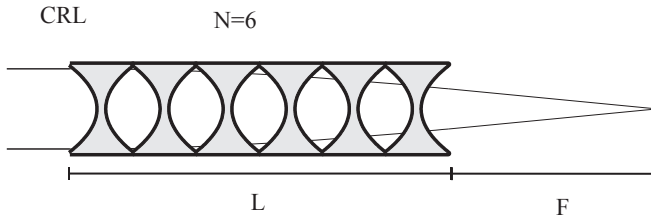
CRL

N=6



**Figure 3.2:** Illustration of CRL.

ments included as part of this thesis was based on refractive optical elements, and for this reason, the introduction will cover only refractive optics.

## 3.2    Definitions and fundamental formulas

A refractive lens is a lens that relies on refraction, as opposed to diffraction or reflection, to redirect rays. A single lenslet, as illustrated in Figure 3.1, has thickness, $T$, an apex radius of curvature, $R$, and a physical aperture $R_0$. A double concave parabolic lenslet has a thickness function $t(x, y) = (x^2 + y^2)/R$, where $R$ is the apex radius of curvature. Using (2.15), the interaction of the field with a lenslet is

$$\psi'(x, y) = \mathrm{e}^{-ik\frac{(\delta - i\beta)}{R}(x^2 + y^2)}\psi(x, y) = \mathrm{e}^{\frac{1}{2}ik\left[-\frac{1}{f}\right](x^2 + y^2)}\psi(x, y), \qquad (3.1)$$

where

$$f = \frac{R}{2\delta} \qquad (3.2)$$

is the focal length of the lenslet. As $\delta$ is small, a single lenslet will typically have a long focal length. To reduce the focal length, several lenslets can be compounded

together into a compound refractive lens (CRL). A CRL has a number of lenslets, $N$, and a length $L$, as illustrated in Figure 3.2. Several approximations to the focal length of the CRL have been derived [43, 70], but as a first approximation, one can imagine the CRL as a number of thin lenslets superimposed on each other, i.e. the CRL is still imagined to be flat. In that case, the focal length, $F$, of the CRL is

$$F \approx \frac{R}{2\delta N},$$
(3.3)

This approximation is valid when the length of the CRL is small compared to $F$. While (3.3) may be sufficient for the majority of experiments where CRLs are involved, there are good reasons to take a closer look at the paths of rays propagating through a CRL. An effective approach is to use RTMs. It can be shown [72] that the RTM for a ray propagating from the entrance of a CRL to the exit on the other side, is

$$M_{\text{CRL}} = \begin{bmatrix} \cos\left(\omega L\right) & \frac{\sin(\omega L)}{\omega} \\ -\omega \sin\left(\omega L\right) & \cos\left(\omega L\right) \end{bmatrix},$$
(3.4)

where $L$ is the length of the CRL, and $\omega$ is a parameter related to the lens geometry and material by $\omega = (fT)^{-\frac{1}{2}}$. The RTM for a microscope, as in (2.22), but using a CRL rather than a flat lens, is

$$S_{\text{CRL}} = R(q)M_{\text{CRL}}R(p) = \cos(\omega L) \begin{bmatrix} 1 - \frac{q}{F} & pq\left(\frac{1}{q} + \frac{1}{p} + \frac{1}{pqF\omega^2} - \frac{1}{F}\right) \\ -\frac{1}{F} & 1 - \frac{p}{F} \end{bmatrix}$$
(3.5)

where $F$ is the back focal length[1], as illustrated in Figure 3.2, and is given by

$$F = \frac{1}{\omega \tan(\omega L)},$$
(3.6)

From (3.5) it is evident that the imaging condition for the CRL microscope is

$$\frac{1}{q} + \frac{1}{p} + \frac{1}{pqF\omega^2} - \frac{1}{F} = 0$$
(3.7)

and that the magnification is

$$\mathcal{M} = \cos(\omega L)\left(1 - \frac{q}{F}\right) = \cos(\omega L) - \omega q \sin(\omega L).$$
(3.8)

---

[1]Not to be confused with the effective focal length, $F_e = \frac{1}{\omega \sin(\omega L)}$ [71], which is the distance between the focal plane and the principle plane.

If the CRL is long enough, the back focal plane will be on the exit plane, or even inside the CRL. It is practical to know the length $L_{F=0}$ where the back focal plane coincides with the exit plane. According to (3.6), the back focal length goes to zero when

$$\omega L_{F=0} = \frac{\pi}{2}.$$
(3.9)

This is already an impractically long lens. However, it is still not the longest possible lens that can be used for imaging. For a given $q$, the maximum length is implicitly given by

$$\omega L_{\max} = \frac{\pi}{2} + \tan^{-1}\left(\frac{1}{\omega q}\right).$$
(3.10)

### 3.2.1   Numerical aperture

The numerical aperture of an optical system is defined as

$$\text{N.A.} = n\sin(\theta_m),$$
(3.11)

where $n$ is the index of refraction in the medium surrounding the sample, and $\theta_m$ is the angle between the marginal ray and the optical axis. As $n$ for X-rays is usually close to 1 regardless of medium, and angles are small enough that the small angle approximation can be used without concern, (3.11) can be reduced to $\text{N.A.} = \theta_m$. In X-ray microscopy, the N.A. is primarily of interest to estimate resolution.

The aperture of the CRL is not necessarily determined by the physical aperture, but by the absorption in the periphery of the lens, where the X-rays have to pass through more material. This gives rise to the notion of the effective aperture, $A_{\text{eff}}$[43]. $A_{\text{eff}}$ is the corresponding circular aperture diameter that will transmit the same total intensity as the CRL, regarding the CRL as a thin object.

$$A_{\text{eff}} = 2R_0\sqrt{\frac{1 - e^{-\mu NT}}{\mu NT}},$$
(3.12)

It will, however, be of interest to investigate the transmission through the CRL more closely. The following derivations are heavily based on derivations by Heugh et al. [72]. Consider the transmission function, $t$, of a ray passing through a single double concave lenslet of infinitesimal thickness $dz$,

$$t = t_0 e^{-\frac{\mu}{RT}x^2\,dz}$$
(3.13)

where $\mu$ is the linear attenuation coefficient of the lens material, $x$ is the position where the ray intersects the lens plane, and

$$t_0 = e^{-\mu T_w}.$$
(3.14)

It will be convenient to express the exponent in terms of matrices

$$t = t_0 e^{-\frac{1}{2}\mathbf{x}'^\top O \mathbf{x}' \mathrm{d}z} \tag{3.15}$$

where $\mathbf{x}'$ is the ray vector at the lens plane and

$$O = \begin{bmatrix} \frac{\mu}{RT} & 0 \\ 0 & 0 \end{bmatrix}. \tag{3.16}$$

Now imagine that the infinitesimal lens is one of many slices of a continuous CRL at position $z$ along the optical axis, with the opening of the CRL at $z = 0$. Let $M_{\mathrm{CRL}}(z)$ be the RTM corresponding to propagation from the CRL opening to $z = z'$. Then one can make the substitution $\mathbf{x}' = M_{\mathrm{CRL}}(z)\mathbf{x}$, where $\mathbf{x}$ is the ray vector at the opening of the CRL.

$$t = t_0 e^{-\frac{1}{2}\mathbf{x}^\top M_{\mathrm{CRL}}(z')^\top O M_{\mathrm{CRL}}(z') \mathbf{x} \mathrm{d}z} \tag{3.17}$$

As the total transmission can be found by multiplying $t$ for all slices that constitutes the CRL, the exponent of the total transmission will be the integral over the exponents of the slices. This yields

$$t(x, w) = t_0^N e^{-\frac{1}{2}\mathbf{x}^\top \mathbf{\Sigma}^{-1}\mathbf{x}}, \tag{3.18}$$

where the matrix in the exponent is given by

$$
\begin{aligned}
\mathbf{\Sigma}^{-1} &= \int_0^L M_{\mathrm{CRL}}(z')^\top O M_{\mathrm{CRL}}(z') \mathrm{d}z' \\
&= k\gamma \begin{bmatrix} \omega\left(\omega L + \cos\left(\omega L\right)\sin\left(\omega L\right)\right) & \sin\left(\omega L\right)^2 \\ \sin\left(\omega L\right)^2 & \frac{\omega L - \cos(\omega L)\sin(\omega L)}{\omega} \end{bmatrix}
\end{aligned} \tag{3.19}
$$

where $\gamma = \beta/\delta$, and the relation $\mu = 2k\beta$ have been used. Here the integral in (3.19) is to be performed over each matrix element separately. Finally, it is desirable to relate the transmission to ray vectors $\mathbf{x}_o$ at the object plane of a microscope. Substituting $\mathbf{x} = R(p)\mathbf{x}_o$ yields

$$t(x, w) = t_0^N e^{-\frac{1}{2}\mathbf{x}_o^\top \mathbf{\Sigma}_o^{-1}\mathbf{x}_o}, \tag{3.20}$$

$$\mathbf{\Sigma}_o^{-1} = R(p)^\top \mathbf{\Sigma}^{-1} R(p). \tag{3.21}$$

Figure 3.3 shows the transmission for different $\mathbf{x}_o$. The numerical aperture is related to the angular acceptance of the system, which corresponds to the horizontal width of the Gaussian. This implies that the numerical aperture is only determined by the $-\frac{1}{2}\Sigma_{o,2,2}^{-1}w_o^2$-term in the exponent in (3.20), and thus given by

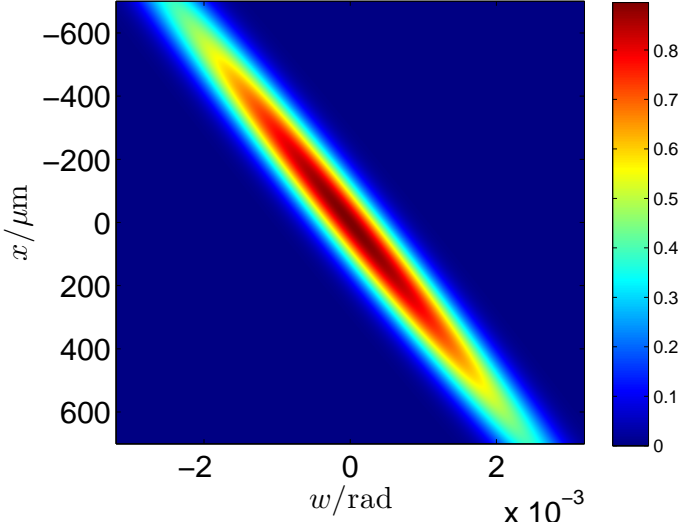$$\sigma_{\mathrm{N.A.}}^2 = \frac{1}{\Sigma_{o,2,2}^{-1}} \tag{3.22}$$

**Figure 3.3:** Transmission as a function of $x$ and $w$, calculated by (3.21). The calculation was performed for a system of 90 Be lenses with $R = 50$ $\mu$m, $T = 1.6$ mm, $T_w = 30$ $\mu$m, $E = 17$ keV, $p = 0.2$ m, and $q = 3$ m.

### 3.2.2   Optimal transmission

Returning to Figure 3.3, it is clear that the transmission of a ray depends, not only the angle, but also the initial position of the ray. In X-ray CRL microscopy this can be significant as the effective aperture of the lens is comparable to the field of view. Naturally the transmission will be higher when the ray passes through less absorbing parts in the center of the lens. By focusing the illumination at a particular distance, $g$, downstream of the sample, the relationship $gw_o = x_o$ will be imposed on incoming parallel rays, ignoring partial coherence and scattering by the sample. The ray angle $w_{\text{opt}}(x_o)$ that optimizes the transmission can be found by minimizing the exponent in (3.20) with respect to $w_o$.

$$w_{\text{opt}}(x_o) = -\frac{\boldsymbol{\Sigma}_{o,1,2}^{-1}}{\boldsymbol{\Sigma}_{o,2,2}^{-1}} x_o. \tag{3.23}$$

The value of $g$ that optimizes the transmission is

$$\frac{1}{g_{\text{ideal}}} = \frac{w_{\text{opt}}(x_o)}{x_o} = -\frac{\boldsymbol{\Sigma}_{o,1,2}^{-1}}{\boldsymbol{\Sigma}_{o,2,2}^{-1}}. \tag{3.24}$$

While focusing at $g_{\text{ideal}}$ improves the transmission in the whole field of view, the effect is most dramatic in the periphery, where transmission would be close to zero

with a parallel beam, but remains appreciable under ideal focusing. This could be taken to suggest that the field of view is larger under ideal focusing, compared to parallel illumination, but in practice, the FOV usually ends up being smaller than the parallel beam FOV due to the limited aperture of the upstream focusing lens.

### 3.2.3 The Rayleigh Criterion

The Rayleigh criterion defines the diffraction limited resolution of an optical system in terms of its PSF. The PSF of a monochromatic imaging system with a circular aperture of diameter $D_a$ is called an Airy disc. The Airy disc has a central peak, surrounded by rings of minima and maxima. The Rayleigh criterion for resolution defines that two points are resolvable if the central peak of Airy discs are separated by more than the radius of the ring of the first minimum. By this definition, the diffraction limited resolution, $\rho$, of the imaging system is given by [3]

$$\rho = \frac{0.61\lambda}{\text{N.A.}}, \tag{3.25}$$

The PSF of an X-ray CRLs is not an Airy pattern, but has a Gaussian shape. This is true, even when the length of the CRL is taken into account [72]. As $\sigma_{\text{N.A.}}$ is the root mean square of the Gaussian aperture in units of radians, the standard deviation of the field amplitude in Fourier space is

$$\sigma_q = \sqrt{2}k\sigma_{\text{N.A.}} \tag{3.26}$$

The r.m.s. of the field amplitude in real space, $\sigma_r$, is related to $\sigma_q$ by $\sigma_r\sigma_q = 1$. From this, the r.m.s. of the intensity distribution is

$$\sigma_{r,\text{intensity}} = \frac{\sigma_r}{\sqrt{2}} = \frac{1}{2k\sigma_{\text{N.A.}}} = \frac{\lambda}{4\pi\sigma_{\text{N.A.}}} \tag{3.27}$$

Comparing a Gaussian function with an Airy pattern of equal FWHM, the first minimum of the airy pattern will be located at 2.7918 standard deviations from the central peak. Using this radius as the resolution, the Rayleigh criterion becomes

$$\rho = 2.7918\frac{\lambda}{4\pi\sigma_{\text{N.A.}}} = 0.222\frac{\lambda}{\sigma_{\text{N.A.}}} \tag{3.28}$$

Figure 3.4 shows a comparison between the Gaussian and Airy disc profile with matching FWHM. There are of course other possible fitting choices. For example, constraining the integrated intensity of the Gaussian PSF to be equal to that of the Airy disc (with identical peak intensity) changes the prefactor on the right hand side of (3.28)from 0.222 to 0.219.
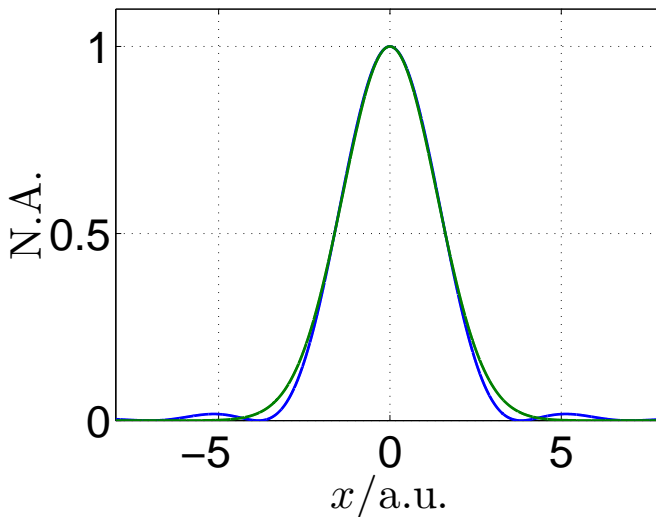
**Figure 3.4:** Comparison of Gaussian and Airy disc profile with matching FWHM.

As several formulas in optics include N.A. as a parameter, and assumes a circular aperture, it is useful to have a relation between the $\sigma_{N.A.}$ of a Gaussian aperture and a circular one. Combining (3.25) and (3.28) yields

$$N.A. \quad = \quad 2.75\sigma_{N.A.}. \tag{3.29}$$

(3.28) of course assumes that the numerical aperture of the lens is determined by the Gaussian absorption profile, rather than the finite physical aperture. In the cases where the physical aperture becomes relevant, the point spread will no longer be a Gaussian function.

## 3.3   Optimal CRL geometry

In this section the physical limits of the achievable N.A. of CRL lenses will be considered. All the formulas presented so far is under the assumption of constant profile CRLs, meaning $\omega$ and $R_0$ is constant throughout the CRL. However, in the context of optimizing N.A., this is not the optimal shape. A higher numerical aperture can be obtained by letting $\omega$ and $R_0$ vary along the optical axis, and the shape that optimizes the N.A. under this privilege is called the adiabatic lens [69]. Although the prospect of imaging with adiabatic lenses is an interesting one, such CRLs have not yet been mad, so in this section only constant profile CRLs will be considered.

Figure 3.5 gives an impression of how the N.A. of a constant profile CRL scales
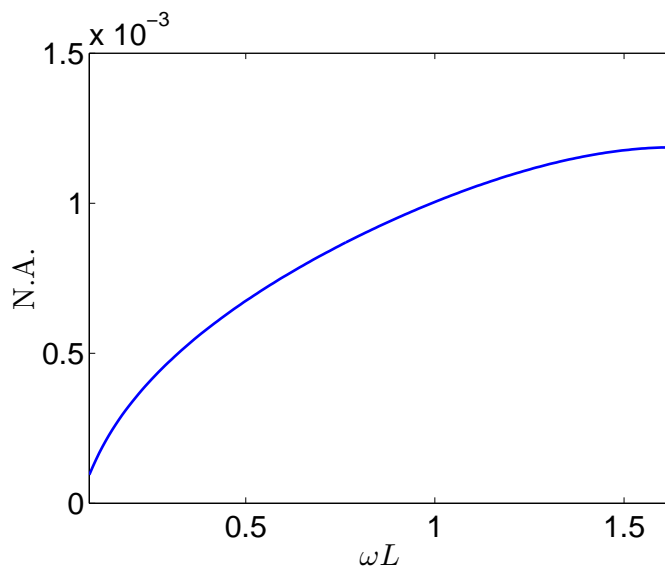
**Figure 3.5:** Numerical aperture as function of CRL length, calculated using (3.22). The calculation parameters were $\omega = 5.43$, and $\mu = 0.41$ cm$^{-1}$, which corresponds to Be lenslets with $R = 50$ $\mu$m and $T = 1.6$ mm at $E = 17$ keV. $q$ was kept constant at 3 m, while $p$ was adjusted to satisfy imaging the condition.

with its length. A finite fixed value of $q$ was used, while $p$ is constrained to satisfy the imaging condition. The maximum is found with the maximum CLR length, i.e. where $p = 0$. Assuming that $q$ is large enough so that

$$\omega L_{\text{max}} \approx \pi/2, \tag{3.30}$$

according to (3.22),

$$\sigma_{\text{N.A.}}^2 = \frac{2\omega}{k\gamma\pi}. \tag{3.31}$$

This would suggest that if one could make $\omega$ arbitrarily large, which under constant $q$ would only solidify the approximation made in (3.30), one could make an arbitrarily large numerical aperture, regardless of $\gamma$. In reality, this is of course not possible. For a given geometrical aperture, geometrical constraints set an upper bound on the value of $\omega$. For a CRL to be realizable, it is clear that

$$2 \cdot \frac{R_0^2}{2R} < T \tag{3.32}$$

must be satisfied. By substituting $R = f/2\delta$ and $\omega = (fT)^{-\frac{1}{2}}$ into (3.32), one

**Table 3.1:** $R_0$ is assumed to be the maximum for the given $R$ and $T$, i.e. $R_0 = \sqrt{RT}$.

| Material | $R/\mu m$ | $T$ | $R_0/\mu m$ | $\omega/m^{-1}$ (at 17 keV) | $\gamma$ (at 17 keV) | Reference |
|---|---|---|---|---|---|---|
| Be | 50 | 1.6 mm | 283 | 5.43 | $2.0 \cdot 10^{-4}$ | [28] |
| Al | 200 | 5 mm | 1000 | 1.9 | $4.3 \cdot 10^{-3}$ | [82] |
| Si | 3.75 | 60 $\mu m$ | 15 | 122 | $5.4 \cdot 10^{-3}$ | [73] |
| Si | 20 | 1.54 mm | 175 | 10.4 | $5.4 \cdot 10^{-3}$ | [72] |
| Diamond | 500 | 0.6 mm | 548 | 4.10 | $4.1 \cdot 10^{-4}$ | [80] |
| PMMA | 200 | 0.22 mm | 200 | 6.48 | $5.3 \cdot 10^{-4}$ | [23] |
| SU-8 | 300 | 2.4 mm | 840 | 1.67 | $5.5 \cdot 10^{-2}$ | [39] |

can see that the maximum value of $\omega$ for a given $R_0$ is

$$\omega_{\max} = \frac{\sqrt{2\delta}}{R_0}. \tag{3.33}$$

To estimate the geometrical aperture, consider a ray entering a CRL of length $L = L_{\max}$ at $x_i = 0$ with an angle $w_i$. If $w_i$ is larger than the critical angle, $\theta_c = \sqrt{2\delta}$, the ray will escape the geometrical aperture of the lens [8]. Therefore, as long as $\omega L > \pi/2$, which is the case when $L = L_{\max}$, the critical angle sets the geometrical limit of the numerical aperture. Substituting (3.33) int (3.31) yields

$$\sigma_{\text{N.A.}}^2 = \frac{2\sqrt{2\delta}}{k\gamma\pi R_0}. \tag{3.34}$$

Thus $\sigma_{\text{N.A.}}$, which relates to the numerical aperture as determined by absorption only, can be made arbitrarily large by reducing $R_0$. Therefore, if one had the capability to make CRLs with arbitrary precision, $\theta_c$, which is independent of $R_0$, is the largest possible N.A.. Ignoring the fact that when $R_0$ is small, both transmission and N.A. falls off rapidly if the sample is moved off axis, the above analysis would imply that the materials with high electron density would be the best materials. In practice, however, the manufacturing quality, in combination with material properties, determines what the most suitable material is. The most commonly used materials for CRLs are listed in Table 3.1. The tabulated data gives an impression of what is available with present technology. Note however that only the three first entries are about 2D lenses. In the third entry, 2D lenses were composed of two interdigitated sets of 1D lenses perpendicularly. The rest of the cases are examples of lenses that were designed for focusing and other beam conditioning purposes. Note also that the table lists no information on lens aberrations, which is important when many lenses are used. Aberration characterization techniques based on grating interferometry exist [39], but currently, data on lens aberrations is scarce.
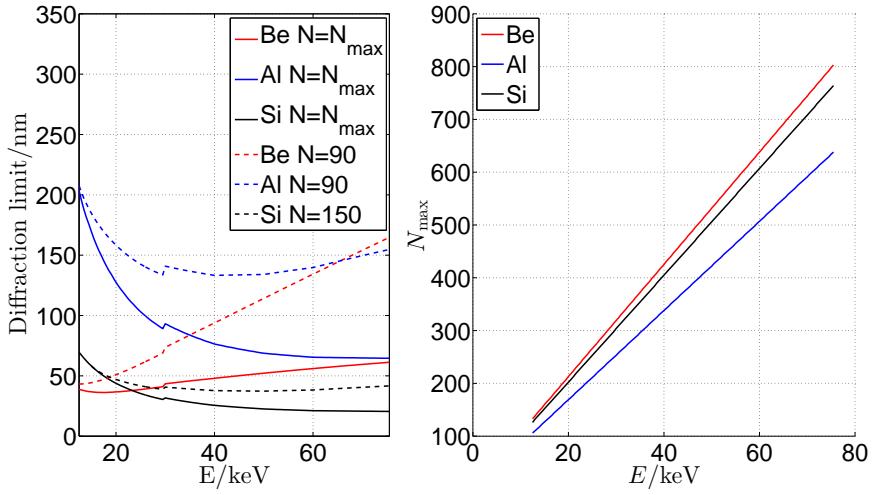
**Figure 3.6:** Diffraction limit as a function of energy with fixed lenslet geometry. Parameters for Be and Al are taken from Table 3.1, while the Si parameters are set to $R = 5~\mu m$ as suggested in [72], and demonstrated to be possible for a 1D CRL [73]. The physical aperture was set to $R_0 = 25~\mu m$, and $T = 125~\mu m$, taking into account that pairs of perpendicular lenslets are needed. Mass attenuation coefficinets are taken from the CXRO [21] and NIST [58] database below and above 30 keV, respectively. The sudden jump in the diffraction limit around 30 keV is related to the change of database.

# Chapter 4

# Illumination and detection

Illumination and detection are critical components of a microscope. A microscope is comprised of components both upstream and downstream of the sample position. The focus has so far been mostly on the latter, but the former should be considered equally important. This chapter will describe some properties of synchrotron radiation sources, monochromators, decoherers, and illumination schemes involving condenser lenses. It will also describe the most commonly used X-ray imaging detector scheme, as well as tomography.

## 4.1   Synchrotron radiation

Synchrotrons produce X-rays by subjecting electrons moving at relativistic velocities to magnetic fields.

Modern synchrotrons inject accelerated electrons into a storage ring, which serves to keep the electron energy more or less constant and at the same time facilitate fields used to produce the electromagnetic radiation for experiments.

One measure of the quality of a source is the brilliance, defined as [62]

$$\mathcal{B}(E) = \frac{\Phi(E)}{4\pi\sigma_x\sigma_{\theta_x}\sigma_y\sigma_{\theta_y}},\tag{4.1}$$

where $\Phi(E)$ is the total flux of photons at a 0.1% bandwidth around $E$. $\sigma_x$ and $\sigma_y$ are the spatial extents of the source in the $x$ and $y$ direction, respectively, while $\sigma_{\theta_x}$ and $\sigma_{\theta_y}$ are the corresponding divergences.

### 4.1.1　Bending Magnet

In the magnetic field of a bending magnet, the electron moves in a circular path, and electromagnetic radiation is emitted due to the acceleration of the electron. With relativistic electrons, the angle of the radiation cone, is [2]

$$\Delta\Omega = \frac{1}{\gamma}, \tag{4.2}$$

where $\gamma$ is the lorentz factor. The storage ring of European synchrotron radiation facility, where all of the experiments described in this work took place, operates at $\varepsilon_e = 6.03$ GeV, which yields $\gamma^{-1} = 8.5 \times 10^{-5}$ rad. The characteristic frequency $\nu_c$ of the bremsstrahlung is given by [2]

$$\hbar\nu_c[\text{keV}] = 0.665\varepsilon_e^2[\text{GeV}]B[\text{T}] \tag{4.3}$$

where $\varepsilon_e$ is the total energy of the electron, including its rest energy. The radiated power is

$$\mathcal{P}[\text{kW}] = 1.266\varepsilon_e^2[\text{GeV}]B^2[\text{T}]L[\text{m}]I[\text{A}] \tag{4.4}$$

where I is the storage ring current, and $L$ is the distance each electron stays along the circular path, i.e. the source length. Note that while changing $B$ or $\varepsilon_e$ will affect the output power, it does not significantly, change number of photons emitted (per electron) [2].

### 4.1.2　Undulator

An undulator is a series of magnets with alternating polarity so that the electron is set in sinusoidal-like motion in the orbit plane orthogonal to the incident electron momentum. The transverse acceleration of the electron causes the electron to give of electromagnetic radiation. As the speed of the electrons is close to the speed of light, the observed frequency of the radiation will be significantly Doppler shifted. A simple way to model the undulator, that captures its main features, is to regard the radiation as the signal emitted from a single magnet, convoluted by a sum of $2 \times N$ Dirac $\delta$-functions with alternating signs. Each delta function is located at a position and time corresponding to where and when the electron passes each magnet. By the convolution theorem, this would imply that the observed spectrum is the spectrum emitted form a single magnet, multiplied by the Fourier transform of the distribution of $\delta$-functions. The Fourier transform of the $\delta$-functions is

$$S(\mathbf{k}) = \mathcal{F}\{\sum_{j=0}^{N-1} \delta\left(x, y, z - j\lambda_u, t - j\frac{\lambda_u}{c\bar{\beta}}\right) - \delta\left(x, y, z - (j + \frac{1}{2})\lambda_u, t - (j + \frac{1}{2})\frac{\lambda_u}{c\bar{\beta}}\right)\}$$

$$= \left(1 - e^{\frac{i}{2}\lambda_u\left(\frac{k}{\bar{\beta}} - k_z\right)}\right) \frac{e^{iN\lambda_u\left(\frac{k}{\bar{\beta}} - k_z\right)} - 1}{e^{i\lambda_u\left(\frac{k}{\bar{\beta}} - k_z\right)} - 1} \tag{4.5}$$

where $ck$ was substituted for $\nu$, and $\bar{\beta}$ is the average velocity of the electron along the optical axis, divided by $c$. An illustration of the amplitude of $S(\mathbf{k})$ in reciprocal space can be seen in Figure 4.1. The illustration demonstrates the characteristic feature of the undulator, namely harmonic spectral peaks. The peak along the optical axis can be found by calculating the value of $k$ that satisfies

$$\lambda_u \left( \frac{k}{\bar{\beta}} - k \right) = n2\pi. \tag{4.6}$$

$\bar{\beta}$ can be found by estimating the trajectory of the electron inside the undulator. Doing so yields the so called undulator equation

$$\lambda_n = \frac{\lambda_u}{2\gamma^2 n} \left( 1 + \frac{K^2}{2} + \gamma^2\theta^2 \right) \tag{4.7}$$

where $\theta$ is the angle of observation relative to the optical axis, and $K$ is the ratio between the largest angle the electron path makes with the optical axis and $\Delta\Omega$, and is given by

$$K = \frac{eB}{m_ec} \frac{\lambda_u}{2\pi}. \tag{4.8}$$

Here $B$ is the magnetic field strength, $m_e$ is the electron mass, and $e$ is the electron charge. The total flux in the central cone of the undulator is [2].

$$\frac{\text{photons/second}}{0.1\,\%BW} \approx 1.43 \cdot 10^{14} NI[\text{A}] \frac{K^2}{1 + K^2/2} \tag{4.9}$$

By increasing $B$, the electron will be more delayed due to a longer path length, which results in a longer wavelength. By tuning $B$, the harmonic peaks can be moved to the desired wavelength. In practice, $B$ is tuned by adjusting the vertical gap between magnet pairs. Only odd harmonic peaks are present as it has been assumed that the X-ray emission from magnets of opposite polarity differ only in the sign. A slightly more accurate model is to assume that the signals are mirrored around the $yz$-plane. When this is the case, even harmonics can appear as long as the observer is not exactly on the optical axis.

The relative bandwidth of the harmonic peaks, evaluated by finding the FWHM of $|S(\mathbf{k})|^2$ along the $k_z$ axis, as illustrated in Figure 4.2(a), is [2]

$$\frac{\Delta\nu}{\nu_n} = \frac{0.886}{nN}, \tag{4.10}$$

where $\nu_n = \frac{2\pi}{c\lambda_n}$ is the frequency of the $n$-th harmonic peak. The amplitude of the peak is proportional to $N^2$. Note that it has been assumed that the path of the
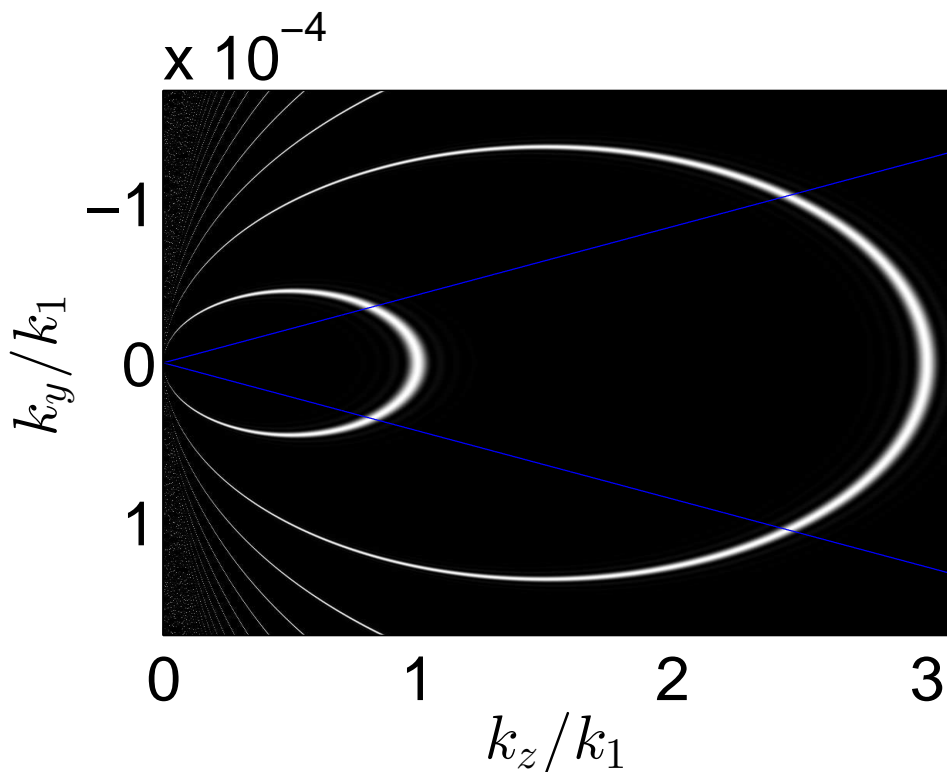
**Figure 4.1:** $|S(\mathbf{k})|^2$ in the $k_z k_y$-plane. The blue lines represents form an angle $\gamma^{-1}$. The axes are in units $k_1 = \frac{2\pi}{\lambda_1}$. Parameters used were $\lambda_u = 18$mm, $\bar{\beta} = 1 - 4 \times 10^{-9}$, and $\gamma = 1.17 \times 10^{-4}$, which implies $K = 0.48$ and $E_1 = \frac{2\pi c\hbar}{\lambda_1} = 17$ keV. The nuber of undulator periods were set to $N = 16$, which is low compared to typical values used in real undulators, but makes the figure more presentable.
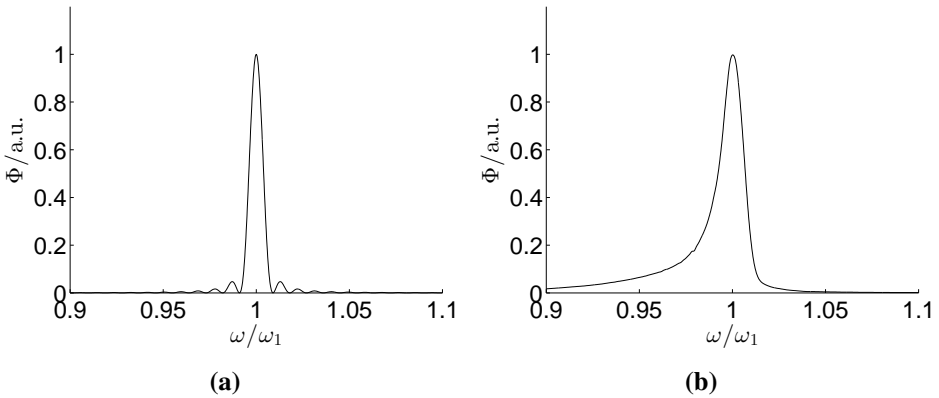
**Figure 4.2:** (a) $|S(\mathbf{k})|^2$ sampled along $k_z$ axis, and (b) measured spectrum at beam line ID06 at the ESRF. The axes are in units $k_1 = \frac{2\pi}{\lambda_1}$. Parameters used were $\lambda_u = 18\text{mm}$, $\bar{\beta} = 1 - 4 \times 10^{-9}$, and $\gamma = 1.17 \times 10^{-4}$, which implies $K = 0.48$ and $E_1 = \frac{2\pi c\hbar}{\lambda_1} = 17\,\text{keV}$. The number of undulator periods were set to $N = 110$.

electron is perfectly periodic. If there is imperfection in the magnetic field, so that there is an element of randomness to the electron path, then the $N$-th oscillation may not be in phase with the first oscillation. If that is the case, then one can not count all $N$ oscillations as contributing coherently, resulting in a band broadening. In addition, (4.10) assumes that only on-axis radiation will reach the observer, neglecting the lower frequency off-axis radiation. In practice, unless the beam is filtered by for example a pinhole [1], the observed spectrum from an undulator will not look like Figure 4.2(a). Figure 4.2(b) shows a real undulator spectrum. The measured FWHM was approximately twice the bandwidth predicted by (4.10), and a tail caused by off-axis radiation can be seen on the lower frequency side.

When $K$ is small, the apparent acceleration, of the electron is close to sinusoidal and the radiation will mostly be concentrated in the first harmonic peak. If $K$ is increased, the apparent trajectory will transition from a sinusoidal to a more triangle wave-like path, which results in increased power in the higher order harmonics [2]. If the power is distributed over a large number of harmonics, then the insertion device is called a wiggler[1]. For pink beam microscopy, it is desirable to concentrate as much power as possible in a single peak. Thus undulators are more suitable than wigglers.

---

[1]Although a wiggler does have harmonic peaks, the tail effect, seen in Figure (4.2(b)) is often so severe that the spectrum is essentially an incoherent sum of single magnet spectra. [1].

## 4.2   Monochromators

The spectral widths of synchrotron sources are larger than what is desirable for most microscopy purposes. Monochromators are employed to select narrower parts of the spectrum. There are two main classes of X-ray monochromators, namely multilayer mirrors and crystal monochromators.

Crystal monochromators utilizes the Bragg condition to diffract X-rays over a narrow bandwidth. The bandwidth of the reflection curve, according to the Darwin theory of dynamical diffraction [22, 4], is

$$\zeta_D = \frac{\Delta\lambda}{\lambda} = \frac{4}{\pi}\left(\frac{d}{m}\right)^2 \frac{r_0\,|F_\mathbf{h}|}{v_c} \tag{4.11}$$

where $r_0$ is the classical electron radius, $v_c$ is the crystal unit cell volume, and $|F_h|$ is the structure factor amplitude, describing the kinematical scattering power of the crystal with the reciprocal lattice vector $\mathbf{h}$ in Bragg condition. For a Si-111 crystal reflection, the Darwin width is approximately $\frac{\Delta\lambda}{\lambda} \sim 10^{-4}$ [4]. The crystals are normally cut so that $\mathbf{h}$ is normal to the surface, and by applying two crystals rather than a single one, it is possible to filter out any energy from the source without having to realign all downstream components for every change in energy.

Multilayer mirrors are made from alternating layers of materials with different electron density. Their properties are mainly determined by the thickness and refractive indices of the layers. For a given set of multilayer parameters, the reflectivity curve is a function of the momentum exchange of the reflected photon, $q$. The curve can be modelled using Parratt's method [3, 64], see example in Figure 4.3. The main features of the curve are the peaks, and the total reflection region near $q = 0$. When using a multilayer mirror, one is typically interested in using the first peak. The peak positions are given by a modified Bragg's law [78]

$$j\lambda = 2\Lambda\sin(\theta_j)\left(1 - \frac{\bar{\delta}}{\sin(\theta_j)^2}\right), \tag{4.12}$$

where $\bar{\delta}$ is the mean refractive index decrement, $\Lambda$ is the layer period, and $\theta_j$ is the angle of the $j$th reflection.

As both the crystal and the multilayer monochromators produce more or less harmonic peaks, it may well happen that a noticeable amount of radiation from the third undulator harmonic peak will reach the detector in a microscopy setup.

## 4.3   Illumination schemes

While it is possible to perform microscopy by using only an objective lens, there are in some cases a lot to gain by employing a so-called condenser lens. A con-
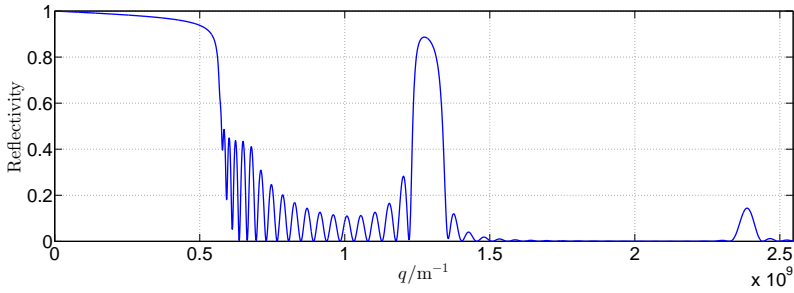
**Figure 4.3:** Reflectivity curve obtained by Parratt's method. Parameters used were, $\Delta_1 = 2.06$ nm, $\Delta_2 = 3.37$ nm, $\delta_1 = 7.79 \cdot 10^{-6}$, $\delta_2 = 1.7 \cdot 10^{-6}$, $\beta_1 = 1.55 \cdot 10^{-7}$, $\beta_2 = 5.17 \cdot 10^{-7}$, and the number of periods were set to 20. These parameters roughly corresponds to the Ru/B$_4$C multilayer used in one of the experiments related to this thesis [28], at 17 keV.

denser lens is a lens placed upstream of the sample, whose traditional role is to condense radiation from the source onto the sample, providing more intense illumination. Another important effect of the condenser is its influence on coherence, and as a consequence, resolution. As partial coherent images can to an approximation be considered a sum of coherent images formed with plane wave illuminations at different angles, it is instructive to consider the consequence of misalignment of the condenser. This chapter will explain some general effects related to the convergence and alignment with respect to the optical axis, followed by a description of the most relevant illumination schemes.

### 4.3.1 Illumination misalignment effects

The ideal convergence of the beam is such that it comes to a focus at the entrance pupil plane. The entrance and exit pupil planes are traditionally defined as the images of the aperture stop at the object and image side, respectively. Recall that the principle ray should cross the optical axis at the aperture stop, but as absorption in the CRL is spread out longitudinally, there is no immediately obvious plane to define the aperture stop. It will serve, however, to define the aperture plane as the plane where the principle ray crosses the optical axis. The pupil planes may then be defined as the images of the aperture plane. The distance to the entrance pupil plane from the object plane will be $g_{\text{ideal}}$, as defined in (3.24), because focusing the illumination at this plane maximizes the transmission, and will by the definition above cross the optical axis at the aperture plane. Figure 4.4 demonstrates the effect of not focusing at the pupil plane, but using a parallel beam instead. The sample objects were an unresolved vertical grating, some stars, and some circles. These objects were simulated as both phase shifting and absorbing. In addition

to these, there were some objects that were simulated as pure phase objects. The undistorted samples can be seen in Figure 4.5. Figure 4.6 shows the same situation with properly converging illumination.

A related effect is the distortion that occur when the optical system is misaligned with the optical axis. Figure 4.7 illustrates the same situation as in Figure 4.6, differing only in that the illumination is off-axis. The off-axis illumination was simulated by applying a constant phase gradient to the sample transmission function. A shading effect now appears on the edges of the stars. This is similar to the shading effects in Figure 4.4, except for the fact that in this case, the shading is biased in the direction of the misalignment, as opposed to being radially biased.

There are some shapes in Figure 4.7 that are barely visible in Figure 4.6. These are objects in the sample that were simulated as pure phase objects, i.e. objects that produce no absorption contrast. This demonstrates how the off-axis illumination can be exploited as a simple and easy to implement phase contrast mechanism.

Another important point is that the grid that was barely resolvable in the aligned image have become resolved in the off axis image. The reason for this is clear when comparing 4.6(a) and 4.7(a). If the angle of the illumination changes significantly during one exposure time, then the recorded image is an intensity average of the several off axis images. Some of the images will have a resolved grating, and others not. The shading effect, however, will not necessarily emerge because the bias is averaged out. This is the role of coherence in microscopy.

## 4.3.2   Critical illumination

In the critical illumination scheme, the source plane is imaged onto the sample plane via a condenser lens, as illustrated in Figure 4.8. A drawback of critical illumination is that if the source has uneven intensity, it will result in uneven illumination. The solution to the problem of source image structure is the so-called Köhler illumination scheme, illustrated in Figure 4.9, where the source is imaged onto the back focal plane of the objective. However, with undulator sources, this is typically not an issue. The main contribution to uneven illumination tends to be imperfections in the optical elements themselves.

The maximum field of view is restricted by the size of the image of the source. It is of course possible to image the source with a larger magnification, however, the larger the magnification, the more the condenser acts like a collimator, as illustrated in Figure 4.10. A collimated beam results radial misalignment effects, as shown in Figure 4.4, and is less effective at reducing coherence.
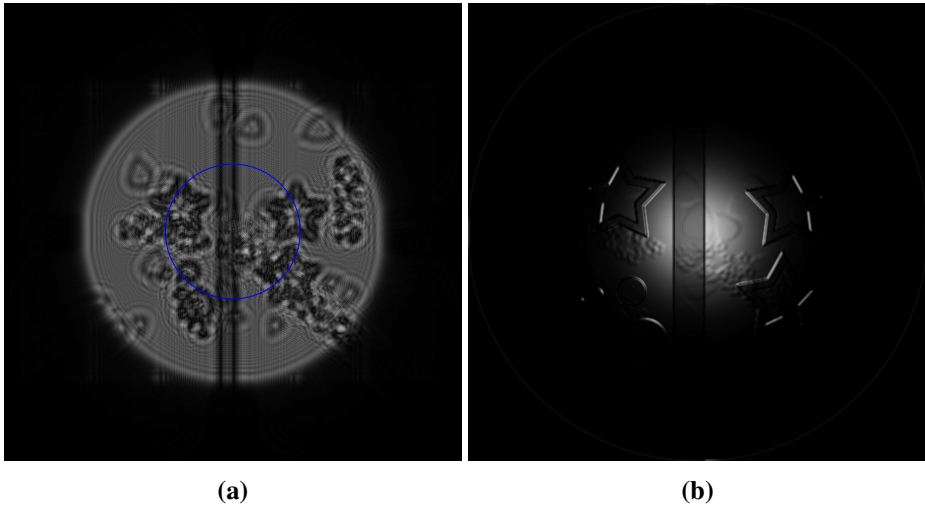
(a)  (b)

**Figure 4.4:** (a) Scalar field as it appears at the aperture plane with parallel beam illumination. The pupil function was a Gaussian, and the blue circle has a radius of $2.75\sigma_{\mathrm{N.A.}}$. (b) Resulting image.
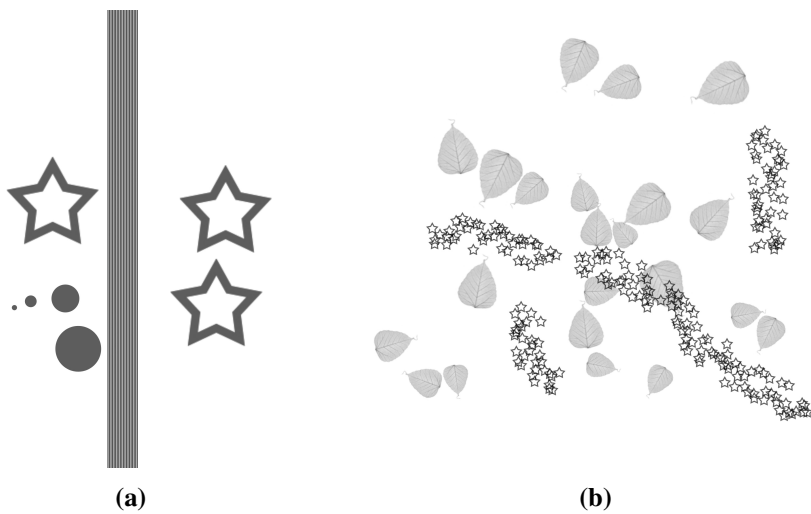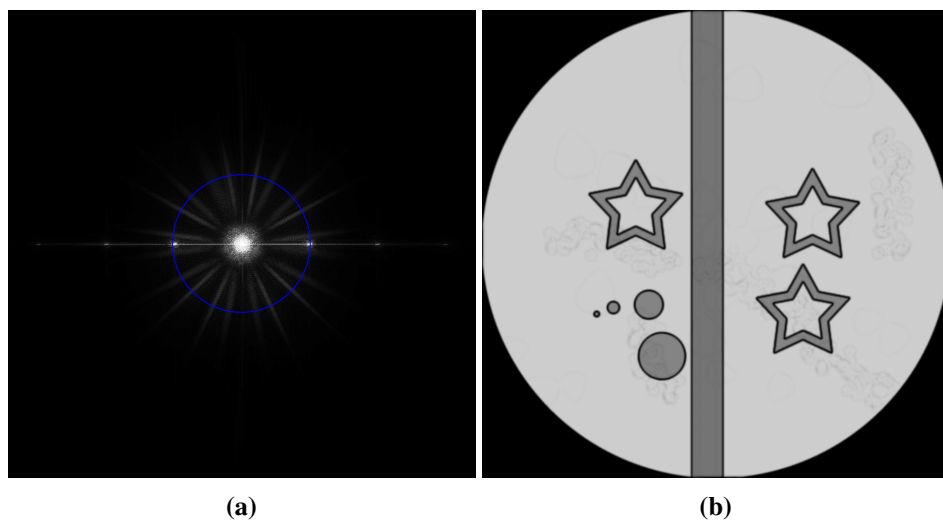


(a)  (b)

**Figure 4.5:** Phantoms used in the simulations in this chapter, separated into (a) Sample objects with $\beta/\delta = 0.05$, and (b) Sample objects that only refract, and do not absorb. i.e. $\beta/\delta = 0$. (a) and (b) were superimposed in the simulations.

(a)                                    (b)

**Figure 4.6:** (a) Scalar field as it appears at the aperture plane with properly converging illumination. The pupil function was a Gaussian, and the blue circle has a radius of $2.75\sigma_{\mathrm{N.A.}}$. (b) Resulting image.



(a)                                    (b)
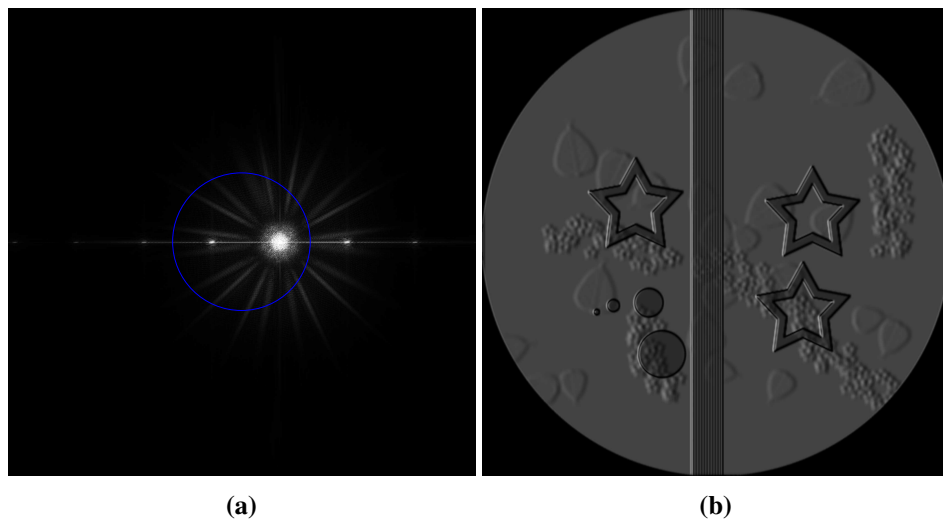
**Figure 4.7:** (a) Scalar field as it appears at the aperture plane, with off-axis illumination. The pupil function was a Gaussian, and the blue circle has a radius of $2.75\sigma_{\mathrm{N.A.}}$. (b) Resulting image.
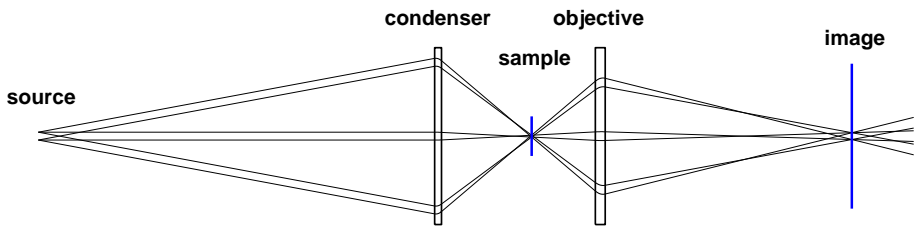
**Figure 4.8:** Illustration of critical illumination scheme.
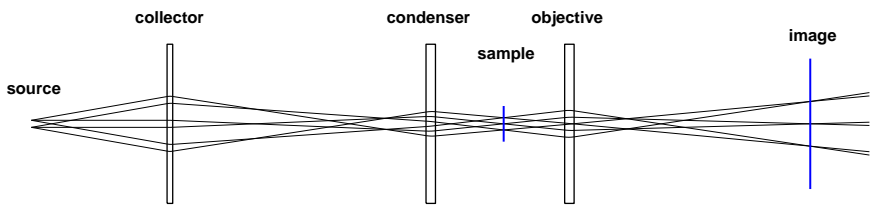


**Figure 4.9:** Illustration of Köhler illumination scheme.



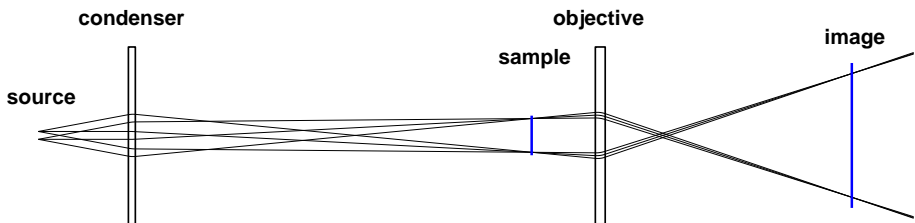**Figure 4.10:** Illustration of critical illumination with magnified source.

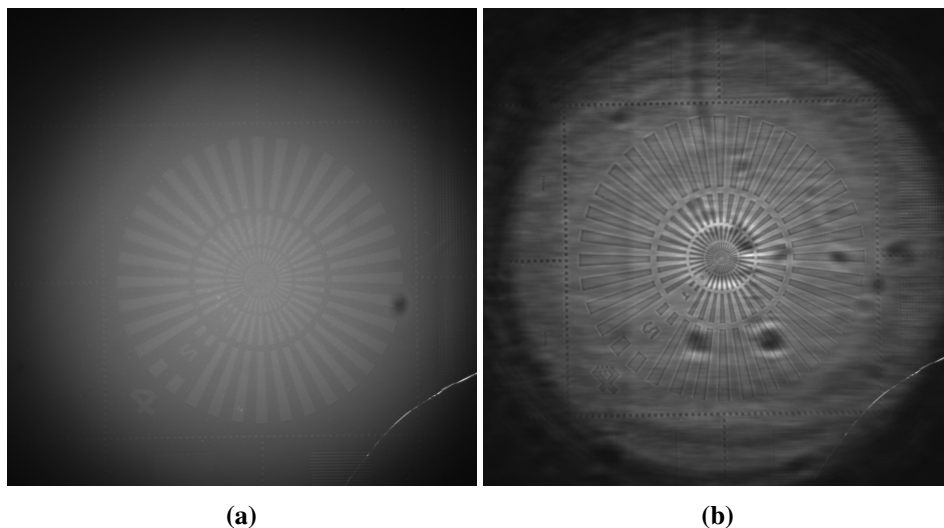(a)                                                           (b)

**Figure 4.11:** Raw images of Siemens star test object (a) with and (b) without decoherer.
A condenser was used in both cases.

### 4.3.3    Illumination focused in objective

A solution to the small field of view from the critical illumination scheme is to
image the source some distance away from the sample. As explained in section
4.3.1, focusing the illumination into the pupil plane at a distance $g_{ideal}$, given in
(3.24), from the sample has the benefit of removing radial misalignment effects.
It also has some merit when it comes to chromatic aberration, as will be shown
later. The drawback of the scheme is that it produces a longer coherence length
compared to critical illumination.

### 4.3.4    Decoherer

Another method of reducing coherence is by the use of a beam diffusing object,
also called decoherer or just a diffuser. A decoherer is a piece of strongly scattering
material placed upstream of the sample. It should be moving so that its diffraction
pattern will be averaged out during camera exposure. A typical implementation is
a spinning disc. As mentioned, the main sources of structure in the illumination
are imperfections in optical components, such as lenses, Beryllium windows, and
multilayer mirrors. While a decoherer reduces the coherence length, its biggest
impact on image quality is in its ability to smooth out structures in the illumination,
as illustrated in Figure 4.11. If the decoherer is placed too far upstream from a
lens or aperture, significant scattering losses may occur. Reasonable positions for
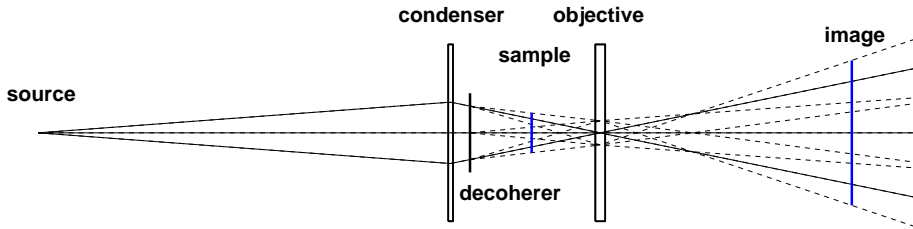
**Figure 4.12:** Maximum transmission configuration, with decoherer. Dashed lines rays that are scattered from the decoherer. Dashed lines represent scattered rays.

standard applications are between sample and condenser. Placing it close to the sample is more efficient in terms of scattering losses, however, in order to smooth out structures, there should be some space between the diffuser and the object plane to allow the beam to diffuse. The best suited distance depends on the size of beam structure.

A schematic drawing of the maximum transmission illumination scheme with decoherer can be seen in Figure 4.12.

### 4.3.5 Measurement of decohering properties

In the imaging experiments described in this thesis, a decoherer was used to reduce the coherence of the beam. Yet, as decoherer has spatial features of finite size, it can not completely remove the coherence.

There are several ways of modelling the decohering properties but here it suffices to stick to the projection approximation. It will be assumed that the decoherer has a complex transmission function $f(x, y, t)$ so that

$$\psi'(x, y, t) = f(x, y, t)\psi(x, y, t) \tag{4.13}$$

where $\psi$ and $\psi'$ is the field immediately upstream and downstream of the decoherer, respectively.

Assuming the decoherer to be isotropic and homogeneous on large scales, time averaging is equivalent to a spatial averaging. Furthermore, it is assumed that the decoherer spins fast enough for a statistically representative area to be sampled during each exposure. Assuming further that $f$ and $\psi$ is uncorrelated, the cross-spectral density can be written as

$$\tilde{\Gamma}_s(\boldsymbol{\xi}_1, \boldsymbol{\xi}_2, \nu) = \langle \psi(\boldsymbol{\xi}_1)^* \psi(\boldsymbol{\xi}_2) \rangle \langle f(\boldsymbol{\xi}_1)^* f(\boldsymbol{\xi}_2) \rangle \tag{4.14}$$

If the incident beam is much more coherent than the beam immediately down-stream of the decoherer[2], (4.14) can be approximated as

$$\tilde{\Gamma}_s(\boldsymbol{\xi}_1, \boldsymbol{\xi}_2, \nu) = I_{s,\nu}(\bar{\boldsymbol{\xi}})\langle f(0)^* f(\boldsymbol{\Delta\xi})\rangle. \tag{4.15}$$

This expression is on the same form as (2.43), which allows the use of the generalized Van cittert-Zernike theorem (2.44).

In order to investigate the decohering properties of the decoherer, a simple SAXS experiment was performed. The experimental setup (illustrated in Figure 4.14) consisted of the decoherer and a detector, separated by a distance $\Delta z = 3.67$ m. A condenser lens, consisting of 6 double concave Be-lenslets with $R = 50$ $\mu$m, and was positioned to image the source, located 53 m upstream, onto the detector plane. By focusing the incident beam on the detector, the far field scattering pattern from the diffuser is imaged onto the detector, without adversely affecting the validity of (2.42) [31].

The recorded intensity distribution at the detector plane is according to (2.44),

$$\begin{aligned}
I_{\nu,o}(\mathbf{r}) &= \tilde{\Gamma}_o(\mathbf{r}, \mathbf{r}, \nu) \\
&= \frac{k^2 e^{-\frac{ik}{\Delta z}(|\mathbf{r}|^2 - |\mathbf{r}|^2)}}{4\pi^2 \Delta z^2} \kappa(\mathbf{r}) \int I_{s,\nu}(\bar{\boldsymbol{\xi}}) e^{-\frac{ik}{\Delta z}\boldsymbol{\Delta r}\bar{\boldsymbol{\xi}}} d^2\bar{\boldsymbol{\xi}} \\
&= \frac{k^2}{4\pi^2 \Delta z^2} \kappa(\mathbf{r}) \int I_s(\bar{\boldsymbol{\xi}}) d^2\bar{\boldsymbol{\xi}} \\
&= \text{const.} \cdot \kappa(\mathbf{r})
\end{aligned} \tag{4.16}$$

From this one can identify the complex coherence factor as

$$\mu_{s,\nu}(\boldsymbol{\Delta\xi}) = \frac{4\pi^2 \Delta z^2}{I_{\text{total}} k^2} \int I_{o,\nu}(\bar{\mathbf{r}}) e^{\frac{ik}{\Delta z}\boldsymbol{\Delta\xi}\bar{\mathbf{r}}} d^2\bar{\mathbf{r}}. \tag{4.17}$$

The recorded scattering pattern from a spinning decoherer can be seen in Figure 4.13(a). For comparison, an image of a pattern obtained with the same decoherer kept stationary i shown in Figure 4.13(b). The result of application of (4.17) to the measurements is shown in Figure 4.15. Normalization was applied to ensure $\mu_\nu(0) = 1$, as demanded by (2.40). The results indicate a coherence length of $l_c \approx 150nm$, if the criterion $\mu(l_c) = e^{-1}$ is used. Note however that the field of view did not capture all of the non-negligible intensity. In order to obtain the curve in Figure 4.15, some extrapolation of the intensity data was necessary. The extrapolation was based on the fitting of two Gaussian functions with their peaks were in $w_x = 0$. Comparison of the fit with the data can be seen in Figure 4.16. The integrated intensity in the central spot is small compared to the rest of the intensity, and was therefore not given any special attention.

---

[2]This is not necessarily the case when the actually being employed in a microscopy setup.
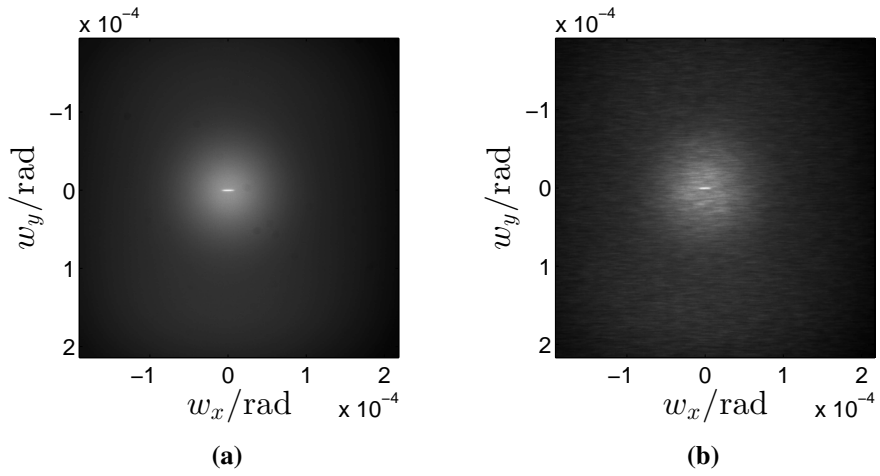
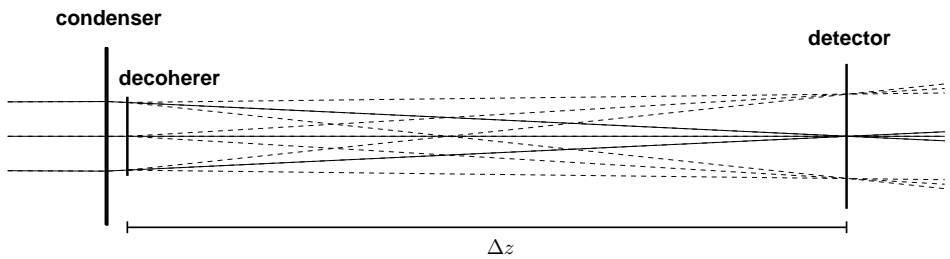**Figure 4.13:** Far field diffraction pattern from (a) spinning, and (b) stationary decoherer.



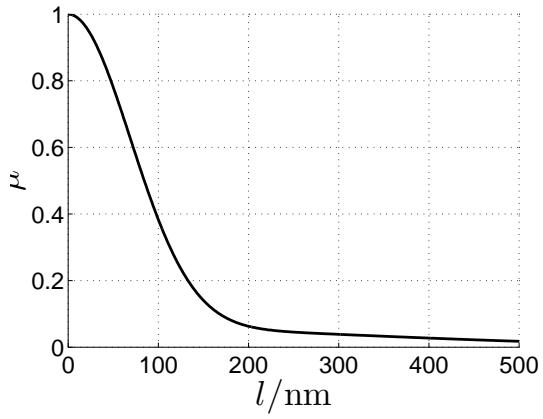**Figure 4.14:** Setup for diffuser diffraction experiment.

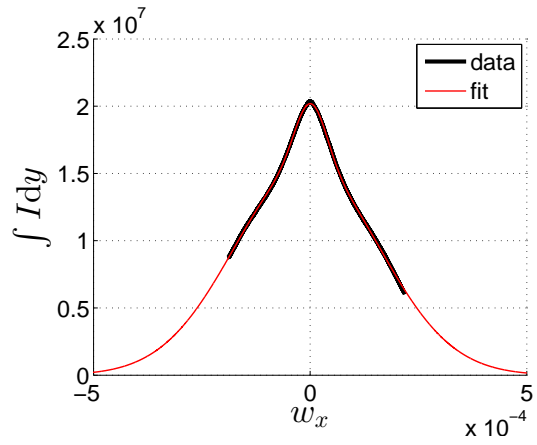**Figure 4.15:** Mutual correlation function.



**Figure 4.16:** Intensity fit.

## 4.4   Indirect X-ray imaging detectors

High resolution X-ray imaging detectors typically consist of a scintillator screen, a visible light microscope, and a CCD or CMOS pixel array. A schematic drawing of a typical setup is shown in Figure 4.17. When X-rays are absorbed in the scintillator, it produces light in the visible spectrum that can be manipulated with visible light optics. The visible light microscope is configured to produce a magnified image of the scintillator screen on the Pixel array. The effective pixel size therefore not only depends on the physical pixel size of the CCD/CMOS-array, but also on the magnification of the visible light microscope.

When an X-ray photon is absorbed in the scintillator, an electron is excited from the valence band. The time it takes for the electron to de-excite is called the decay time, and is typically on the order of micro seconds, or less. This is not to be confused with the afterglow, which is caused by the excited electron possibly being in states from which direct transition to the valence band is forbidden[33]. The time it takes for afterglow to fade is typically much longer than the decay time. In the experiments related to this thesis, a Europium doped $Gd_3Ga_5O_{12}$ (GGG:Eu) scintillator was used. This scintillator has a refractive index of 1.95, a light yield of $44 \ \text{photons/keV}$, and emits at 595 nm wavelength [33]. Precise data on the afterglow and decay time of GGG:Eu is not readily available.

The number of X-ray photons passing through in the scintillator screen for a given time interval is $n_x = \Phi_x t_e$, where $\Phi_x$ is the X-ray flux and $t_e$ is the exposure time. Using Poisson statistics, the variance of $n_x$ is equal to $\langle n_x \rangle$. This variation in $n_x$ gives rise to noise, and is referred to shot noise. The detective quantum efficiency (DQE) of the detector is the ratio of the square SNR of the output and input signal, where output and input refers to pixel values and number of X-rays, respectively. For an X-ray imaging detector such as the one described above [5, 76, 38],

$$\text{DQE} = \frac{\text{SNR}_{\text{out}}^2}{\text{SNR}_{\text{in}}^2} \approx \eta_{\text{abs}} \left( 1 + \frac{1 + \eta_{v/e}^{-1}}{\eta_{\text{col}}(E_x/E_v)\eta_{x/v}} \right)^{-1}, \qquad (4.18)$$

where $\eta_{\text{abs}}$ is the absorption efficiency of the scintillator screen, $\eta_{\text{col}}$ the collection efficiency of the visible light microscope, $\eta_{v/e}$ the quantum efficiency of the CCD or CMOS, $\eta_{x/v}$ the conversion efficiency of X-ray energy into visible light energy, $E_x$ the X-ray energy, and $E_v$ the visible light photon energy.

CCDs and CMOS cameras suffer from so-called dark-current signal. The dark-current signal is proportional to the exposure time. The dark current can be corrected for by subtracting an image taken without any X-ray signal present. However, the dark current signal will produce shot noise too, which of course is not eliminated by the subtraction. In addition to shot noise, there are several sources of noise

within the electronics of the camera, collectively referred to as read-out noise, mux noise, or the noise floor [34]. This noise is added to the shot noise, irrespective of the number of X-rays.

As an X-ray passes through the scintillator screen, it will deposit its energy not in a single plane, but everywhere along the thickness of the scintillator. Therefore, an appropriate relation between the scintillator thickness and the N.A. of the microscope must be used. Defining the resolution as the full width that covers $90\%$ of the integrated LSF [38],

$$r = \sqrt{\left(\frac{c_1}{\text{N.A.}}\right)^2 + (c_2 t_s \text{N.A.})^2} \tag{4.19}$$

where $t_s$ is the thickness of the scintillator screen. The coefficients $c_1$, and $c_2$, will depend on the scintillator material.

As $\eta_{\text{abs}}$ increases with increasing scintillator thickness, due longer beam paths over which the X-rays can be absorbed, there is a trade-off between the DQE and resolution. The maximum scintillator thickness for a given target resolution is [38]

$$t_{s,\text{opt}} = \frac{r^2}{2c_1 c_2} \tag{4.20}$$

If this thickness is chosen, the value of N.A. that must be used in order to achieve the target resolution is [38]

$$\text{N.A.}_{\cdot\text{opt}} = \sqrt{2}\frac{c_1}{r}. \tag{4.21}$$

## 4.5  Tomography

Tomography is a well-established imaging method based on 3D reconstruction of sample volume from a set of 2D projection images covering different sample orientations [13, 37].

All tomograms produced in this thesis were recorded with continuous scans, i.e. projections were recorded while the sample rotated at a constant speed. As the sample does not have to be accelerated and decelerated between recording each projection image, continuous scans has a speed advantage over non-continuous scan.

Reconstruction algorithms fall into two main categories, namely filtered back projection (FBP), and algebraic reconstruction algorithms. In the work related to this thesis, only FBP was used. The FBP algorithm relies on the radon transform and
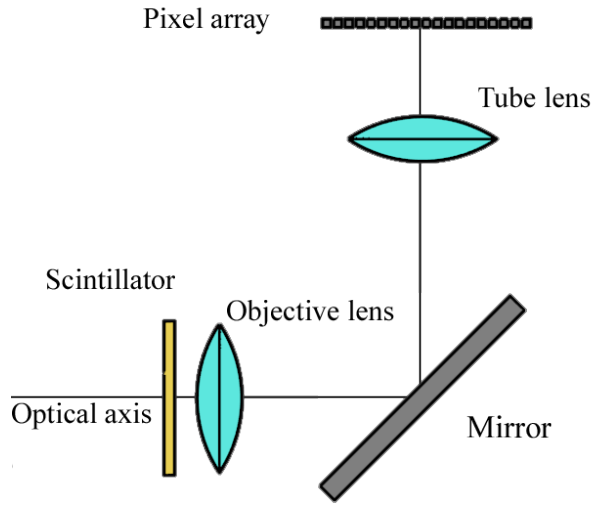
**Figure 4.17:** Schematic drawing of imaging detector.

the Fourier slice theorem, which states that a projection, $p$, in real space corresponds to a slice in Fourier space. For example, if $p_\theta(\xi)$ is a 1-dimensional projection of the two dimensional function $f(x, y)$, where $\theta$, as illustrated in Figure 4.18, is the angle of the projection direction, then $p_\theta(\xi)$ is defined as

$$p_\theta(\xi) = \int f(\xi \cos(\theta) + \eta \sin(\theta), \xi \sin(\theta) - \eta \cos(\theta)) \mathrm{d}\eta, \qquad (4.22)$$

and the Fourier slice theorem states

$$\tilde{f}(q \cos(\theta), q \sin(\theta)) = \int p_\theta(\xi) e^{iq\xi} \mathrm{d}\xi. \qquad (4.23)$$

Therefore, recording projections is equivalent to recording slices of $\tilde{f}$. $f(x, y)$ can be reconstructed from the projections using the inverse radon transform

$$f(x, y) = \int \int \tilde{p}_\theta(q) e^{iq(x \cos(\theta) + y \sin(\theta))} \tilde{h} \mathrm{d}\theta \mathrm{d}q. \qquad (4.24)$$

where $\tilde{h}$ is a filter function that in the ideal case is equal to $|q|$. It is common to modify $\tilde{h}$ to reduce high spatial frequency noise amplification.

The intensity images obtained with an X-ray transmission microscope are exponential functions of the projections of the linear attenuation coefficient distribution, i.e.

$$I_\theta(\xi) = I_0 e^{-\int \mu(\xi \cos(\theta) + \eta \sin(\theta), \xi \sin(\theta) - \eta \cos(\theta)) \mathrm{d}\eta} \qquad (4.25)$$
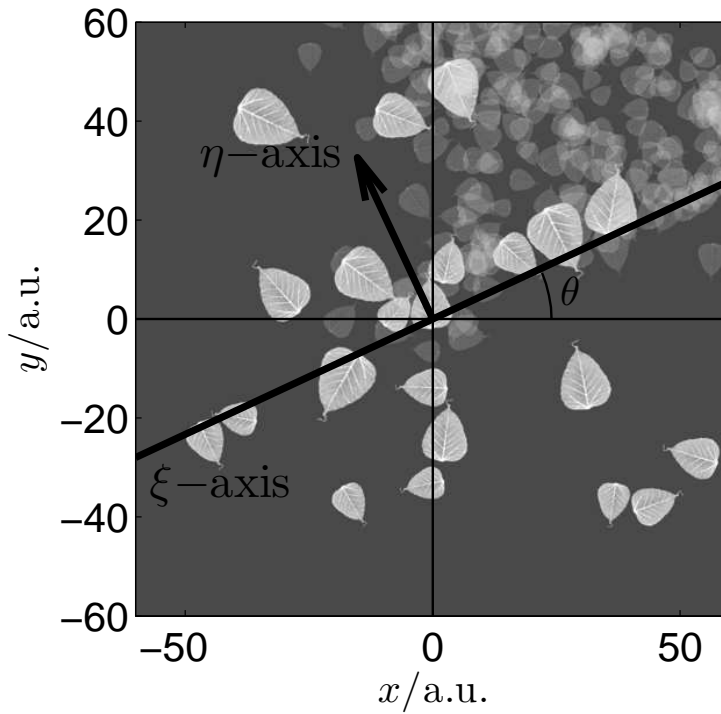
**Figure 4.18:** Illustration of $(\xi, \eta)$-coordinate system.

Thus, $f(x, y)$ corresponds to $\mu(x, y)$, while $p_\theta(\xi)$ corresponds to $-\ln\left(\frac{I_\theta(\xi)}{I_0}\right)$. Ideally, the entire sample should fit inside the field of view, however it is not always possible to meet this condition. Figure 4.19 shows the effect on the tomogram when the sample is too large.
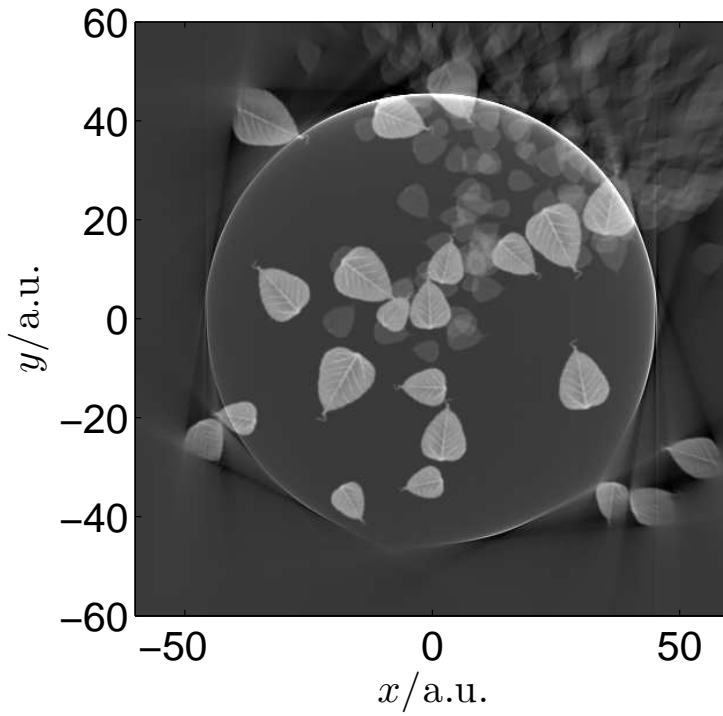
**Figure 4.19:** Illustration of effect of limited field of view.

# Chapter 5

# Zernike phase contrast

Zernike phase contrast (ZPC) [87] is a phase contrast technique that earned Frits Zernike the Nobel prize in physics in 1953. It converts phase modulations into detectable intensity variations in a focused real space image, and is ideal for imaging of weakly absorbing matter. For X-rays, until now, the technique has exclusively been used with microscopes based on Fresnel Zone Plates[56, 79, 19]. In this chapter the working principle will be presented, followed by a brief discussion of some practical considerations regarding implementation.

## 5.1 Working principle

The image formed by an optical system can be regarded as the sum of the scattered wave field, $\psi_{\mathrm{SC}}(x, y)$ and the non-scattered background field, $\psi_{\mathrm{BG}}(x, y)$. In standard microscopy, the scattered wave is $\pi/2$ out of phase with respect to the background wave. The core principle of ZPC is to phase shift the background wave by $\pm\pi/2$ so that it may interfere with the scattered wave, which allows phase modulations by the sample to produce intensity variations in the image. Consider a sample object with thickness function $t(x, y)$. The field on the exit side of the sample can be written

$$\psi'(x, y) = \psi_{\mathrm{BG}} e^{-ik(\Delta\delta - i\Delta\beta)t(x,y)} = \psi_{\mathrm{BG}}(x, y) + \psi_{\mathrm{SC}}(x, y) \qquad (5.1)$$

where $\psi_{\mathrm{BG}}$ is the background field, and

$$\psi_{\mathrm{SC}}(x, y) = \psi(x, y) \left( e^{-ik(\Delta\delta - i\Delta\beta)t(x,y)} - 1 \right) \qquad (5.2)$$

is the field scattered by the sample. If $\beta$ is negligible compared to $\delta$, which is typically the case with X-rays, and if $k\delta t(x, y)$ is small compared to $\pi/2$, then one

may use the approximation

$$\psi_{\text{SC}}(x, y) \approx -ik\delta t(x, y)\psi(x, y) \tag{5.3}$$

The basic idea of ZPC is to apply a phase shift $\phi$ to either $\psi_{\text{SC}}$ of $\psi_{\text{BG}}$. With an ideal imaging system, the intensity image would take the form

$$
\begin{aligned}
I(x, y) &= |\psi_{\text{BG}}|^2 + |\psi_{\text{SC}}|^2 - 2k\delta t(x, y)\text{Re}\left[i\psi_{\text{BG}}\psi_{\text{BG}}^* e^{-i\phi}\right] \tag{5.4}\\
&= |\psi_{\text{BG}}|^2 + |\psi_{\text{SC}}|^2 - 2ka\delta t(x, y)|\psi_{\text{BG}}|^2 \sin(\phi) \tag{5.5}\\
&= |\psi_{\text{BG}}|^2 \left(1 - 2k\delta t \sin(\phi) + (k\delta t)^2\right) \tag{5.6}
\end{aligned}
$$

If $k\delta t$ is small, then the $(k\delta t)^2$-term is small compared to the $k\delta t$-term. Thus choosing $\phi = \pm\pi/2$ yields a significant contrast enhancement. To apply the phase shift, one can take advantage of the fact that the Fourier transform of $\psi_{\text{BG}}$ will be localized near the origin, provided coherent illumination, whereas the Fourier transform of $\psi_{\text{SC}}$ will be spread over a larger area. If a small diameter quarter wave plate is placed on the optical axis in the Fourier plane, the plate will phase shift $\psi_{\text{BG}}$, while letting most of $\psi_{\text{SC}}$ pass unaffected. Positive and negative phase contrast is defined according to the direction of the phase shift of the background. Examples of negative and positive ZPC can be seen in Figure 5.1. For comparison, the Figure also shows the same simulation without any phase plate.

## 5.2    Effect of plate dimensions

Ideally, only $\psi_{\text{BG}}$ should be phase shifted. However, the phase plate will not be able to perfectly discriminate between $\psi_{\text{BG}}$ and $\psi_{\text{SC}}$. A small part of $\psi_{\text{SC}}$ will inevitably be phase shifted along with the background. This gives rise to ringing artefacts around sample features, also called halo artefacts, or shade off effects. The severity of the ringing depends on the radius of the phase plate. The larger the reciprocal space radius, $R_q$, covered by the phase plate, the higher the spatial frequency of the ringing. A rough estimate of the fringe period can be obtained from the approximation $\lambda_{\text{fringe}} \approx 2\pi/R_q$. If the size of the fringes is comparable to the sample object it can become difficult to distinguish real features from artefacts. An illustration of this is shown in Figure 5.2.

The ringing can be reduced to some extent by tapering or smoothing the thickness of the phase plate [24]. Partial coherence will also have a smoothing effect, however, if the coherence ratio is too low, part of the background illumination will miss the phase plate, and will not contribute to the phase contrast. Thus the plate size sets an effective maximum on the coherence ratio.

To evaluate the significance of this type of effects, one may use the simulation method put forth in Appendix B
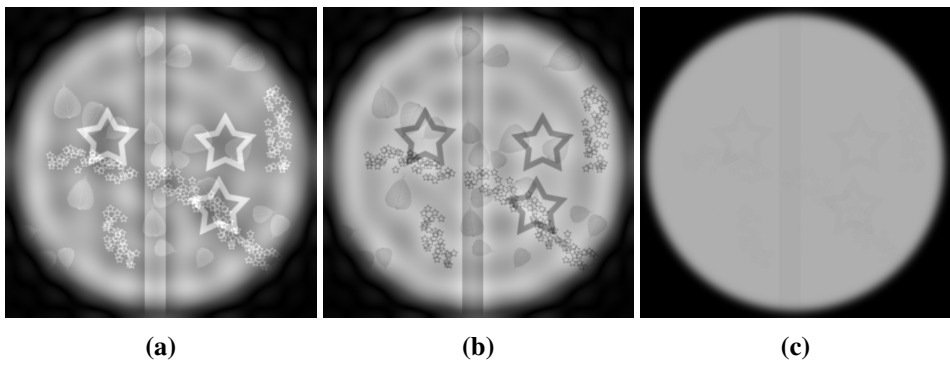
**Figure 5.1:** (a) positive ZPC. (b) negative ZPC. (c) standard microscopy. The simulation consisted of modulating the input field in Fourier space.
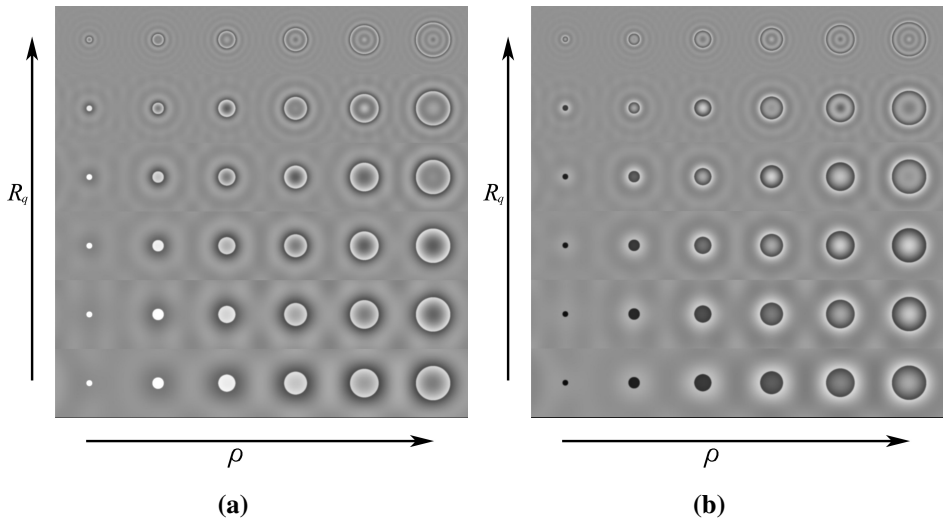


**Figure 5.2:** Effect of phase plate radius on image of discs of varying size. (a) negative ZPC. (b) positive ZPC.

# Chapter 6

# Chromatic aberrations

With the introduction of increased bandwidth of the pink beam comes increased X-ray flux. The drawback, on the other hand, is chromatic aberrations. Due to chromatic aberrations, the extra photons can not be fully exploited. In order to maximize the gain, it is important to understand how chromatic aberration in CRLs responds to changes in different parameters. This chapter is an introduction to chromatic effects in CRLs with chromatic illumination, and introduce the important interplay between noise and resolution. The latter is especially important when considering temporal resolution.

## 6.1 Chromatic aberrations in CRL based Hard X-ray transmission microscopy

A microscope illuminated with a polychromatic beam, will form an image corresponding to the intensity sum of images formed at different photon energies. If the image differs for different energies, the microscope suffers from chromatic aberrations. The focal length of a refractive lenslet depends on the photon energy. Specifically, it follows the relation

$$f \propto E^2. \tag{6.1}$$

This implies that $F$ is energy dependent as well. The microscope may only be in focus for one wavelength. It is convenient to express the photon energy, $E$, in terms of the in-focus reference energy, $E_0$, and the ratio

$$\alpha = \frac{E}{E_0} \tag{6.2}$$

so that the image is in focus when $\alpha = 1$. As $\omega$ is proportional to $f^{-\frac{1}{2}}$, the relationship between $\alpha$ and $\omega$ is

$$\omega = \frac{\omega_0}{\alpha}. \tag{6.3}$$

where $\omega_0$ is the value of $\omega$ at the $E_0$. The energy dependence of $\omega$ will result in an energy dependent RTM, which in turn will result in an energy dependence of $d$ and $\mathcal{M}$. Chromatic aberration is often separated into longitudinal and lateral components, related to the energy dependence of $d$ and $\mathcal{M}$, respectively.

If the bandwidth is sufficiently small, one may linearize $d$ as a function of $\Delta\alpha = \alpha - 1$, i.e.

$$d \approx \left. \frac{\partial}{\partial\alpha} d \right|_{\alpha=1} \Delta\alpha \tag{6.4}$$

The evaluation of $\left. \frac{\partial}{\partial\alpha} d \right|_{\alpha=1}$ will be investigated in section A.2. Under this approximation, the r.m.s. spread of defocus is related to the r.m.s. bandwidth, $\sigma_\alpha$, by

$$\sigma_d = \left. \frac{\partial}{\partial\alpha} d \right|_{\alpha=1} \sigma_\alpha. \tag{6.5}$$

A trade-off exists between $\sigma_{\text{N.A.}}$ and chromatic aberration. While a high $\sigma_{\text{N.A.}}$ increases the diffraction limited resolution, it also disperses the out-of-focus more than with a small $\sigma_{\text{N.A.}}$. Figure 6.1(b) gives an impression of how the LSF and PSF changes with respect to $\sigma_{\text{N.A.}}$. Figure 6.1(a) shows how the resolution behaves with respect to $\sigma_{\text{N.A.}}$. The parameters used in the calculation correspond to a realized microscope [28]. Resolution is here defined as the separation between LSFs that yields a 26.4% contrast, assuming incoherent illumination. As the realistically attainable numerical apertures ($10^{-4} - 10^{-3}$) are currently far short of the optimal values, simply maximizing the $\sigma_{\text{N.A.}}$ will be beneficial for the resolution of pink beam microscopy. This conclusion is further reinforced in Section A.1, where it will be shown that an inverse exists between $\sigma_d$ and $\sigma_{\text{N.A.}}$. The choice of resolution criterion will have influence on the exact shape of the curve, and may in some cases lead to questionable conclusions. An example of such is illustrated in Figure 6.1(b). The blue and the black curve are both assigned a resolution of 192 nm, whereas the black curve yields 130 nm.

The basic idea, however, behind using a pink beam rather than a monochromatic beam is to improve temporal resolution. Rather than optimizing the resolution, it might be more relevant to minimize the exposure time needed to produce an image of sufficient quality. A commonly used criterion for whether or not an object can be reliably detected by a human observer is the Rose criterion [66, 14], which
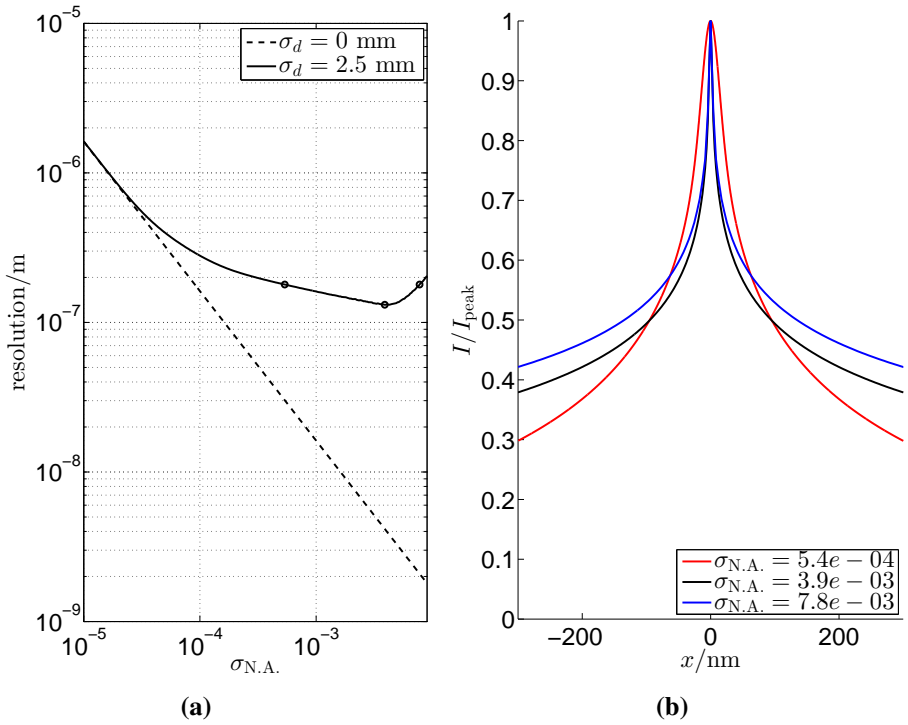
**Figure 6.1:** (a) relation between $\sigma_{\text{N.A.}}$ and resolution. The values of $\sigma_d$ corresponds approximately to a microscope with an objective consisting of 90 Beryllium lenslets with $R = 50$ $\mu$m, and $T = 1.6$ mm, using a FWHM bandwidth of $10^{-2}$, at 17 keV. The monochromatic case was also included for comparison. (b) comparison of LSFs using parameters indicated by the black marks on the red curve in (a). The red and the blue curve are judged to yield the same resolution by the 26.4% contrast criterion.

states that a feature made up of $n_{\text{px}}$ pixels is detectable if the visibility satisfies

$$v = \text{CNR}\sqrt{n_{\text{px}}} >\sim 5, \tag{6.6}$$

where $\text{CNR}$ is the contrast to noise ratio, defined as

$$\text{CNR} = \frac{|I_{\text{f}} - I_{\text{bg}}|}{\sigma_n} \tag{6.7}$$

where $I_f$ and $I_{\text{bg}}$ are the intensity levels in the contrast feature and the background, respectively, and $\sigma_n$ is the noise r.m.s. The significance of feature size, contrast, and noise is illustrated in Figure 6.2.

Assuming the noise is dominated by the shot noise contribution, it will scale as $\sigma_n \propto \sqrt{I_{\text{bg}}}$. As both $I_{\text{f}}$ and $I_{\text{bg}}$ is proportional to the camera exposure time, $t_e$, CNR will be proportional to $\sqrt{t_e}$. The implication for temporal resolution is that smaller objects require longer exposure time than large ones, and that in order to optimize the temporal resolution, one should maximize CNR at the required resolution. This topic is advanced further in Paper 4 [25], where partial coherence is taken into account as well.

It is also of interest to minimize the impact of chromatic aberrations. Derivations have been made on how to minimize the chromatic aberrations of a CRL system. The results can be found in A
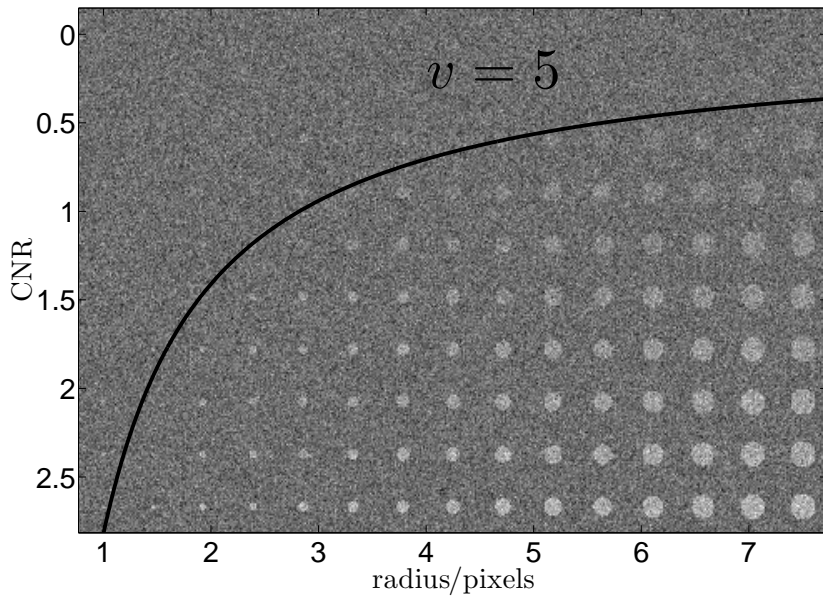
**Figure 6.2:** Illustration of the effect of feature size, contrast, and noise on the visibility of an object. The test pattern is an array of disc objects with varying radius and contrast.

**Part II**

# Results

# Chapter 7

# Papers

# Paper 1

## Correcting lateral chromatic aberrations in non-monochromatic X-ray microscopy

Falch, Detlefs, Di Michiel, Snigireva, Snigirev, and Mathiesen

# Correcting lateral chromatic aberrations in non-monochromatic X-ray microscopy

Ken Vidar Falch,[1] Carsten Detlefs,[2] Marco Di Michiel,[2] Irina Snigireva,[2] Anatoly Snigirev,[3] and Ragnvald H. Mathiesen[1,a)]

[1]*Department of Physics, Norwegian University of Science and Technology, Høgskoleringen 1, 7491 Trondheim, Norway*
[2]*European Synchrotron Radiation Facility, 71 Avenue des Martyrs, 38000 Grenoble, France*
[3]*Immanuel Kant Baltic Federal University, 238300 Kaliningrad, Russia*

Lateral chromatic aberration in microscopy based on refractive optics may be reduced significantly by adjustments to the illumination scheme. By taking advantage of a broadened bandwidth illumination, the proposed scheme could open for x-ray microscopy with spatial resolution in the range 150–200 nm at millisecond frame rates. The scheme is readily implemented and is achievable using only standard refractive x-ray lenses, which has the advantage of high efficiency. It also maximizes the transmission and removes the spatial filtering effects associated with absorption in x-ray lenses. *Published by AIP Publishing.* [http://dx.doi.org/10.1063/1.4960193]

Today microscopy experiments at synchrotrons are performed more or less exclusively with monochromatic radiation, either from a bending magnet or an undulator source. Undulator sources deliver a harmonic comb spectrum, and subsequent monochromatization filters the beam to a bandwidth typically 2–3 orders of magnitude narrower than those of the harmonic undulator peaks. Accordingly, the use of non-monochromatized undulator harmonics would yield two orders of magnitude increase in flux. This could open for new application areas, e.g., for faster structure dynamics to be addressed by *in situ* X-microscopy experiments, under the provision that challenges with increased bandwidth such as chromatic aberrations can be circumvented. The possibility of using combinations of refractive and diffractive optics to construct achromats and apochromats for visible light was pointed out already 3 decades ago.[1] It was not seriously considered for x-rays until the early 2000 s,[2,3] with applications to x-ray telescopes in mind.[4] More recently, microscopy based on Kirkpatrick-Baez mirrors was performed, showing negligible chromatic aberration in the 8–11 keV range, making the technique suitable for spectromicroscopy.[5] Focusing X-ray optics is commonly based either on curved crystal mirrors,[6–8] Fresnel zone plates,[9] or compound refractive lenses (CRLs).[10] Using CRLs for microscopy has the advantage of high efficiency, and scalability to higher energy x-rays,[11] which is beneficial when sample transmission is a limiting factor. While combination of CRLs with diffractive optics can be arranged to correct chromatic aberration, the introduction of a diffractive element in the microscope gives rise to a considerable loss of photons. Focal spots in the 100–200 nm range have been achieved with CRLs at 8.2 keV with a ∼2% bandwidth,[12] which suggests that microscopy with similar resolution is achievable. However, when it comes to focusing, only longitudinal chromatic aberration is important. The work presented here is an investigation into

the possibility of correcting lateral chromatic aberration in microscopy purely based on CRLs.

When using a non-monochromatic beam for microscopy, the final image can be considered to be an intensity sum of images recorded with different photon energies. It can be shown that the CRL focal length, $f \propto E^2$, where $E$ is the photon energy.[13] Consider $E_0$ as the reference energy at which the microscope is in focus. Photons with energy $E \neq E_0$ will produce defocused and scaled variants of the in-focus image. The defocusing and scaling are conventionally referred to as longitudinal and lateral chromatic aberration, respectively.

Let the ray transfer matrix for the microscopy setup depicted in Figure 1(a) be

$$M = \begin{bmatrix} \mathcal{M} & \mathcal{M}d \\ \mathcal{M}c & \mathcal{M}^{-1} + dc\mathcal{M} \end{bmatrix}. \quad (1)$$

As was shown by Nazarathy and Shamir,[14] the operation of a system represented by a matrix such as $M$ on an input field is
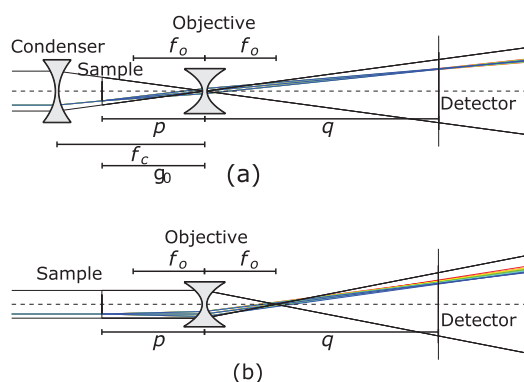


FIG. 1. (a) Microscope with beam focused into the objective lens and (b) Microscope with parallel beam illumination. Notice the distribution of the rays on the detector plane.

a)Author to whom correspondence should be addressed. Electronic mail: ragnvald.mathiesen@ntnu.no

to propagate it a distance $d$, scaling it laterally by a factor $\mathcal{M}$, and applying a quadratic phase shift related to $c$. The latter is unimportant for imaging, provided sufficient exposure time is used. Accordingly, the energy dependence of $\mathcal{M}$ and $d$ is related to lateral and longitudinal chromatic aberrations, respectively. Let $\alpha = \frac{E}{E_0}$ be a measure of the deviation from the reference energy. Under the thin lens approximation

$$M = \begin{bmatrix} 1 - \dfrac{q}{f_0^o \alpha^2} - \dfrac{\left(1 - \dfrac{q}{f_0^o \alpha^2}\right)p + q}{f_0^c (\alpha^2 - 1) + g_0} & \left(1 - \dfrac{q}{f_0^o \alpha^2}\right)p + q \\[3ex] -\dfrac{1}{f_0^o \alpha^2} - \dfrac{1 - \dfrac{p}{f_0^o \alpha^2}}{f_0^c (\alpha^2 - 1) + g_0} & 1 - \dfrac{p}{f_0^o \alpha^2} \end{bmatrix}. \tag{2}$$

Here, $f_0^o$ and $f_0^c$ are the $E_0$ focal lengths of the objective and condenser lens, respectively. $g_0$ is the distance from the $E_0$ focal spot of the condenser to the sample. $p$ and $q$ are the distances from the objective lens to the sample and detector, respectively. Under the assumption of a narrow bandwidth, $\mathcal{M}$ and $d$ may be Taylor expanded about $\alpha = 1$ and $g_0 = p$ to yield

$$\mathcal{M} = \mathcal{M}_0 \left(1 - 2\frac{\Delta g_0}{f_0^o}\Delta\alpha - 4\frac{f_0^c}{f_0^o}\Delta\alpha^2\right) + O(\Delta\alpha^3) + O(\Delta\alpha^2 \Delta g_0) + O(\Delta\alpha \Delta g_0^2) \tag{3}$$

and

$$\frac{d}{\alpha} = -2p\left(1 + \frac{p}{q}\right)\Delta\alpha + O(\Delta\alpha^2) + O(\Delta\alpha^2 \Delta g_0), \tag{4}$$

where $\mathcal{M}_0 = -\frac{q}{p}$, $\Delta\alpha = \alpha - 1$, and $\Delta g_0 = g_0 - p$. The motivation for expressing $d/\alpha$ rather than just $d$ is to normalize the propagation distance at $E$ to the equivalent distance at $E_0$. By choosing $g_0 = p$, $\mathcal{M}$ becomes energy independent to the first order in $\Delta\alpha$. Taylor expansion of the parallel beam case, which is obtained by letting $g_0$ go to infinity, results in

$$\mathcal{M} = \mathcal{M}_0\left(1 - 2\frac{p}{f_0^o}\Delta\alpha + 3\frac{p}{f_0^o}\Delta\alpha^2\right) + O(\Delta\alpha^3). \tag{5}$$

Thus, if the energy bandwidth is small, the lateral chromatic aberration can be reduced by a factor $\frac{\Delta g_0}{p}$. Eq. (4), which is also valid in the parallel beam case, shows that the longitudinal chromatic aberration at small $\Delta\alpha$ is minimized by keeping $p$ as small as possible, and to a lesser extent by keeping $\frac{p}{q}$ as small as possible. This in turn implies that $f_0^o$ should be relatively short. Obviously, when focal lengths become too short with respect to the length of the CRL, the thin lens approximation becomes invalid. However, the CRLs employed here are not long enough to make a significant deviation from the thin lens approximation. Therefore, a more comprehensive treatment, accounting also for lens lengths,[13,15–18] has been omitted from Eqs. (2)–(5) but can be found as supplementary material.

A test experiment has been performed at the ID06 beamline at the European Synchrotron Radiation Facility (ESRF). The output spectrum of undulator sources is dominated by a peak at the fundamental photon energy, accompanied by odd harmonics. In the current experiment, a fundamental photon energy of 17.2 keV was used. Upstream to downstream, the setup consisted of the undulator source, a multilayer mirror, a diffuser, a condenser CRL, the sample, an objective CRL, a pair of slits, and an x-ray imaging detector. The mirror was a Ru/B$_4$C multilayer with a d-spacing of 5.40 nm and a bandwidth of $\frac{\Delta E}{E} = 4 \times 10^{-2}$, significantly larger than the bandwidth of the undulator peak, measured to be $\frac{\Delta E}{E} = 1.3 \times 10^{-2}$ from the power spectrum shown in Figure 2. The condenser and objective CRLs consisted of 32 and 84 double concave lenslets, respectively. Each lenslet had an apex radius of 50 $\mu$m. In the condenser, the spacing between lenslets was 2 mm, while the objective was a mix of $14 \times 2$ mm and $70 \times 1.6$ mm thick lenslets. The numerical aperture of the objective CRL was estimated to be $7.1 \times 10^{-4}$ (HWHM) by a ray tracing method[18] which included the physical aperture. In order to suppress speckles and smooth out features in the incident illumination, a 1.2 mm thick diffuser disc made from amorphous carbon was placed approximately 10 cm upstream of the condenser CRL. About 10 cm downstream of the objective, a pair of slits were placed. With an opening of 100 $\mu$m × 100 $\mu$m, the slits had no observable effect on the resolution but were useful for blocking a large portion of x-rays from the higher harmonics of the undulator. The camera was a PCO dimax CMOS, equipped with 10× visible light optics and a 24.5 $\mu$m thick Eu-doped GdGa-garnet crystal scintillator. Relevant distances used were $f_0^o = 270$ mm, $q = 2600$ mm, $p = 300$ mm, and $f_0^c = 670$ mm, yielding $4f_0^c/f_0^o = 9.9$ and $d \approx 670$ mm × $\Delta\alpha$. Evaluating $d$ at the FWHM-energies gives $d_{\text{FWHM}} = \pm 5.4$ mm. The test sample was a 4 $\mu$m thick microscopy Copper mesh with 8 $\mu$m diameter circular holes.

Figure 3 shows the experimental results with and without condenser lens. There are two main differences between the images. In the image recorded with the parallel beam (Figure 3(a)), large fringes can be seen near the edges of the holes, presumably stemming from a combination of chromatic aberration and inhomogeneous filtering in the objective lens.[19] In the image recorded with the condenser (Figure 3(b)), the fringes are no longer visible. Focusing the beam into the objective lens makes the filtering homogeneous and reduces the lateral chromatic aberration. The second difference is in the radial blurring effect associated with lateral chromatic aberration. In the parallel beam case, one can see that the holes appear smeared. The smearing is almost absent
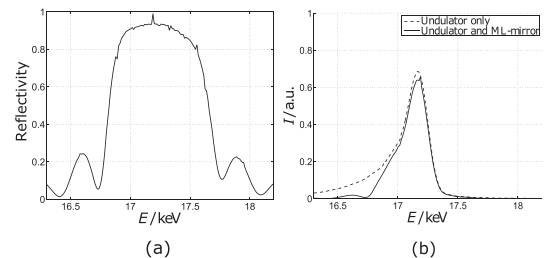


FIG. 2. (a) Measured multilayer reflectivity at the specific incident angle used in the experiment and (b) Power spectrum of the undulator and reflected spectrum.

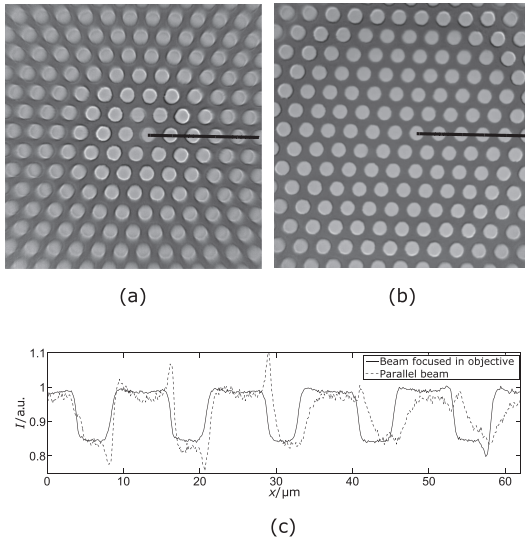(a)                                        (b)



(c)

FIG. 3. (a) and (b) are images recorded with parallel illumination and with illumination focused in the objective, respectively. (c) Intensity plots sampled from the black lines in (a) and (b).

in the center of the image but becomes more and more pronounced towards the image periphery. With the beam focused in the objective, radial blurring more or less vanishes. A more intuitive physical explanation for the working principle of the suggested scheme can be found by taking into account that the angular distribution of the X-rays scattered of the sample typically is peaked in the forward direction. If the illumination is aimed at a part of the objective where it will be strongly refracted, the location of the peak in the detector plane will depend on the energy, as illustrated in Figure 1(b). By aiming the illumination at the center of the objective, as in Figure 1(a), the peaks show up in the same position in the detector for all energies. The field of view (FOV) as determined by the full width at half maximum of the illumination intensity was $113 \mu m$. A drawback of the scheme is that the FOV becomes limited by the diameter of the condensed beam as opposed to the objective aperture. Larger aperture condensers are desirable for increasing the FOV.

By comparing the lines in Figure 3(c), it can be seen that there appears to be a discrepancy in the magnification of the two images. The image recorded with the parallel illumination is approximately 1.5% larger. It is not clear whether this is a real discrepancy or simply due to confusion caused by the fringes. If the microscope is perfectly focused, one would expect the magnification to be independent of the illumination. A 1.5% discrepancy would indicate that the sample was placed approximately 1.5% too far away from the objective lens, assuming that $\Delta g$ is small. With $p \approx 306$ mm, this comes to 4.6 mm defocusing, which is not unreasonable considering the bandwidth. The fact that the illumination can only change the magnification if the microscope is out of focus might serve as a basis for a simple focusing algorithm. This would of course be applicable to both monochromatic and polychromatic beams.

In the corners of the image recorded with a condenser lens, one can still see that some fringes persist. This is presumably caused by illumination not focused to the correct distance, which may not be unlikely considering that the focal spot could have been slightly off. It is worth mentioning though that in the analysis presented above, no efforts have been made to account for the effects of the diffuser. It could be expected that scattering by the diffuser, in combination with a finite beam diameter, could influence the location of the effective focal spot. Further experiments would be required to determine the exact effect of the diffuser disc.

To evaluate the validity of the presented theory in practice, the microscope was replicated with a Si 111 double crystal monochromator replacing the multilayer mirror. Due to geometrical constraints, the exact distance from the sample to the detector could not be reproduced. The new distances were $p = 304$ mm and $q = 3200$ mm, resulting in a reference magnification of $\mathcal{M}_0 = -10.4$ when the length of the objective is taken into account. Two series of images with different photon energies were recorded, one with parallel beam illumination and one with illumination focused in the objective. The results are presented in Figure 4, along with estimates based on ray transfer matrices for both thin and long lenses, following the procedure of Simons *et al.*[18] The magnification of each image was estimated by measuring the distance between two features in the images. Two second order polynomials were fitted to the experimental data, and their intersection was taken as the reference length. The intersection was found at $E = 17.103$ keV. The two best focused images, judged by inspection, were found at $E = 17.10$ keV and $E = 17.12$ keV. Note that the thin lens estimate was normalized by $\mathcal{M}_0 = -10.5$ which is slightly larger in magnitude than in the long lens case. The experimental curves fit well to the ray trace estimates. In the focused beam case, the largest discrepancies between model and polynominal fit can be attributed to $\Delta g_0$ being in the range of 30–40 mm. It is evident that long lens calculations give an improved fit for the parallel beam case. In conclusion, the principle behind the presented lateral chromatic aberration correction scheme appears to be valid.
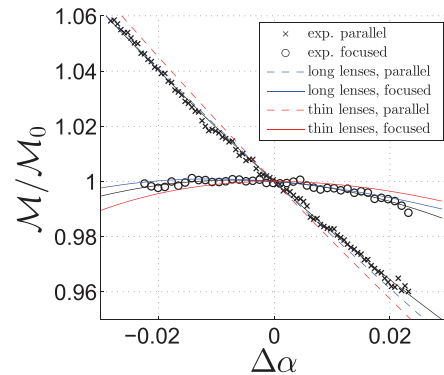


FIG. 4. Theoretical and experimentally determined magnification of images at different photon energies. The black curves are second order polynomial fits.

See supplementary material for calculation of long lens relative magnification.

[1]T. Stone and N. George, Appl. Opt. **27**, 2960 (1988).

[2]G. K. Skinner, AIP Conf. Proc. **587**, 855 (2001).

[3]G. K. Skinner, Appl. Opt. **43**, 4845 (2004).

[4]G. K. Skinner, Z. Arzoumanian, W. C. Cash, N. Gehrels, K. C. Gendreau, P. Gorenstein, J. F. Krizmanic, M. C. Miller, J. D. Phillips, R. D. Reasenberg, C. S. Reynolds, R. M. Sambruna, R. E. Streitmatter, and D. L. Windt, Proc. SPIE **7011**, 70110T (2008).

[5]S. Matsuyama, Y. Emi, H. Kino, Y. Kohmura, M. Yabashi, T. Ishikawa, and K. Yamauchi, Opt. Express **23**, 9746 (2015).

[6]O. Hignette, P. Cloetens, G. Rostaing, P. Bernard, and C. Morawe, Rev. Sci. Instrum. **76**, 063709 (2005).

[7]W. J. Liu, G. E. Ice, J. Z. Tischler, A. Khounsary, C. Liu, L. Assoufid, and A. T. Macrander, Rev. Sci. Instrum. **76**, 113701 (2005).

[8]H. Mimura, S. Handa, T. Kimura, H. Yumoto, D. Yamakawa, H. Yokoyama, S. Matsuyama, K. Inagaki, K. Yamamura, Y. Sano, K. Tamasaku, Y. Nishino, M. Yabashi, T. Ishikawa, and K. Yamauchi, Nat. Phys. **6**, 122 (2010).

[9]W. L. Chao, B. D. Harteneck, J. A. Liddle, E. H. Anderson, and D. T. Attwood, Nature **435**, 1210 (2005).

[10]C. G. Schroer, F. E. Brack, R. Brendler, S. Honig, R. Hoppe, J. Patommel, S. Ritter, M. Scholz, A. Schropp, F. Seiboth, D. Nilsson, J. Rahomaki, F. Uhlen, U. Vogt, J. Reinhardt, and G. Falkenberg, Proc. SPIE **8848**, 884807 (2013).

[11]S. D. Shastri, P. Kenesei, and R. M. Suter, Proc. SPIE **9592**, 95920X (2015).

[12]F. Seiboth, A. Schropp, R. Hoppe, V. Meier, J. Patommel, H. J. Lee, B. Nagler, E. C. Galtier, B. Arnold, U. Zastrau, J. B. Hastings, D. Nilsson, F. Uhlen, U. Vogt, H. M. Hertz, and C. G. Schroer, in Proceedings of the 22nd International Congress on X-Ray Optics and Microanalysis (2014), Vol. 499, p. 012004.

[13]B. Lengeler, C. Schroer, J. Tummler, B. Benner, M. Richwin, A. Snigirev, I. Snigireva, and M. Drakopoulos, J. Synchrotron Radiat. **6**, 1153 (1999).

[14]M. Nazarathy and J. Shamir, J. Opt. Soc. Am. **72**, 356 (1982).

[15]V. G. Kohn, JETP Lett. **76**, 600 (2002).

[16]V. G. Kohn, J. Exp. Theor. Phys. **97**, 204 (2003).

[17]I. I. Snigireva, V. G. Kohn, and A. A. Snigirev, Proc. SPIE **5539**, 218 (2004).

[18]H. Simons, F. Stohr, J. Michael-Lindhard, F. Jensen, O. Hansen, C. Detlefs, and H. F. Poulsen, Opt. Commun. **359**, 460 (2016).

[19]C. G. Schroer, B. Benner, T. F. Gunzler, M. Kuhlmann, B. Lengeler, C. Rau, T. Weitkamp, A. Snigirev, and I. Snigireva, Proc. SPIE **4503**, 23 (2002).

# Paper 2

## Zernike phase contrast in high-energy X-ray transmission microscopy based on refractive optics

Falch, Lyubomirskij, Casari, Detlefs, Snigirev, Snigireva, Di Michiel, and Mathiesen

# Zernike phase contrast in high-energy x-ray transmission microscopy based on refractive optics

KEN VIDAR FALCH[A], MIKHAIL LYUBOMIRSKIJ[B], DANIELE CASARI[A], ANATOLY SNIGIREV[C], IRINA SNIGIREVA[B], CARSTEN DETLEFS[B], MARCO DI MICHIEL[B], AND RAGNVALD H. MATHIESEN[A,*]

[a]Norwegian University of Science and Technology, Department of physics, Høgskoleringen 1, 7491 Trondheim, Norway
[b]European Synchrotron Radiation Facility, 71 Avenue des Martyrs, 38000 Grenoble, France
[c]Immanuel Kant Baltic Federal University, 238300 Kaliningrad, Russia

## ABSTRACT

Contrast enhancement by use of Zernike phase contrast for x-ray microscopy based on refractive optics is demonstrated. The phase contrast was achieved using only compound refractive lenses fitted with phase elements, circumventing the flux loss associated with the use of an annular diaphragm. The resolution is demonstrated to be sub-micron, and can be improved using already existing technology. The possibility of combining the technique with polychromatic radiation is considered, and a preliminary experiment was performed, with positive results.

## 1. Introduction

X-ray microscopy is a powerful technique that allows non-destructive study of a wide range of natural and man-made objects with sub-micron spatial resolution. In the most straight forward implementation, the main contrast mechanism is absorption. Consequently, it can be difficult or impossible to obtain high quality images in cases where the absorption contrast is weak. Zernike phase contrast (ZPC) is a microscopy technique that produces phase contrast by converting phase modulations in the image into detectable amplitude modulations. It has been used frequently with visible light optics since its introduction in 1942[1]. With X-rays, ZPC microscopy was first demonstrated in 1994 at photon energies ~0.5 keV, employing Fresnel Zone Plates (FZPs)[2]. Similar FZP based setups have since been used to obtain ZPC microscopy images with resolution in the 40-100 nm range at energies 4-8 keV[3-5]. Scanning ZPC has also been demonstrated with promising results, allowing for spectroscopic mapping [6]. Furthermore, efforts have been made to extract quantitative phase information by alternating between negative and positive ZPC. Numerical results employing this technique were published quite recently [7].

The potential of ZPC makes it a promising direction for development of microscopy based on Compound Refractive Lenses (CRLs). While existing CRLs cannot match FZPs when it comes to resolution, they can be used at photon energies well above those currently feasible with FZP optics. Use of high energy x-rays is advantageous for microscopy of e.g. inorganic samples of appreciable thickness in order to have a usable amount of transmission through the sample, and often also to reduce sample alteration or damage associated with ionization. Microscopy based on CRLs has been demonstrated at energies up to 50 keV[8], and could quite readily be extended to operate at even higher energies. ZPC at 25 keV was reported in 2003, based on refractive capillary lenses, and represents until now the only X-ray ZPC study reported based on refractive optics. Since then, however, refractive x-ray optics has vastly improved.

## 2. Experimental setup

An experiment was performed at the micro optics test bench at beamline ID06 at the European Synchrotron Radiation Facility. The experimental setup is illustrated in Figure 1. The microscope was operated on an undulator source with 17 keV radiation selected by liquid nitrogen cooled Si 111 double-crystal fixed exit monochromator , and with the sample and detector placed 800 mm upstream and 4200 mm downstream of the objective, respectively. The detector was a pco.2000 CCD camera equipped with 10x visible light optics and a Eu-doped GdGa-garnet crystal scintillator. Both the condenser and objective were made by assemblies of double concave 50 μm apex radius Be-lenslets. The condenser consisted of 16 lenslets with 2 mm spacing, resulting in a total thickness of 32 mm, while the objective contained 32 lenslets with thickness 1.6 mm. In the objective, a 5 mm spacer was inserted between the 16th and the 17th lenslet with its interior open for the beam to pass through and so that a phase plate could be suspended into the opening from above. Ideally, the phase element would be attached and aligned to the spacer. The total length of the objective, including the spacer, was 56 mm.
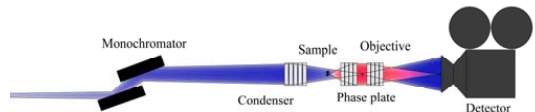


Fig 1: Schematic illustration of the experi,mental setup.

The phase plate was a 5 μm thick 30 μm diameter platinum disc mounted on a silicon nitride membrane, which at 17 keV induces a phase shift of $1.68\pi$.

The numerical aperture of the objective was estimated to N.A.=$2.8\times10^{-4}$ considering the marginal rays from the sample. The geometrical aperture was significantly smaller than the Gaussian effective aperture. The root-mean-square (RMS) source size at ID06 is 415 µm and 8.6 µm in the horizontal and vertical directions, respectively. The distance between the condenser and the source was 53 m while the distance between the condenser and the objective was 1.3 m. A rough estimate of the spot size on phase plate, $R_{bg}$, can be obtained by multiplying the horizontal source size by the demagnification of the source image, which yields $R_{bg}\approx10$ µm.

Another test experiment was performed at beamline ID31 at the European Synchrotron Radiation Facility. The setup was similar to the previous one with the sample and detector placed 425 mm and 5000 mm upstream and downstream of the objective, respectively. The objective and condenser contained 87 and 32 Be-lenslets, respectively, each with 50 µm apex radius. In this experiment the incident beam photon energy was 22.5 keV selected by two multilayer mirrors, which results in a bandwidth of 0.3 % rather than the typical 0.01% bandwidth from a Si(111) double-crystal monochromator. A collector lens consisting of 5 Be-Lenslets with 200 µm apex radii was situated about 31 m from the source, which was 117 m upstream of the sample position. The main objective for this study was to verify that ZPC imaging could be carried out with satisfactory results also with non-monochromatic radiation.

If ZPC is to be employed for ultra-fast imaging, like e.g. time-resolved in situ tomography, it would be an advantage if it could be used in combination with broadband radiation. However, the significantly increased photon flux could potentially cause substantial heating or even melting of the phase element, in particular taking into account that the phase element would be placed in the focal spot of the condenser. Therefore, rather than using a phase plate, a hole was made in the center of one of the lenslets. This lenslet will be referred to as a Zernike lenslet. The nominal web thickness of the lenslet was 30 µm, which gives the background wave a phase shift of $\varphi$=-$\pi$/2-0.23$\pi$. The diameter of the hole was 20 µm. After the microscope was aligned with a standard CRL objective, the central lenslet was replaced by the Zernike lenslet.

## 3. Theory

The ray transfer matrix for a complete microscope, from sample to detector, is

$$M_p = \cos(\omega L)\begin{bmatrix} 1-\dfrac{q}{F} & p+q+\dfrac{pq}{F}+\dfrac{1}{F\omega^2} \\ -\dfrac{1}{F} & 1-\dfrac{p}{F} \end{bmatrix} \tag{1}$$

where $p$ and $q$ are the distances from the sample to the objective entrance and from the objective exit to the detector, as illustrated in Figure 2, and $\omega = (fT)^{-\frac{1}{2}}$, where $f$ and $T$ are the focal length of a single lenslet and the spacing between lenslets, respectively. $F$ is the focal length measured from the exit of the lens, given by

$$F = \frac{1}{\omega\tan(\omega L)} \tag{2}$$

with $L$ as the length of the CRL. The imaging condition is met when the upper right element of $M_p$ vanishes, i.e. when

$$\frac{1}{F} - \frac{1}{p} - \frac{1}{q} - \frac{1}{pqF\omega^2} = 0. \tag{3}$$

The image formed by a microscope can be considered as a sum of the scattered wave field and the non-scattered background wave field. In absorption contrast, the scattered wave is approximately $\pi$/2 out of phase with respect to the background wave, assuming small phase variations in the sample. The core principle of ZPC is to phase shift the background wave by ±$\pi$/2 so that it may interfere with the scattered wave. This way, phase variations in the scattered wave can produce intensity variations in the final image. The phase shift can be achieved by placing a phase shifting element, such as a plate- or ring structure, in the Fourier plane where the scattered wave appears as the Fourier transform of the sample and the background wave comes to a focus. In the Fourier plane the scattered wave and background wave are separated, allowing the phase element to discriminate between the two. In the conceptually simplest form of ZPC imaging, the sample is illuminated by a coherent plane wave. In this case, the ideal phase element would be a disc placed in the back focal plane of the objective. By adding a condenser lens upstream of the sample, the focus of the background wave, and thus the ideal place for the phase element, is moved along the optical axis.
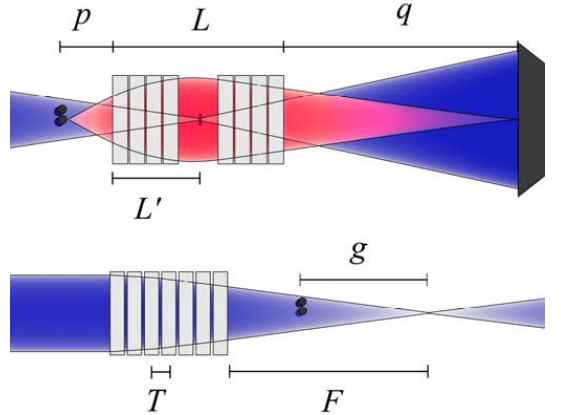


Fig 2: Illustration of the meaning of CRL parameters.

Fringes related to absorption in the objective are common artefacts in CRL-based microscopy[9]. The severity of the effect increases with decreasing effective objective aperture and with the distance from the sample feature to the optical axis. At high energies, where the effective aperture for a given resolution is likely to be smaller, the effect is expected to become more pronounced. The fringes occur because the Fourier plane is not located in the effective aperture stop plane. Often in CRL microscopy, the objective lens itself will act as the aperture stop. The fringes can be removed by moving the Fourier plane to the effective aperture stop. This is equivalent to aligning the background wave with the principle rays, which can be done with the help of a condenser lens. The principle ray through a system of CRLs without diaphragms is the ray that maximizes the transmission from the sample plane to the image plane. In most cases, simply focusing the background wave somewhere inside the objective is good enough.

In cases with long objectives, the principle rays can be determined by finding the initial ray angle that maximizes the transmission. The transmission of a ray through a CRL is a Gaussian function of position, $r$, and angle, $w$, of the ray at the objective entrance.[Extended formalism for simulating compound refractive lens-based x-ray microscopes] It may therefore be expressed as

$$t(\mathbf{x}) = e^{-\mu T_w N} e^{-\frac{1}{2}\mathbf{x}^T \Sigma^{-1} \mathbf{x}} \quad , \tag{4}$$

Where $T_w$ is the web thickness, $\mu$ is the mass attenuation coefficient of the CRL material, and $\mathbf{X}$ is a ray vector with $r$ and $w$ as its first and second element, respectively. and $\Sigma^{-1}$ is a 2×2 matrix whose elements depend on the CRL parameters. Specifically

$$\Sigma^{-1} = \mu \begin{bmatrix} \omega(\omega L + \frac{1}{2}\sin(2\omega L)) & \sin^2(\omega L) \\ \sin^2(\omega L) & \dfrac{\omega L - \frac{1}{2}\sin(2\omega L)}{\omega} \end{bmatrix}. \tag{5}$$

From this, the transmission of a ray from the sample plane can then be found by mapping them to the objective entrance. The mapping is done by multiplying $\mathbf{x}$ with the free propagation matrix

$$\mathbf{R}(p) = \begin{bmatrix} 1 & p \\ 0 & 1 \end{bmatrix}. \tag{6}$$

Substituting $\mathbf{x}_i = \mathbf{R}(p)\mathbf{x}$ into (4) yields

$$t_i(\mathbf{x}_i) = e^{-\mu T_w N} e^{-\frac{1}{2}\mathbf{x}_i \Sigma_i^{-1} \mathbf{x}_i} \quad , \tag{7}$$

where

$$\Sigma_i^{-1} = \mathbf{R}^T(p)\Sigma^{-1}\mathbf{R}(p) . \tag{8}$$

For a given $r$, the angle $w_p$ of the principle ray must be the $w_0$ that maximizes $t_0$. This angle can be expressed in terms of the elements of $\Sigma_i^{-1}$ as

$$w_p = -\frac{\Sigma_{i,(1,2)}^{-1}}{\Sigma_{i,(2,2)}^{-1}} r_0 . \tag{9}$$

Let $g$ be the distance from the sample to where the illumination would come to a focus if objective lens was not present. By choosing

$$g = -\frac{r_0}{w_p} = \frac{\Sigma_{0,(2,2)}^{-1}}{\Sigma_{0,(1,2)}^{-1}} , \tag{10}$$

the illumination is aligned with the principle rays. By ray tracing, the distance $L'$ from the objective entrance to the Fourier plane can be related to $g$ by

$$g = p + \tan(\omega L')/\omega , \tag{11}$$

which may be satisfactory approximated by $g \approx p + L'$ for short or weakly refracting CRLs.

In order to determine the appropriate size of the phase plate it is necessary to relate the spatial displacement in the Fourier plane to reciprocal components of the sample transmission function. For this, it is convenient to calculate the ray transfer matrix $M'$ that maps rays from the sample plane to the Fourier plane.

$$M' = \begin{bmatrix} \cos(\omega L') & \dfrac{\sin(\omega L')}{\omega} \\ -\omega\sin(\omega L') & \cos(\omega L') \end{bmatrix} \begin{bmatrix} 1 & p \\ 0 & 1 \end{bmatrix} \begin{bmatrix} 1 & 0 \\ -\dfrac{1}{g} & 1 \end{bmatrix}$$
$$= \begin{bmatrix} 0 & p\cos(\omega L') + \dfrac{\sin(\omega L')}{\omega} \\ \dfrac{\omega}{\sin(\omega L')} - \dfrac{1}{p\cos(\omega L')} & \cos(\omega L') - \omega p \sin(\omega L') \end{bmatrix} \tag{12}$$

A displacement $\mathbf{r}_{FT}$ in the Fourier plane can then be related to the reciprocal coordinate $\mathbf{q}$ by

$$\mathbf{q} = \frac{k}{B'}\mathbf{r}_{FT} \tag{13}$$

where $k = 2\pi/\lambda$ is the wavenumber, $\lambda$ the wavelength, and

$$B' = p\cos(\omega L') + \sin(\omega L')/\omega \tag{14}$$

is the upper right element of $M'$. The mapping of the phase plate radius $R_p$ to the radius $R_q$ of the affected region in reciprocal space is

$$R_q = \frac{k}{B'} R_p , \tag{15}$$

The lower limit of $R_p$ is determined by the numerical aperture of the condensing optics, the longitudinal alignment precision, and the illumination coherence length. At synchrotrons, assuming no diffusing element is being used, the coherence length is mainly related to the angular source size, which gives rise to a smearing of the intensity profile in the Fourier plane. As a result, the phase plate cannot effectively discriminate between the background and scattered wave when scattering angles become comparable to the angular source size. This implies that at high energies, the source size may have to be taken into consideration.

The minimum size of $R_p$ is related to the size of the background wave in the Fourier plane. It is assumed that the beam is condensed by a CRL with Gaussian aperture, and that the root-mean-square (RMS) source size is $\sigma_s$. Hence, the RMS size of the background wave can be expressed

$$\sigma_{bg}^2 = \sigma_s^2 m_s^2 + \Delta g^2 \sigma_{N.A.}^2 + \frac{1}{4k^2 \sigma_{N.A.}^2} , \tag{16}$$

where $m_s$ is the source demagnification, $\Delta g$ is the misalignment between the Fourier plane and phase element, and $\sigma_{N.A}$ is the RMS of the numerical aperture of condenser combined with any objective lenslets upstream of the phase plate. The third term on the right hand side of (16), relates to the diffraction limit, and is practically negligible. Although this expression is specific to phase discs, the same qualitative results are expected for phase elements of other shapes. As a Gaussian function is non-zero in the whole domain, the phase plate is defined to be covering the beam when

$$R_p = C\sigma_{bg} \tag{17}$$

is satisfied, corresponding to a coverage of the beam intensity profile at a $C \cdot \sigma$ level when the beam is centered on the phase plate.

The upper limit of $R_p$ is not as sharply defined as the lower limit. The larger the object, the smaller the phase plate needs to be. Although the shape of the object matters, a reasonable rule of thumb is to keep $R_q \rho \approx 1$[10], where $\rho$ is the radius of the largest object required to be fringe free. In real space, this translates to a maximum plate radius of

$$R_{p,max} \approx \frac{B'}{k\rho} \qquad (18)$$

The pending question is how $R_{p,max}$ develops with increase in the photon energy. For a given energy, $B'$ depends on the parameters of the objective as well as the geometry of the setup. A complete mapping of all possibilities is not reasonable as constraints set by the ability to produce lenslets with certain thicknesses and apex radii in the end will be the real limiting factors. Figure 3 was produced assuming Be-lenslets with $T=1.6$ mm and $R_a=50$ µm, corresponding to the most readily available Be-lenslets at present. The figure shows $B'/k$ as a function of the diffraction limit $r_d$ for different energies. The calculation was done in the limit of infinite magnification, which maximizes the diffraction limit and is equivalent to $p=F$.
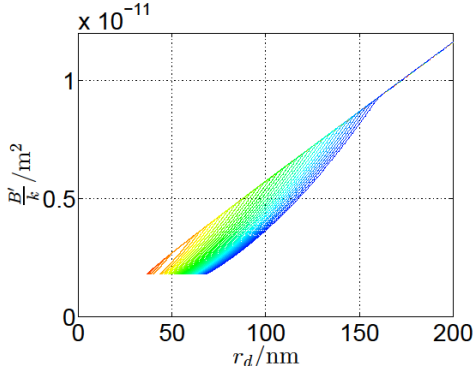


Fig 3: B'/k as a function of $r_d$. The energy range is 15-100 keV. There is a 2.5 keV gap between each line. The red and blue lines at the extremes represent 15 keV and 100 keV, respectively. The calculation was done by estimating B'/k and $r_d$ in the limit of infinite magnification. It is assumed that the illumination is focused so that the non-scattered wave follows the principle rays, in accordance with to (10). The common asymptote is related to the geometrical aperture, and can be calculated as B'/k.≈A$r_d$/(0.61·4π), where A is the geometrical aperture.

For it to be possible to satisfy both the upper and lower constraint one must have $C\sigma_{bg}<2\pi B'/k\rho$. The maximum photon energy where this occurs iss

$$E_{max} = 2\pi\hbar c \frac{B'}{C\sigma_{bg}\rho} \qquad (19)$$

Where $\hbar$ is the reduced Planck's constant and $c$ is the speed of light in vacuum. It should be kept in mind that in practice $B'$ as well as $m_s$ will be energy dependent. .

It was recently demonstrated that lateral chromatic aberration is corrected by using the illumination scheme considered here [latt chrom lett]. The possibility of using ZPC with non-monochromatic illumination with band width is in the range $\Delta E/E\sim 10^{-2}$, commonly referred to in the synchrotron radiation community as a pink beam, will now be considered. A numerical experiment considering a CRL microscope with unit magnification and parallel pink beam illumination has already givenpromising results [11]. The two main concerns when it comes to ZPC with a pink beam is the energy dependence of both the phase shift induced by the phase plate, and the spread of Fourier planes due to the chromaticity of the condenser.

The phase shift, $\varphi$, induced by the phase plate is proportional to $\delta$, which in turn is proportional to $E^{-2}$. The amplitude of the intensity modulation due to interference between scattered and background wave is proportional to the deviation $\tau = \sin(\varphi)$. Let the phase shift induced at the central energy in the $\Delta E$ energy range be denoted by $\varphi_0$. The spread in phase shifts is

$$\Delta\varphi \approx 2\varphi_0 \frac{\Delta E}{E} \qquad (20)$$

Using $\Delta E/E=10^{-2}$, assuming $\varphi_0=\pi/2$, and evaluating $\tau$ at the marginal energies of the spectrum yields

$$\tau = \cos\left(\tfrac{1}{2}\Delta\varphi\right) \approx 1-10^{-4}\tfrac{\pi^2}{4} . \qquad (21)$$

This is close to one, and still would be even if the bandwidth was increased by an order of magnitude. Thus one may conclude that phase shift spread is not likely to be a problem with a pink beam illumination.

The location of the Fourier plane will vary with energy. If $\Delta g_{ch}$ is the Fourier plane misalignment of the lowest and highest contributing frequency in the spectrum, and if it is assumed that $\Delta g_{ch}$ is significantly larger than the alignment accuracy,

$$\sigma_{bg}^2 = \sigma_s^2 m_s^2 + \Delta g_{ch}^2 \sigma_{N.A.}^2 + \frac{1}{4k^2\sigma_{N.A.}^2} . \qquad (22)$$

## 4. Results and discussion

For each recorded image, a flat field image and a dark frame was also recorded. The final results presented are the flat field corrected images, where both the raw images and flat fields were dark frame subtracted. The images in Figure 4-8 were recorded with the monochromatic setup, while the image in Figure 9 was recorded with the pink beam setup and a Zernike lenslet.
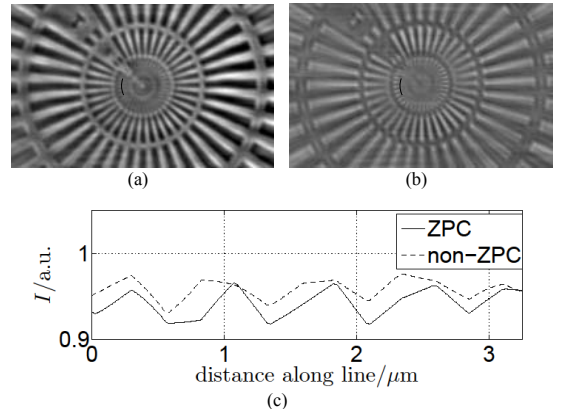


(a)                          (b)



(c)

Fig. 4 : ZPC (a) and non-ZPC (b) image of a Simens star. (c) Intensity profile sampled from the black lines using bilinear interpolation. A half period of 350 nm is resolved.

In order to compare the resolution of the ZPC and non-ZPC configuration, a ZPC and a reference image of a Simens star test object was recorded, see Figure 4. Figure 5-7 shows ZPC and reference images of 2 µm diameter polystyrene colloidal spheres, a 20 µm thick beryllium electron microscopy grid, and a boron fiber with an interior tungsten core, respectively. Exposure times of 1 s and 0.6 s for the ZPC and reference images, respectively, were chosen to stay well below the saturation limit of the CCD. Figure 8 contains images of the microstructure of an Al-Si alloy.

The sample for the pink beam image seen in Figure 9 was a 2000 mesh Cu microscopy grid with 8 μm diameter holes.
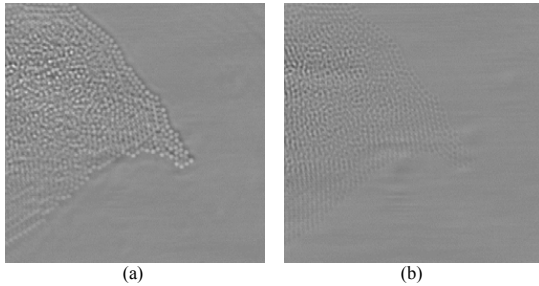

(a)                              (b)

*Fig 5: ZPC image (a) and reference image (b) of 2 μm polystyrene colloidal particles.*


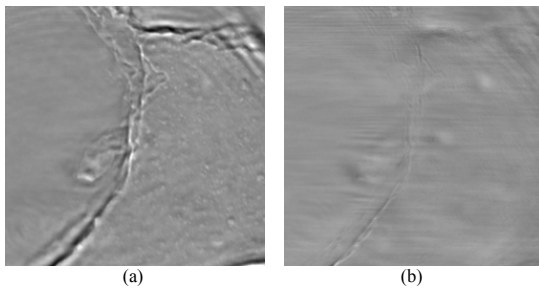(a)                              (b)

*Fig 6: Zernike phase contrast (a) and reference (b) images of a beryllium microscopy grid.*
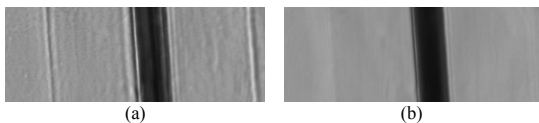

(a)                              (b)

*Fig 7 : Zernike phase contrast (a) and absorption contrast (b) images of a boron fibre with a tungsten core.*


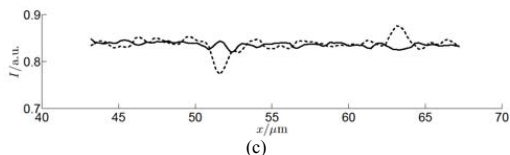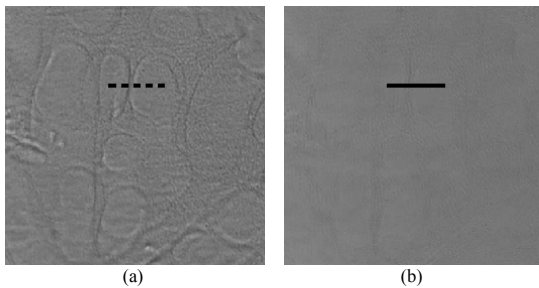(a)                              (b)


(c)

*Fig 8: Zernike phase contrast (a) and non-ZPC reference (b) images of a 200 μm thick Al-Si alloy sample.*
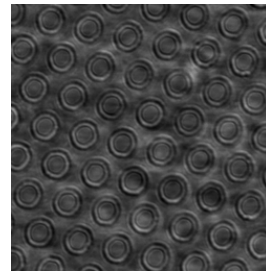


*Fig 9: Zernike phase contrast Image of a 2000 mesh Cu microscopy grid with 8 μm diameter holes, recorded with 22.5 keV radiation with 0.3% bandwidth.*

The smallest half period resolved from the images presented in Figure 4 was ~350 nm, both in the ZPC and reference image, and close to the pixel resolution of 240 nm/pixel. It should be stressed that this does not by any means represent the highest resolution obtainable with CRLs. Using the same quality lenslets, resolution should be expected to improve by a factor of 2-3 by reducing the size of the phase plate, employing a shorter focal length objective, and a higher magnification.

In Figure 4a the polystyrene spheres appear with inverted contrast with respect to the reference image Figure 4b, which is the expected result as both the platinum phase plate and the polystyrene spheres impart positive phase shifts. This is taken as clear evidence that ZPC was present. The attenuation through 2 μm polystyrene is approximately 0.01% at 17 keV, but the colloidal particles are still visible without any phase shifting element due to scattering and propagation-based phase contrast. Taking the radius of the spheres as $\rho$, $R_q\rho$=1.7. Ringing artefacts are present, but faint.

The advantage of ZPC in hard x-ray microscopy is perhaps most evident in Figure 6. Although some scattering contrast and propagation-based phase contrast appear in the reference image Figure 6b, the ZPC image reveals details that are barely visible in the reference. Likewise, in Fig 8, the boundaries between primary-phase Al-dendrites and Sr-modified fibrous Al-Si eutectic microstructures[12] are readily visible in the ZPC image. In the reference image, faint contrast features, barely detectable above the noise level, can be found between the coarse primary dendrites and the surrounding eutectic, whereas the finer internal eutectic microstructure features remain unresolved.. The absorption contrast between Al and Si at 17 keV is negligible. As the eutectic regions consists of 3D layers of micron-sized overlapping features, it is not clear whether the ZPC image represents an accurate 2D projection of the sample, which is a necessity for tomographic applications. Further experiments are necessary to determine if the setup can be used to obtain tomograms of the eutectic microstructure.

The spatial coherence of the illumination in combination with imperfections in beamline components used in the experiments typically gives a rise to speckles and features in the illumination intensity. The uneven illumination is particularly evident in Figure 5 and 6 where large horizontal fringes are visible, presumably stemming from defects in the condenser. These features can be mitigated by decohering the illumination, simply by inserting a diffuser somewhere upstream of the sample. A suitable diffuser could be a rotating disc made from a low-absorbing semi-amorphous or ultra-fine grained material. Unfortunately, decohering comes at the cost of smearing the focal spot in the Fourier plane. ZPC requires the diffuser to be gentle enough so that the background and the scattered wave still can be discriminated.

Both ZPC and standard CRL based microscopy could benefit from a practical method of controlling the spatial coherence. Uneven illumination is also visible in Figure 9. Here, however, the effects can to a large extent be attributed to problems with the flat field image. Due to hardware difficulties, the flat field image was not a proper flat field, but rather a best fit of a displaced flat field.

Halo artefacts are quite visible in Figure 7 and 9. $R_d\rho$ was 88.3 and 9.6, with $\rho$ as the radius of the boron fibre and grid holes, respectively. A number of techniques exist for apodization[13-15], but adaptation of these techniques to CRL microscopy is not necessarily straight forward without sacrificing considerable amounts of flux. Smoothing the edge of the phase plate can also have a positive effect[10] An investigation into which apodization methods might be suitable for hard x-ray CRL microscopy could be a topic for future investigations.

In Figure 9 the symmetry of the fringing around each hole suggests that the beam was well centered in the hole of the lens. No special alignment steps were necessary. The longitudinal alignment was done by simply placing the center of the objective CRL in the back focal plane of the condenser, which was estimated theoretically from (2). The fact that the symmetry of the fringes is homogenous over the FOV suggests that a theoretical estimation was sufficient for longitudinal alignment in this case. The longitudinal spread of the focal spot was approximately $\Delta g_{ch}=\pm 8.8$ mm. The intensity in the focal spot could potentially reach a level where melting of the phase elements becomes an issue. In this case, the Zernike lenslet is a good choice of phase element.

It is difficult to judge from Figure 9 alone if deviation from the ideal phase shift is a problem, however, the phase shift imparted by the phase plate in the monochromatic experiment was estimated to be $0.18\pi+3\pi/2$. This deviation yielded ZPC, and is a much larger deviation than the inherent deviation associated with pink beam illumination.

In the pink beam experiment, $\Delta g_{ch}$ was estimated to 4.6 mm. The calculation takes into account the contribution to $\Delta g_{ch}$ from the collector lenses. Assuming the central energy to be perfectly focused on the phase element, (22) result in $\sigma_{bg}=1.6$ μm, which is still not critically different from the idealized monochromatic value of $\sigma_{bg}=1.3$ μm. Had the monochromatic experiment been performed with $\Delta E/E=10^{-2}$, it would result in $\Delta g_{ch}=\pm 13.3$ mm. This gives $\sigma_{bg}=5.6$ μm, compared to $\sigma_{bg}=5.1$ μm in the monochromatic case. It is possible to reduce $\Delta g_{ch}$ somewhat by using a condenser with a shorter focal length, but source size still dominates the ZPC performance with this modest band width.

Note that (17) is somewhat strict when it comes to longitudinal misalignment. It is still possible to have ZPC even if the criterion above is not satisfied. If the spot is sufficiently small and wll aligned transversally, but with a substantial longitudinal misalignment, a projection image of the phase plate could appear in the image plane. Inside the projection image there may still be ZPC, but such considerations will not be taken any further here as they would demand lengthy discussions about the defocus and coherence related blurring of the projection image.

The illumination scheme used in these experiments is useful for avoiding lateral chromatic aberration or artefacts from spatial filtering. It also allows for insertion of the phase element into the objective. With visible light a more common technique is to employ Köhler illumination passed through an annular diaphragm. With FZPs for soft x-rays it is possible to produce what is sometimes referred to as pseudo Köhler illumination by employing a segmented zone plate[4]. The shape of the phase element may be a ring, concentric rings[13], or an array of spots[16]. The off-axis illumination associated with the use of a phase ring is expected to improve the resolution.

Unfortunately, hollow cone illumination as implemented with diaphragms or diffractive optics comes at the cost of reduced flux. With the advances made in manufacturing techniques of refractive optics, development of specialized condensers is possible. Perhaps by some adaptation of rolled prism lenses[17], or by thickness modulation of standard lenslets could serve as a refractive equivalent of sectored zone plates. Condensers could conceivably be tailored to provide illumination with the desired shapes in reciprocal space, such as rings, concentric rings, or spots. It would still be possible to place the Fourier plane inside the objective by combining with standard CRLs, so that the phase element still may be fixed to the objective. Condensers like these could conceivably be used with FZPs too.

## 5. Conclusion

In summary, ZPC using x-ray CRLs was investigated and successfully implemented at 17 keV using Be-CRLs as the only photon efficient refractive x-ray lenses. A ~350 nm half-period pattern was resolved. While the traditional hollow cone illumination scheme is more appropriate when the goal is to optimize spatial resolution, there is still room for improvement of the resolution within the scheme described here, for example by reducing the size of the phase plate, using a shorter focal length objective, and increasing the magnification. It was also demonstrated that ZPC is achievable with illumination bandwidth of $\Delta E/E=0.3\times 10^{-2}$.

## 6. ACKNOWLEDGMENT

## References

1. Zernike, F., Phase contrast, a new method for the microscopic observation of transparent objects. Physica, 1942. **9**(7): p. 686-698.
2. Schmahl, G., et al., Phase contrast X-ray microscopy studies. Optik, 1994. **97**(4): p. 181-182.
3. Neuhausler, U., et al., X-ray microscopy in Zernike phase contrast mode at 4 keV photon energy with 60 nm resolution. Journal of Physics D-Applied Physics, 2003. **36**(10a): p. A79-A82.
4. Takeuchi, A., K. Uesugi, and Y. Suzuki, Zernike phase-contrast x-ray microscope with pseudo-Kohler illumination generated by sectored (polygon) condenser plate. 9th International Conference on X-Ray Microscopy, 2009. **186**.
5. Chen, J., et al., Fresnel zone-plate based X-ray microscopy in Zernike phase contrast with sub-50 nm resolution at NSRL. 9th International Conference on X-Ray Microscopy, 2009. **186**.
6. Holzner, C., et al., Zernike phase contrast in scanning microscopy with X-rays. Nature Physics, 2010. **6**(11): p. 883-887.
7. Chen, H., et al., Quantitative phase retrieval in X-ray Zernike phase contrast microscopy. Journal of Synchrotron Radiation, 2015. **22**: p. 1056-1061.
8. Shastri, S.D., P. Kenesei, and R.M. Suter, Refractive lens based full-field x-ray imaging at 45-50 keV with sub-micron resolution. X-Ray Nanoimaging: Instruments and Methods Ii, 2015. **9592**.
9. Schroer, C.G., et al., Magnified hard x-ray microtomography: Toward tomography with sub-micron resolution. Developments in X-Ray Tomography Iii, 2002. **4503**: p. 23-33.
10. Edgcombe, C.J., Imaging by Zernike phase plates in the TEM. Ultramicroscopy, 2016. **167**: p. 57-63.

11. Kohn, V.G. and M.A. Orlov, Theoretical analysis of the possibilities of Zernike phase contrast method in hard X rays for nondestructive imaging of micropipes in a silicon carbide single crystal. Crystallography Reports, 2011. **56**(6): p. 941-946.

12. Dahle, A.K., et al., Eutectic nucleation and growth in hypoeutectic Al-SI alloys at different strontium levels. Metallurgical and Materials Transactions a-Physical Metallurgy and Materials Science, 2001. **32**(4): p. 949-960.

13. Vartiainen, I., et al., Halo suppression in full-field x-ray Zernike phase contrast microscopy. Optics Letters, 2014. **39**(6): p. 1601-1604.

14. Otaki, T., Halo reduction technique in phase contrast microscopy. Optical Review, 2001. **8**(4): p. 284-286.

15. Cheng, G.X., et al., Zernike apodized photon sieves for high-resolution phase-contrast x-ray microscopy. Optics Letters, 2010. **35**(21): p. 3610-3612.

16. Stampanoni, M., et al., Hard X-ray Phase-Contrast Tomographic Nanoimaging. 10th International Conference on X-Ray Microscopy, 2011. **1365**: p. 239-242.

17. Vogt, H., et al., X-Ray Refractive Large Aperture Rolled Prism Lenses as Condensers for X-Ray Tubes. Optical Design and Engineering Iv, 2011. **8167**.

# Paper 3

## In situ hard X-ray transmission microscopy for material science

Falch, Casari, Di Michiel, Detlefs, Snigireva, Snigireva, Honkimäki, and Mathiesen

Is not included due to copyright

# Paper 4

## Analytical Transmission Cross-coefficients for Pink Beam X-ray Microscopy Based on Compound Refractive Lenses

Falch, Detlefs, Snigirev, and Mathiesen

# Analytical Transmission Cross-coefficients for Pink Beam X-ray Microscopy Based on Compound Refractive Lenses

KEN VIDAR FALCH,[A] CARSTEN DETLEFS,[B] ANATOLY SNIGIREV,[C] AND RAGNVALD H. MATHIESEN[A,*]

[a]*Norwegian University of Science and Technology, Department of physics, Høgskoleringen 1, 7491 Trondheim, Norway*
[b]*European Synchrotron Radiation Facility, 71 Avenue des Martyrs, 38000 Grenoble, France*
[c]*Immanuel Kant Baltic Federal University, 238300 Kaliningrad, Russia*

ARTICLE INFO

ABSTRACT

Analytical expressions for the transmission cross-coefficients for x-ray microscopes based on compound refractive lenses are derived based on Gaussian approximations of the source shape and energy spectrum. The effects of partial coherence, defocus, beam convergence, as well as lateral and longitudinal chromatic aberrations are accounted for and discussed. Taking the incoherent limit of the transmission cross-coefficients, a compact analytical expression for the modulation transfer function of the system is obtained, and the resulting point, line and edge spread functions are presented. Finally, analytical expressions for optimal numerical aperture, coherence ratio, and bandwidth are given.

## 1. Introduction

Full field synchrotron X-ray microscopy experiments are typically carried out with monochromatic radiation produced by filtering the incident polychromatic beam from the source through a double-crystal monochromator, most commonly using the Si(111) reflection. This practically eliminates chromatic aberrations of refractive or diffractive optics which in turn improves the spatial resolution of the microscope, but at the cost of photon flux. The loss can be critical in experiments which require high frame rates, e.g. fast in situ X-ray imaging experiments in 2 or 3D. It is therefore of general interest to examine in detail to which extent monochromatisation can be relaxed before chromatic effects become detrimental. In the present study the transmission cross-coefficients are examined to derive compact analytical expressions for the performance of a full-field transmission microscope based on compound refractive lenses (CRLs) as function of the bandwidth of the illuminating x-rays.

The typical source for high performance X-ray microscopy at a 3rd generation synchrotron is an undulator. The undulator produces radiation with a comb-like spectrum of odd harmonic peaks. A completely non-monochromatised beam is referred to as a white beam, whereas an isolated harmonic peak commonly is referred to as a pink beam. The typical bandwidth of a harmonic peak is $\Delta E/E \sim 10^{-2}$, roughly 2 orders of magnitude larger than the typical bandwidth of a Si(111) double crystal monochromator. Both pink and white beams are used for fast lensless projection imaging [2-4], and more recently, the possibility of using compound refractive lenses (CRLs) with pink beams for focusing nanoprobes and microscopy have been demonstrated [1, 5-7].

Currently there is no simple and accurate estimate available for the modulation transfer function (MTF) of CRL-based transmission microscopes. Consequently, simple estimates for essential image forming characteristics such as point spread function (PSF), line spread function (LSF), or edge spread function (ESF) are missing. When partial coherence is to be taken into account, the straight forward integration over source points can be quite time consuming for optimization purposes, where simulations may have to be repeated when parameters are shifted. A first approximation of adding root mean square (r.m.s.) values in quadrature is sometimes used to estimate spot sizes [6-8], but this approach has a limited range of validity and can be misleading when it comes to optimization. The Hopkins method [9], sometimes also referred to as the transmission cross coefficient (TCC) method, is an effective method for simulating imaging with partial coherence. So far, direct analytical application of the Hopkins method to CRLs has not been reported.

## 2. Theory

Hopkins' equation is as follows [9]:

$$I(x) = \int TCC(q',q'')\tilde{F}(q')\tilde{F}(q'')^{*}\exp\left(-i(q'-q'')x\right)\mathrm{d}q'\,\mathrm{d}q''. \quad (1)$$

Here, $I(x)$ is the image intensity, $\tilde{F}$ the Fourier transform of the complex sample transmission function, and $TCC(q',q'')$ the transmission cross-coefficients. Substituting $\overline{q} = (q'+q'')/2$, and $\Delta q = q'-q''$ allows recasting (1) into a Fourier transform with respect to $\Delta q$,

$$I(x) = \int TCC(\overline{q},\Delta q)\tilde{F}(\overline{q}+\tfrac{1}{2}\Delta q)\tilde{F}(\overline{q}-\tfrac{1}{2}\Delta q)^{*}\exp\left(-i\Delta qx\right)\mathrm{d}\overline{q}\mathrm{d}\Delta q, \quad (2)$$

which is convenient for numerical evaluation. In the monochromatic case, the transmission cross-coefficients are given by

$$TCC_{\text{mono}}(\overline{q}, \Delta q) = \int J(q) P(\overline{q} + \tfrac{1}{2}\Delta q + q) P(\overline{q} - \tfrac{1}{2}\Delta q + q)^* \mathrm{d}q, \qquad (3)$$

where $P$ is the pupil function, and $J$ the angular source distribution. The integral in (3) must be calculated for all values of $\overline{q}$ and $\Delta q$. Fortunately, the pupil function of an x-ray CRL has the mathematically convenient Gaussian shape, even for CRLs of arbitrary length [10, 11]. Therefore,

$$P(q) = \exp\left(-\frac{q^2}{8k^2\sigma_{\text{N.A.}}^2}\right),$$

where $\sigma_{\text{N.A.}}$ is the root mean square (r.m.s.) of the transmission function of the aperture, and $k = 2\pi / \lambda$, with $\lambda$ as the photon wavelength. It is assumed that the pupil function is fully determined by the absorption in the CRL material, and that therefore the physical aperture is much larger than $\sigma_{\text{N.A.}}$. For typical microscopy applications, this is a good approximation [10, 12].

Furthermore the angular source distribution, as seen by the sample through any condensing optics and decoherers, is also approximated by a Gaussian,

$$J(q) = \frac{1}{\sqrt{2\pi k^2 S^2 \sigma_{\text{N.A.}}^2}} \exp\left(-\frac{q^2}{2k^2 S^2 \sigma_{\text{N.A.}}^2}\right), \qquad (4)$$

where $S$ is the ratio between the r.m.s of the angular source distribution and $\sigma_{\text{N.A.}}$. Under these assumptions, (3) can be integrated analytically, yielding

$$TCC_{\text{mono}}(\overline{q}, \Delta q) = \frac{1}{\sqrt{1+S^2}} \exp\left(-\frac{\overline{q}^2}{2k^2\sigma_{\text{N.A.}}^2\left(1+S^2\right)} - \frac{\Delta q^2}{8k^2\sigma_{\text{N.A.}}^2}\right) \qquad (5)$$

i.e. the TCC becomes the product of two Gaussians depending on $\overline{q}$ and $\Delta q$ only.

In the above equations it has been assumed that the filtering action of the pupil function is homogenous over the field of view. This is approximately the case if the FOV is small compared to the aperture of the objective, which may not necessarily be the case for CRL microscopy. Inhomogeneous filtering gives rise to directionally dependent fringing at edges in the sample [13], but can be eliminated by focusing the illumination in the appropriate spot, $g_{\text{ideal}}$, downstream of the object plane. It is possible, however, to include an inhomogeneous filtering effect in the TCC formalism. If $g_{\text{ideal}}$ is known, any deviation between the ideal and the actual focus, $g$, can be simulated imposing a quadratic phase shift on the sample transmission function, $F$, replacing it with

$$F_{\text{foc}} = F \cdot \exp\left(\frac{ik}{2}\left[\frac{1}{g_{\text{ideal}}} - \frac{1}{g}\right]x^2\right), \qquad (6)$$

where $x$ is the real space coordinate. In the case of a thin lens, $g_{\text{ideal}}$ will be the distance from the sample to the objective lens position. For thick CRLs, the correct convergence of the beam can readily be calculated by means of ray tracing matrices [8, 10].

To include chromatic effects, it is necessary to integrate the intensity distribution given by (2) over the energy spectrum. The image formed by out-of-focus energies will be defocused and scaled versions of the monochromatic in-focus image. Instead of considering the bandwidth directly, it is convenient to consider the spread of defocus distances. Let

$d(\alpha)$ represent the defocus distance at energy E, with $\alpha = E/E_0$ where $E_0$ is the in-focus energy. If the bandwidth of the pink beam is modest, $d(\alpha)$ may be linearized in terms of $\alpha$ as

$$d \approx \left.\frac{\partial d}{\partial \alpha}\right|_{\alpha=1} \alpha \qquad (7)$$

The power spectrum is assumed to be reasonably well represented by a Gaussian function of $\alpha$, with an associated r.m.s. $\sigma_{\Delta E/E}$. Linearization of $d(\alpha)$ implies that the defocus distribution also attains a Gaussian form,

$$W(d) = \exp\left(-\frac{d^2}{2\sigma_d^2}\right), \qquad (8)$$

with r.m.s. given by

$$\sigma_d = \left.\frac{\partial d}{\partial \alpha}\right|_{\alpha=1} \sigma_{\Delta E/E_0} . \qquad (9)$$

In order to capture the effect of increased flux with increasing bandwidth, (8) have intentionally not been normalized. The full integral expression for the chromatic transfer cross coefficients is

$$TCC_{\text{ch}}(\overline{q}, \Delta q) = \iint W(d - d_0) J(q) P(\overline{q} + \tfrac{1}{2}\Delta q + q) P(\overline{q} - \tfrac{1}{2}\Delta q + q)^*$$
$$\times \exp\left(-\frac{id}{2k}\left[(\overline{q} + \tfrac{1}{2}\Delta q + q)^2 - (\overline{q} - \tfrac{1}{2}\Delta q + q)^2\right]\right)\mathrm{d}q\mathrm{d}d \qquad (10)$$

Carrying out the integration over both $d$ and $q$ yields

$$TCC_{\text{ch}}(\overline{q}, \Delta q) = \frac{\sqrt{2\pi\sigma_d^2}}{\sqrt{1+S^2 + \sigma_{\text{N.A.}}^2\sigma_d^2 S^2 \Delta q^2}}$$
$$\times \exp\left(\frac{\sum_{m,n}\overline{q}^m \Delta q^n K_{m,n}}{4k^2\left(1+S^2 + \sigma_{\text{N.A.}}^2\sigma_d^2 S^2 \Delta q^2\right)}\right). \qquad (11)$$

The values of $K_{m,n}$ are given in Table 1. Note that only longitudinal chromatic aberration has been accounted for so far.

Lateral chromatic aberrations are related to the energy dependence of the image magnification. Similar to the case of inhomogeneous filtering, the lateral chromatic aberration can be eliminated, to the first order in $d$ at least, by focusing the illumination in the appropriate distance $g_{\text{ch}}$ from the sample [1]. The effect can be taken into account in the same way as the inhomogeneous filtering, i.e. by applying a quadratic phase shift to the sample transmission function,

$$F_{\text{foc}} = F \cdot \exp\left(\frac{ik}{2}\left[\frac{1}{g_{\text{ch}}} - \frac{1}{g}\right]x^2\right) \qquad (12)$$

Fortunately, $g_{\text{ch}}$ will be equal to $g_{\text{ideal}}$ as long as all CLR between the sample and detector planes are of one material. In most experiments involving CRLs so far, only one type of lens material is used at a time. When this is not the case it will not be possible to represent scaling and spatial filtering by (6) and (12) simultaneously, however, using $g_{\text{ch}} = g_{\text{ideal}}$ may still yield good approximations.

*Table 1: Expressions for $K_{m,n}$.*

| Coefficient | Monochromatic term | Chromatic term | Defocus term |
|---|---|---|---|
| $K_{0,2} =$ | $-(1+S^2)/2\sigma_{N.A.}^2$ | | $-2k^2\sigma_{N.A.}^2 S^2 d_0^2$ |
| $K_{0,4} =$ | | $-S^2\sigma_d^2/2$ | |
| $K_{1,1} =$ | | | $-i4kd_0$ |
| $K_{2,0} =$ | $-2/\sigma_{N.A.}^2$ | | |
| $K_{2,2} =$ | | $-2\sigma_d^2$ | |

Once the expression for TCC is known, the evaluation of (2) can be performed numerically using a diagonal sum method [14]. With $\tilde{F}(q')\tilde{F}(q'')^*$ represented on a square 2D grid, and the TCCs evaluated in the grid points, integration over $\bar{q}$ can be performed by taking the diagonal sum. The remaining integral over $\Delta q$ takes the form of a Fourier transform, and can be evaluated by the fast Fourier transform algorithm. An alternative method is the so-called sum over coherent systems method (SOCS)[15]. As SOCS involves singular value decomposition of the TCCs, it is not suitable for frequent re-evaluation of (2) with different parameters.

The modulation transfer function (MTF) can be calculated by going to the incoherent limit of (11), i.e. taking $S$ to infinity. The MTF is of interest due to its simplicity and independence of $\bar{q}$. Assuming $d_0 = 0$, a relatively simple expression for the MTF can be derived, and the result is

$$\text{MTF}(\Delta q) = \frac{1}{\sqrt{1+\sigma_{N.A.}^2 \sigma_d^2 \Delta q^2}} \exp\left(-\frac{\Delta q^2}{8k^2\sigma_{N.A.}^2}\right), \quad (13)$$

when normalizing so that MTF(0)=1. The result is generalizable to two dimensions simply by replacing $\Delta q$ with the magnitude of the two dimensional momentum exchange vector, $\boldsymbol{\Delta q}$. The incoherent LSF and PSF can be obtained from the MTF via numerical Fourier transformation.

*Optimization*

As the sample to a large extent will determine the choice of photon energy, optimization with respect to this parameter is of little general relevance, and will not be carried out here. For optimization purposes, a generic sample is chosen, represented by a small sinusoidal thickness modulation of a uniform slab. The transmission function of the sample is

$$F(x) = 1 + \varepsilon\cos(qx). \quad (14)$$

Here $q$ is the spatial frequency and $\varepsilon$ the complex amplitude of the modulation. Using (14) in (2) yields an expression on the form

$$I(x) = A_0 + \text{Re}(\varepsilon)A_1\cos(qx) + |\varepsilon|^2 A_2\cos(2qx) \quad (15)$$

Assuming $\varepsilon$ to be small, the $\varepsilon^2$-term can be ignored. The figure of merit to optimize is

$$\text{FOM} = \varepsilon\frac{A_1}{\sqrt{A_0}}, \quad (16)$$

and is proportional to the contrast to noise ratio (CNR). It is assumed that the noise is dominated by shot noise, and can be adequately modeled as Gaussian. The transmission function and FOM used here are chosen mainly due to the resulting mathematical simplicity, and do not necessarily represent the image quality as judged by a human observer [16]. Despite being a simple model for image quality, it captures the dependence on spatial frequency of the sample. The system also resembles one potential application of the hard x-ray pink beam microscope, namely the study of

self-assembling periodic lamellar patterns in solidifying metal alloy microstructures [17]. Up to a certain point, increasing the bandwidth increases both contrast and noise, but beyond this point the noise contribution becomes dominant. In other words, there is an optimal bandwidth with respect to the CNR. The right hand side of (16) can be maximized analytically with respect to $\sigma_d$ for a given $q$ yielding

$$\sigma_{d,\text{opt}}^2 = \frac{-q^2 + \sqrt{q^4 + 16k^4\sigma_{N.A.}^4 S^4\left(S^2+1\right)^2}}{4\sigma_{N.A.}^4 S^4 k^2 q^2}. \quad (17)$$

In the incoherent limit, $\sigma_{d,\,opt}$ reduces to

$$\lim_{S\to\infty}\sigma_{d,\text{opt}} = \frac{1}{q\sigma_{N.A.}},$$

while in n the coherent limit,

$$\lim_{S\to 0}\sigma_{d,\text{opt}} = \sqrt{2}\frac{k}{q^2} \approx 0.11\cdot Z_T,$$

where $Z_T = 4\pi k/q^2$ is the Talbot length related to $q$. It should be stressed that the positive contribution of increasing $\sigma_d$ stems entirely from enhanced photon flux. Increasing $\sigma_d$ by enlarging $\partial d/\partial\alpha$ has no positive effect. A smaller $\partial d/\partial\alpha$ improves the CNR, regardless of bandwidth. Similarly, when considering optimization of CNR with respect to $S$, attention must be given to whether the total flux increases, or not. If the effective source size is determined by occlusion, increasing the source size will increase the photon flux linearly with $S$. In that case, the FOM should be multiplied by $S^{1/2}$ to account for it. Optimization with respect to $S$ yields

$$S_{\text{opt}}^2 = \frac{q^2 + q^6\sigma_d^4\sigma_{N.A.}^4 + 2q^4\sigma_d^2\sigma_{N.A.}^2 + 4k^2\sigma_{N.A.}^2}{4k^2q^4\sigma_d^4\sigma_{N.A.}^6 - 2q^6\sigma_d^6\sigma_{N.A.}^4 - 4q^4\sigma_d^2\sigma_{N.A.}^2 - 4k^2\sigma_{N.A.}^2 - 2q^2} \\ + \frac{q^2\sqrt{q^4k^8\left(1+\left(q^8\sigma_d^8 + 16k^4\sigma_d^4\right)\sigma_{N.A.}^8 + 4q^6\sigma_{N.A.}^6\sigma_d^6 + 6q^4\sigma_{N.A.}^4\sigma_d^4 + 4q^2\sigma_{N.A.}^2\sigma_d^2\right)}}{4k^2q^4\sigma_d^4\sigma_{N.A.}^6 - 2q^6\sigma_d^6\sigma_{N.A.}^4 - 4q^4\sigma_d^2\sigma_{N.A.}^2 - 4k^2\sigma_{N.A.}^2 - 2q^2} \quad (18)$$

In the case where the illumination intensity remains constant while the angular source changes, the optimal $S$ is

$$S_{\text{opt}}^2 = \frac{q^2 - 4k^2\sigma_d^2\sigma_{N.A.}^4 + q^4\sigma_d^2\sigma_{N.A.}^2 - 4k^2\sigma_{N.A.}^2}{4k^2\sigma_{N.A.}^2\left(1+\sigma_{N.A.}^2\sigma_d^2 q^2\right)} \\ + \frac{q^2\sqrt{1+\left(16k^4\sigma_{N.A.}^8 + q^4\sigma_{N.A.}^4\right)\sigma_d^4 + 2q^2\sigma_d^2\sigma_{N.A.}^2}}{4k^2\sigma_{N.A.}^2\left(1+\sigma_{N.A.}^2\sigma_d^2 q^2\right)} \quad (19)$$

The expression for the optimal numerical aperture is impractically large, and has been included as supplementary material. Fortunately, optimization of the MTF yields

$$\sigma_{N.A.,\text{ opt}}^2 = \frac{q^2}{8k^2} + \frac{\sqrt{q^4\sigma_d^2 + 16k^2}}{8\sigma_d k^2}, \quad (20)$$

which is a much more compact and agreeable expression.

## 3. Results and discussion

Figure 1 shows the LSF and PSF calculated for the pink beam case by using (13), together with the monochromatic case were the PSF and LSF are identical. Evidently and perhaps not surprisingly, the chromatic spread functions have tails, and those of the LSF are more severe than for the PSF. In the monochromatic case, adding a third line (equally spaced) makes little contribution to the contrast between the first two, provided that they are
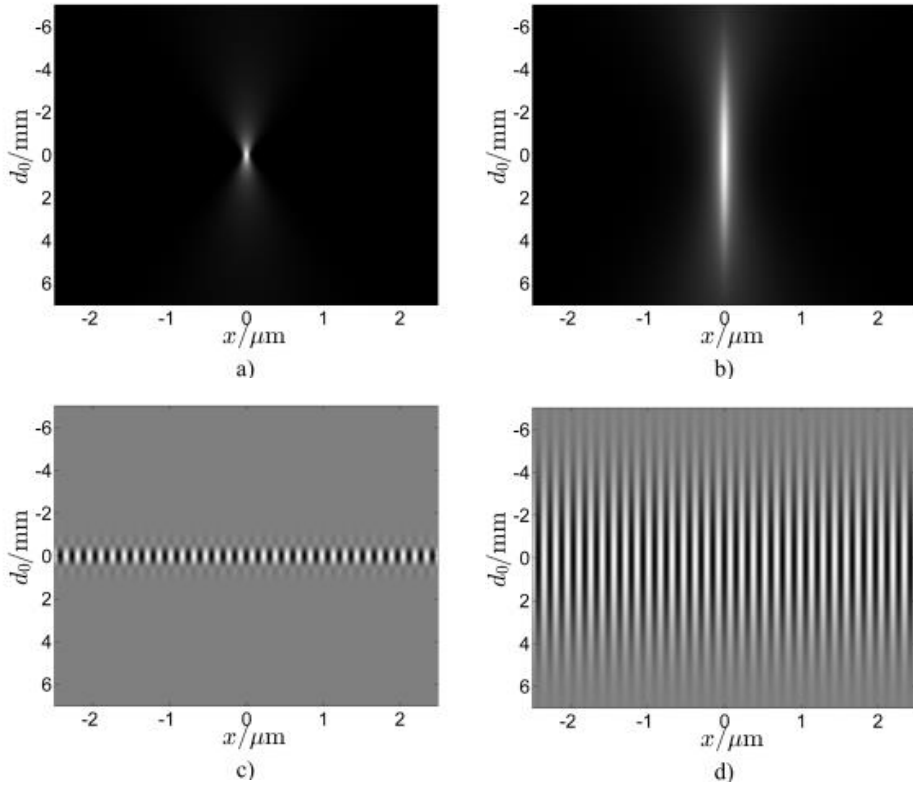
*Figure 2: Simulated 1D images at different defocus $d_0$. (a) and (b) are monochromatic and pink beam images, respectively, of a Gaussian with 10 nm r.m.s. value, which is small compared to the diffraction limit of 75 nm. (c) and (d) are monochromatic and pink beam images, respectively, of a grating with period of 150 nm. A coherence ratio of S=0.5 was used in the simulations. The other parameters used were $E_0=35keV$, and $\sigma_{N.A.} = 1.05 \cdot 10^{-4}$. In the pink beam case, $\sigma_d=2.55$ mm was used, while $\sigma_d=0$ was used in the monochromatic case.*

separated by a distance comparable to the diffraction limit. In the pink beam case, however, the presence of additional lines can make significant contributions to contrast between the other two. The sinusoidal sample model used here assumes an infinite periodic sample and will therefore take into consideration the long tail of the LSF.
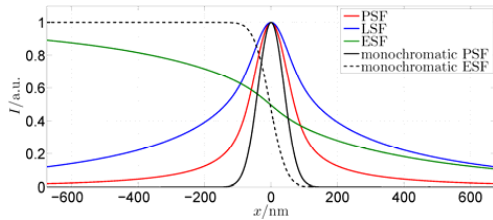


*Figure 1: The LSF and PSFs for the pink beam and monochromatic beam cases. The LSF is determined by an inverse Fourier transform of the 1D MTF, and a slice of the PSF has been extracted by applying the Fourier slice theorem to the 2D MTF. The ESFs were calculated by convoluting the LSF with a step function. The parameters used in the calculation were $\sigma_d=5.4$ mm and $\sigma_{N.A.}=1.5 \cdot 10^{-4}$.*

Figure 2 compares 1D images of two Gaussian shaped objects at different defocus lengths. Depth of field (DOF) with monochromatic illumination is mostly a matter of numerical aperture. It is evident that with pink-beam illumination, $\sigma_d$ can come into play in a significant manner as well. A coherence ratio of 0.5 was used to create the images in Figure 2. It should be noted that in (c) and (d), such an increase in DOF is not achieved when a highly coherent beam is used, due to emergence of interference patterns.
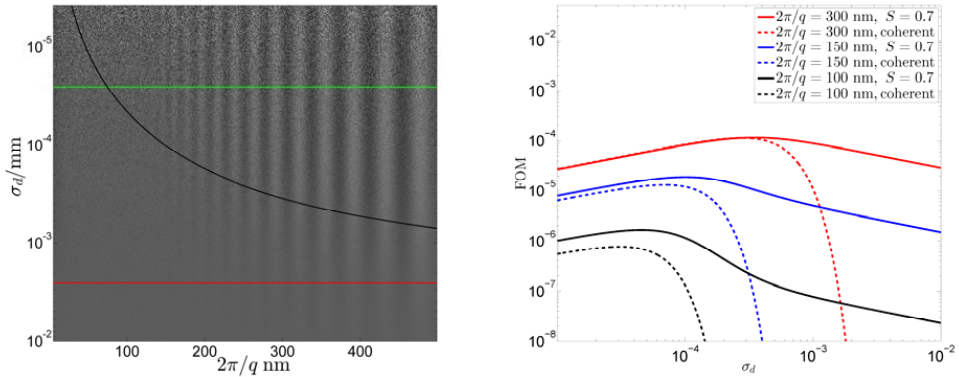
*Figure 3: a) Simulated 1D images with noise, computed for different bandwidths. The black line indicates the optimal bandwidth as given by (17). The green and red curves indicate Si-111 monochromatic and pink beam case, respectively, with rate of defocus at $\frac{\partial \zeta}{\partial \sigma} = 0.6$. The monochromatic bandwidth was set to $10^{-4}$ (FWHM), and the pink beam bandwidth was set to $10^{-2}$ (FWHM). The figure appearances depend on several parameters choices, where the most decisive ones are $E_0 = 17keV$, $S = 0.5$, and $\sigma_{N.A.} = 1.75$, corresponding to a diffraction limit of 93nm.*
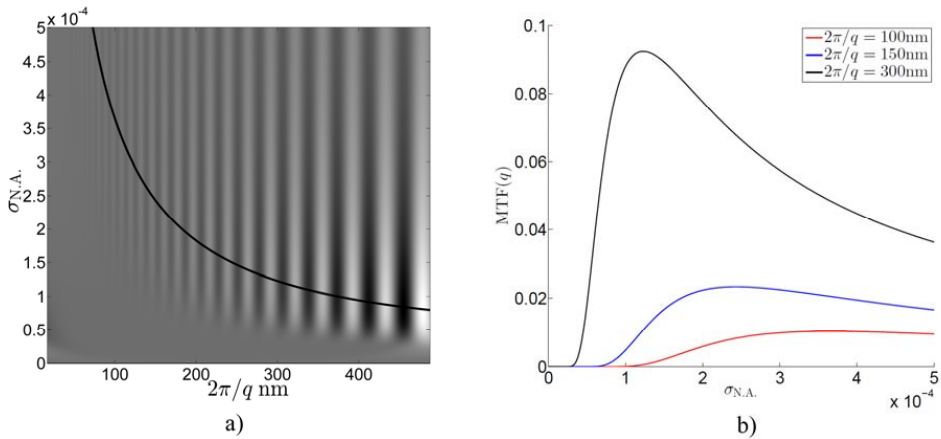


*Figure 4: (a) Simulated 1D images of a sinusoidal wave with gradually changing period. The simulation is based on the MTF. Each horizontal line is an individual image, simulated with different N.A.. The horizontal axis is labeled with the length of the period. The black line indicates the N.A. that optimizes MTF(q), according to (20). Parameters used were $E = 17$ keV, $\sigma_d = 2.5$ mm. (b) MTF as a function of $\sigma_{N.A.}$ at different values of q.*

Figure 3 illustrates the effect of varying $\sigma_d$. Artificial noise was added to Figure 3 a) to capture the detrimental effect of low flux. Although optimizing FOM does not necessarily optimize the image quality as judged by a human observer, it seems to come rather close in this case. Increasing the bandwidth beyond the optimal is of course detrimental to the resolution, but it should be noted that the DOF at the optimal bandwidth is comparable to the monochromatic DOF. Significant gain only occurs when $\sigma_d$ is increased beyond the optimal. Figure 3 b) shows the FOM for three different values of $q$, with $S = 0.7$, and with perfect coherence. Both the perfectly coherent and partially coherent curves starts off with an incline proportional to $\sigma_d^{1/2}$, which suggests that the exposure time required to reach a given CNR is proportional to $\sigma_d$, as should be expected. In the coherent case there is a rather sharp cutoff near the optimum, where FOM declines rapidly, while with a partial coherence, the descent is much slower.

Figure 4 shows simulated 1D image with varying N.A.. It is evident that there is quite a bit of contrast to be gained by maximizing the aperture to a specific spatial frequency. It is of course difficult to determine which spatial frequency to optimize for in most cases. However, for application to microscopy of lamellar structures, the approximate lamellar spacing may be known in advance.
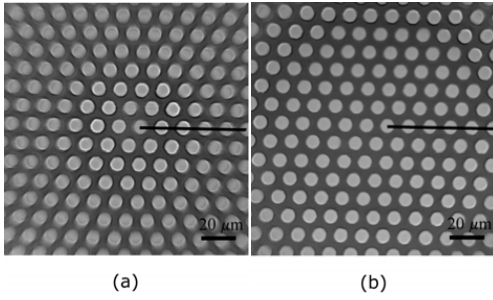
*Figure 5: Experimental images of a copper mesh from a previously published experiment [1]. (a) and (b) were recorded with parallel illumination and with converging illumination, respectively. The convergence was due to a condenser lens configured to focus the source inside the objective.*

The theory and optimization presented here is concerned with perfect lenses. Real CRLs, of course, have aberrations that will influence the image quality. Figure 5 shows two images taken from a previously published experiment [1], recorded with an objective and condenser consisting of 84 and 32 double concave 50 μm apex radius Be lenslets, respectively. The condenser was positioned to focus the illumination into the center of the objective, and a beam decoherer was placed approximately 10 cm downstream of the condenser. The sample was a 4 μm thick Copper mesh. Figure 6 compares simulations based on the presented theory to the experimental results sampled from the black lines in Figure 5. The defocus in the simulations was set to $d_0 = 4.6$ based on an estimate that considered the apparent difference in magnification of the experimental curves [1].
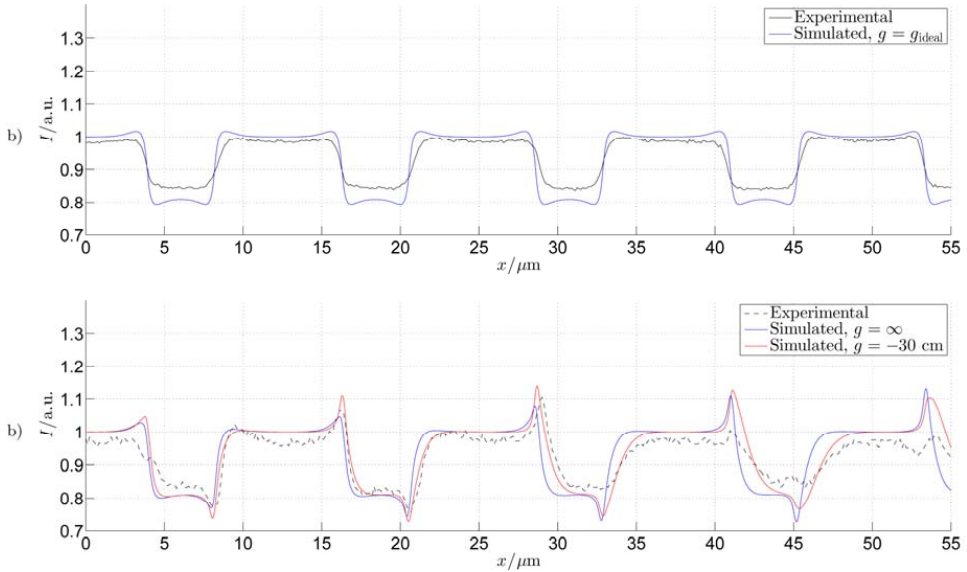
There is a notable mismatch between the simulation and the experimental data, the most significant of which is the exaggerated contrast in the simulation presented in a). In b) there is a reasonable agreement that gets progressively worse towards the periphery of the FOV, i.e. as $x$ increases. It is notable, however, that in the region between 15-30 μm, the agreement is quite good, especially considering that the simulation parameters were simply taken from estimates, without parameter fitting. The fit is somewhat better when using $g=-30$ cm, which corresponds to regarding the decoherer as the effective source plane.

While it is tempting to attribute the improvement to the decoherer, it cannot be ruled out that spherical aberrations might be the real cause. Spherical aberration in the type of lenses that were used in the experiment, namely 50 μm apex radius Be lenses, have been reported [6, 18]. If spherical aberration was present, it would, in the parallel beam case, produce a defocused image by an amount that differs over the FOV. Figure 7 shows the same simulations as in Figure 6, repeated with $d_0 = -4$ mm. The $x = 15-30$ μm region is no longer a good fit, however the $x=0-10$ μm region is now in much better agreement than in Figure 6. Furthermore, the contrast level in the focused beam simulation is close to that of the experiment, albeit with some new fringe features. It should be mentioned that the appearance of fringes is rather sensitive to the choice of $S$. The contrast level largely depends on the transmission of rays representing low spatial frequencies, which in the focused beam case travel mostly through the center the lens where spherical aberration is least prominent. This might suggest that the defocus that gives a good fit in the center of the FOV would also give a better estimate of the contrast. Thus spherical aberrations seem to be an important source of discrepancy between the simulations and experiments.

**4. Conclusion**



*Figure 6: Comparison with experimental results [1]. x=0 is in the center of the FOV. a) Beam focused into objective. b) Parallel beam illumination. Note that g is the only parameter that was changed in the simulations. All other parameters were the same for all three simulations. $d_0$ was set to 4.6 mm, as estimated in [1, 2]. Other parameters used were $\sigma_d = 3.6$ mm, $\sigma_{N.A.} = 1.75 \cdot 10^{-4}$, E = 17 keV, S = 0.7, and $g_{ideal} = 30$ cm. The curves were flat field corrected with a simulated featureless sample, to compensate for vignetting of the FOV.*
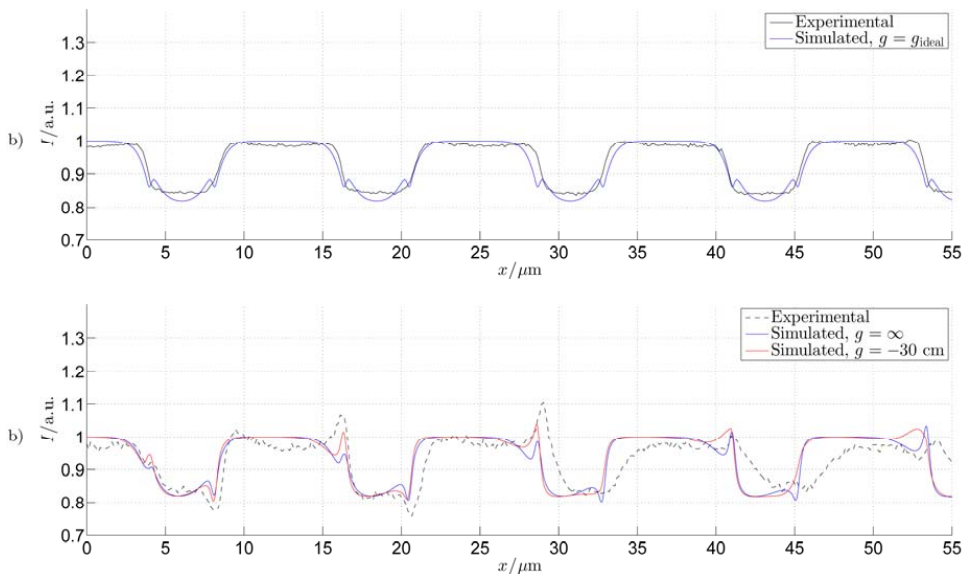
*Figure 7: Comparison with experimental results [1]. x= 0 is in the center of the FOV. a) Beam focused into objective. b) Parallel beam illumination. $d_0$ was set to -4 mm, which yields an improved fit near x = 0 and a closer agreement with the experimental contrast levels. All other parameters were the same for all three simulations, and were identical to those used in Figure 6.*

The transmission cross-coefficients for an x-ray microscope based on compound refractive lenses were derived using Gaussian approximations of the source shape and energy spectrum. The effects of partial coherence, defocus, beam convergence, as well as lateral and longitudinal chromatic aberration are included in the solution. An analytical expression for the MTF was obtained, as well as for optimal numerical aperture, coherence ratio, and bandwidth. Comparison with experimental data shows qualitative agreement, however, it is likely that a more detailed model of illumination or lens aberrations, or both have to be taken into account in order to produce better simulations.

# References

1. Falch, K.V., et al., *Correcting lateral chromatic aberrations in non-monochromatic X-ray microscopy.* Applied Physics Letters, 2016. **109**(5): p. 054103.
2. Ludwig, O., et al., *In-situ three-dimensional microstructural investigation of solidification of an Al-Cu alloy by ultrafast x-ray microtomography.* Metallurgical and Materials Transactions A, 2005. **36**(6): p. 1515-1523.
3. You, J.X., et al., *Interfacial undercooling in solidification of colloidal suspensions: analyses with quantitative measurements.* Scientific Reports, 2016. **6**: p. 28434.
4. Rack, A., et al., *Exploiting coherence for real-time studies by single-bunch imaging.* Journal of Synchrotron Radiation, 2014. **21**: p. 815-818.
5. Falch, K.V., et al., *In situ hard X-ray transmission microscopy for material science.* Journal of Materials Science(accepted, unpublished), 2016.
6. Seiboth, F., et al., *Focusing XFEL SASE pulses by rotationally parabolic refractive x-ray lenses.* 22nd International Congress on X-Ray Optics and Microanalysis, 2014. **499**.
7. Dufresne, E.M., et al., *Pink-beam focusing with a one-dimensional compound refractive lens.* Journal of Synchrotron Radiation, 2016. **23**: p. 1082-1086.
8. Falch, K.V., et al., *Zernike phase contrast in high-energy x-ray transmission microscopy based on refractive optics.* Ultramicroscopy, 2016. **Under Review**.
9. Hopkins, H.H., *On the Diffraction Theory of Optical Images.* Proceedings of the Royal Society of London Series a-Mathematical and Physical Sciences, 1953. **217**(1130): p. 408-432.
10. Simons, H., et al., *Full-field hard x-ray microscopy with interdigitated silicon lenses.* Optics Communications, 2016. **359**: p. 460-464.
11. Kohn, V.G., *Semianalytical Theory of Focusing Synchrotron Radiation by an Arbitrary System of Parabolic Refracting Lenses and the Problem of Nano-Focusing.* Journal of Surface Investigation-X-Ray Synchrotron and Neutron Techniques, 2009. **3**(3): p. 358-364.
12. Snigireva, I., G.B.M. Vaughan, and A. Snigirev, *High-Energy Nanoscale-Resolution X-ray Microscopy Based on Refractive Optics on a Long Beamline.* 10th International Conference on X-Ray Microscopy, 2011. **1365**: p. 188-191.
13. Schroer, C.G., et al., *Beryllium parabolic refractive x-ray lenses.* Design and Microfabrication of Novel X-Ray Optics, 2002. **4783**: p. 10-18.
14. Yamazoe, K., *Fast fine-pixel aerial image calculation in partially coherent imaging by matrix representation of modified Hopkins equation.* Applied Optics, 2010. **49**(20): p. 3909-3915.
15. Saleh, B.E.A. and M. Rabbani, *Simulation of Partially Coherent Imagery in the Space and Frequency Domains and by Modal Expansion.* Applied Optics, 1982. **21**(15): p. 2770-2777.
16. Burgess, A.E., *The Rose model, revisited.* Journal of the Optical Society of America a-Optics Image Science and Vision, 1999. **16**(3): p. 633-646.
17. Witusiewicz, V.T., et al., *The Ag-Al-Cu system - Part I: Reassessment of the constituent binaries on the basis of new experimental data.* Journal of Alloys and Compounds, 2004. **385**(1-2): p. 133-143.

18.     Koch, F.J., et al., *Quantitative characterization of X-ray lenses from two fabrication techniques with grating interferometry.* Optics Express, 2016. **24**(9): p. 9168-9177.

# Chapter 8

# Conclusions and outlook

Paper 1 demonstrates improved image quality and correction of lateral chromatic aberration by focusing the illumination into the objective lens, which also optimizes transmission from object to image plane. To determine definitively that the aberration was corrected, a monochromatic energy scan was performed, from which it could be concluded that lateral aberration was indeed corrected.

There may, however, be other factors contributing to the improved image quality. Spherical aberration in the lens shapes may, in the parallel beam case, contribute to a significant field curvature. Focusing the illumination into the objective likely has the added benefit of flattening the field. An experiment to confirm this might be worthwhile.

Methods have been developed to characterize the aberration, however, it may be possible to quickly asses spherical aberration of an entire CRL stack by measuring the field curvature. If the aberration is predominantly spherical, it might be possible to produce phase element to compensate for spherical aberration. Significant improvement to the resolution might be gained, without tailoring a phase plate to a specific CRL.

Paper 2 demonstrates ZPC in a CRL microscope, and shows that ZPC can be implemented with the scheme presented in paper 1. Estimations were presented that indicates that the use ZPC with a pink beam is possible without alterations to the scheme. The fact that the beam is focused in the objective allows ZPC to be achieved by using modified CRLs. This was demonstrated by employing a lenslet with a circular hole as a negative phase plate.

The resolution was limited due to the need for long propagation distance to allow

the scattered field to separate properly from the background field. A significant gain in resolution can be expected if a smaller diameter phase element is employed, allowing shorter focal lengths to be used. Implementation of traditional hollow cone illumination is also expected to improve resolution, but at the cost of photon flux. However, modification of refractive condenser optics could be a reasonable approach to hollow cone illumination with minimal loss of photons.

Paper 3 Demonstrates that HXTM can be operated both in monochromatic and non-monochromatic modes. It was shown that with pink beam illumination, full tomograms can be recorded in 1–2 s, with spatial resolutions below 200 nm, using 1ms frame exposure times. Potential application areas of fast 2D and 3D microscopy were demonstrated with a few selected test cases, including regular and irregular eutectic solidification microstructure formation, and self-assembly of colloidal crystal systems composed of polymer particles with diameters in the micrometer range.

Paper 4 prescribes optimal coherence lengths and numerical apertures for any bandwidth and resolution requirement. It also identifies the bandwidth that is useful for a given resolution, which helps to identify the conditions under which a pink beam is preferable to a monochromatic beam.

A natural concern regarding the scheme presented in paper 1 is that resolution is lost due to the longer coherence length. An investigation into practical methods of tuning the coherence length with minimal loss of flux could be of interest, especially for ZPC, where it is desirable to tune the illumination to the phase shifting element. Paper 4 provides tools to evaluate the trade-off between flux and coherence length.

Some convenient relations between numerical aperture and longitudinal chromatic aberration have been derived. As the optimal $\sigma_{N.A.}$ for maximizing resolution with pink beams is well above what is currently achievable, the fact that $\sigma_d$ decreases rapidly with $\sigma_{N.A.}$ suggests that efforts to optimize the resolution of a pink beam microscope is currently well aligned with efforts to optimize resolution in the monochromatic case, with the possible exception that different lens materials might be of interest due to the $\sigma_d \propto 1/\gamma$ relationship.

Finally, A light-weight numerical modelling tool, based heavily on previous work [41, 42, 75], was developed for fast evaluation of image quality.

As for further improvement of temporal resolution, there is still a lot to be gained in terms of detector DQE. While the development of X-ray detectors is a very active field of research, some measures using only available technology are possible. By simply increasing the magnification of the CRL microscope, the detector

resolution requirements can be relaxed. For example, if the detector resolution requirement is reduced by a factor of 3, the scintillator plate is allowed to be 9 times thicker, which increases the fraction of absorbed X-rays. Furthermore there is an on-going effort to reduce the pixel size of highly efficient solid state detectors. If their pixel size can reach the 20 $\mu$m range, they could become useful for microscopy if $> 100$ magnification is employed.

# Appendix A

# Minimization of chromatic aberration of CRL systems

In paper 1 [28] it was demonstrated that lateral chromatic aberration can be corrected by focusing the illumination inside the objective. The theory presented there was based on approximating the objective as a thin lens.This chapter will elaborate the theory to account for arbitrary systems of CRLs. Two simple relationships will be derived that relates lateral and longitudinal chromatic aberrations, in terms of $\sigma_{\mathrm{N.A.}}$. To the knowledge of the author, this work is original.

## A.1 Lateral chromatic aberration

Lateral chromatic aberration can be analysed with RTMs. The change in magnification of a system represented by an ABCD-matrix is

$$\frac{\partial \mathcal{M}}{\partial \alpha} = \frac{\partial A}{\partial \alpha} \tag{A.1}$$

With a thin lens microscope under parallel beam illumination,

$$\frac{\partial \mathcal{M}}{\partial \alpha} = -\frac{2p}{f} \mathcal{M}_0, \tag{A.2}$$

whereas in the case of the constant profile CRL microscope, one obtains

$$\frac{\partial \mathcal{M}}{\partial \alpha} = \left( L \sin(\omega L) + \omega L q \cos(\omega L) + q \sin(\omega L) \right) \frac{\omega_0}{\alpha^2}. \tag{A.3}$$

It is possible to change $\frac{\mathrm{d}\mathcal{M}}{\mathrm{d}\alpha}$ by pre-multiplying the RTM with a matrix corresponding to focusing the illumination a distance $g$ from the sample. Letting $M_P$

be the parallel beam illuminated system, the new RTM with focused illumination becomes

$$M_g = M_P \begin{bmatrix} 1 & 0 \\ -\frac{1}{g} & 1 \end{bmatrix} = \begin{bmatrix} A_P - \frac{B_P}{g} & B_P \\ C_P - \frac{D_P}{g} & D_P \end{bmatrix}, \tag{A.4}$$

from which one may derive the following relation:

$$\mathrm{d}\mathcal{M}_g = \mathrm{d}A_P - \frac{1}{g}\mathrm{d}B_P + \frac{B_P}{g^2}\mathrm{d}g. \tag{A.5}$$

The $\mathrm{d}g$-term accounts for the possibility that the condensing optics may not be achromatic. Assuming $B_P = 0$, the distance $g_{\mathrm{ch}}$ that eliminates lateral chromatic aberration, to the first order in $\alpha$, is

$$g_{\mathrm{ch}} = \frac{\mathrm{d}B_P}{\mathrm{d}A_P} \tag{A.6}$$

Computing $g_{\mathrm{ch}}$ analytically from (A.6), although somewhat laborious, is straight forward. It is also easily computed by numerical differentiation. However, $g_{\mathrm{ch}}$ must be equal to $g_{\mathrm{ideal}}$ as long as all lenslets in the system are made from only one type of material. This conclusion can be arrived at by considering the change in optical path length in response to a change in the refractive index of the CRL. When the microscope is in imaging condition, all rays emanating from a point $P_o$ in the object plane and terminating in a point $P_i$ in the image plane will have the same optical path length. Now suppose an infinitesimal change $\mathrm{d}n$ is added to the CRL refractive index, $n_{\mathrm{CRL}}$. Let $C_{w_o,x_o}$ be the ray defined so that it intersects the object plane at $x_o$ at an angle $w_o$. The infinitesimal change to the optical path length is

$$\Phi = \mathrm{d}\left(\int_{C_{w_o,x_o}} n(s)\mathrm{d}s\right) = \Theta\mathrm{d}n + \delta\int_{C_{w_o,x_o}} n(s)\mathrm{d}s, \tag{A.7}$$

where

$$\Theta = \int_{C_{w_o,x_o}} \rho_{\mathrm{CRL}}(s)\mathrm{d}s,$$

and $\rho_{\mathrm{CRL}}(s)$ is the CRL material density, which is zero outside the CRL and equal to $\frac{x^2}{R}$ inside it. The second term on the right hand side in (A.7) vanishes due to Fermat's principle. Note that $\Theta$ is the same integral as the one computed to evaluate the attenuation of the rays. The ray that minimizes $\Theta$ is the ray of maximum transmission. It also stands out as the ray with the minimum change in optical path length in response to a change in $n_{\mathrm{CRL}}$. Consider a point $P_o$ in the object plane
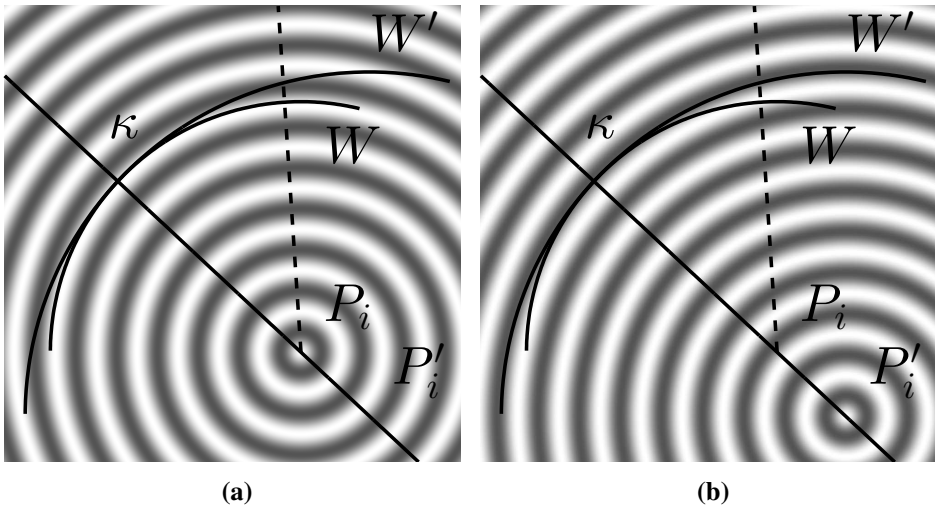
**Figure A.1:** Illustration of wave fronts in (a) the initial system, and (b) the perturbed system. The perturbation causes the image of the point source to move from $P_i$ to $P_i'$, but $W$ and $W'$ is tangential in $\kappa$. The line intersecting both $\kappa$ and $P_i$ remains tangential to the wave fronts in both systems, and is therefore a valid ray in both systems.

located a distance $x_0$ from the optical axis. Let $\kappa$ be the point on the image side of the system where the ray that minimizes $\Theta$ intersects a wave front, $W$. Furthermore, let $W'$ be the wave front that includes $\kappa$, after a small change in refractive index have occurred. The infinitesimal optical path length difference, $\Phi$, between $W$ and $W'$, along the rays of the original system, is equal to the geometrical distance. Furthermore, because $\kappa$ is defined as containing the ray that minimizes the optical path length response, $\Phi$ will have either a minimum or maximum at $\kappa$, which implies that $W$ and $W'$ will be tangential at $\kappa$, and that the angle of the ray joining $P_o$ and $\kappa$ does not change to the first order in $dn$. Thus it can be concluded that the point in which the ray intersects the detector plane will be unchanged to the first order of $dn$. As this is the criterion for correction of lateral chromatic aberration, it is evident that

$$g_{\text{ch}} = g_{\text{ideal}} \tag{A.8}$$

as long as $\gamma$ is constant throughout the CRL. This argument is valid for arbitrary systems of CRLs, as illustrated in Figure A.2.
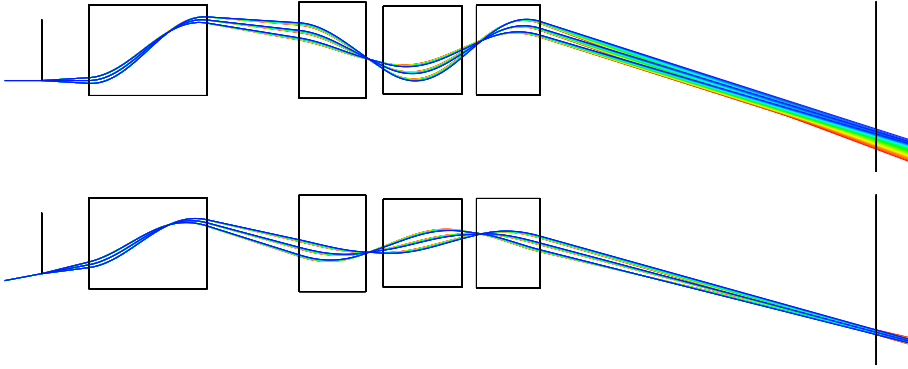
**Figure A.2:** Ray traces through randomized system of CRLs with parallel and ideally focused illumination in the top and bottom image, respectively.

## A.2   Longitudinal chromatic aberration

With small bandwidths, $d$ may be linearised as a function of $\alpha$ by differentiating (2.32).

$$\frac{\partial}{\partial \alpha} d = \frac{1}{A} \frac{\partial B}{\partial \alpha} - \frac{B}{A^2} \frac{\partial A}{\partial \alpha}. \tag{A.9}$$

For a thin lens microscope, regardless of the value of $g$ the rate of defocusing is

$$\frac{\partial}{\partial \alpha} d = -2p \left( 1 + \frac{p}{q} \right). \tag{A.10}$$

For long CRLs, the matter is more complicated. While it is possible to linearize $d(\alpha)$ by explicitly differentiating ABCD-matrix elements, another approach will be presented here that provides a simple relationship between $\frac{\partial}{\partial \alpha} d$ and $\sigma_{\text{N.A.}}$. In the same fashion as $\Sigma^{-1}$ and $\Sigma_i^{-1}$ was defined in (3.19) and (3.21), $V$ and $V_i$ will be defined here as

$$V \quad = \quad \int_0^L M_{\text{CRL}}(z')^\top O' M_{\text{CRL}}(z') \mathrm{d}z' = \frac{1}{\gamma} \Sigma^{-1}, \tag{A.11}$$

where

$$O' = \begin{bmatrix} -\frac{2k\delta}{RT} & 0 \\ 0 & 0 \end{bmatrix}, \tag{A.12}$$

and

$$V_o = R(p)^\top V R(p) = -\frac{1}{\gamma} \Sigma_o^{-1}. \tag{A.13}$$

Ignoring the web thickness, $\Theta$ in (A.7) may be expressed as

$$\Theta = -\frac{1}{2}\mathbf{x}^\top V_o \mathbf{x} \qquad (A.14)$$

It is clear from Figure A.1 that the perturbation of the wave front in response to a small change in refractive index is the same as the response to a small displacement of the image. The rate of the displacement with respect to $\alpha$ is, by the displacement theorem [12],

$$\frac{\partial}{\partial \alpha} d = -\frac{2}{k} V_{o,2,2}. \qquad (A.15)$$

If $\gamma$ is constant (throughout the CRL system), the following relationship exists between the longitudinal aberration and $\sigma_{\text{N.A.}}$ (of the system):

$$\frac{\partial}{\partial \alpha} d = -\frac{2}{k\gamma\sigma_{\text{N.A.}}^2} \qquad (A.16)$$

# Appendix B

# Simulation of pink beam microscopy based on complex RTMs

Although the propagator of a single CRL imaging system have been derived in earlier works [41, 42, 75], a more general formalism exists that applies to arbitrary first order optical systems, including systems with absorbing lenses [50, 51]. As the formalism is based on complex ray transfer matrices, it significantly simplifies notation.

Fast simulation based on this formalism is a useful tool to quickly asses field of view, lens aberration effects, and sensitivity to misalignment. It can also be used to evaluate the effects of phase elements and arbitrary shaped aperture stops. Implementation of the simulation tool may, however, offer a few technical hurdles. This section will present the basic theory, and show how to resolve the difficulties related to numerical implementation.

## B.1   Theory

A first order optical system is a system in which the small angle approximation is valid, and all optical elements are described by polynomials of second order, or lower. If the ray transfer matrix of the system is

$$M = \begin{bmatrix} A & B \\ C & D \end{bmatrix},$$

(B.1)

where $A$, $B$, $C$, and $D$ are arbitrary complex parameters that satisfies $AD - BC = 0$, the Greens function of any first order optical system can be expressed in terms of the elements of $A$, $B$, $C$, and $D$, including the cases where the lens material has a complex refractive index[51],

$$G(x', x) \quad = \quad \left( i \frac{2\pi B}{k} \right)^{\frac{1}{2}} e^{\frac{ik}{2B} \left( Dx'^2 - 2xx' + Ax^2 \right)}, \tag{B.2}$$

where $x$ and $x'$ are the input and output coordinates of the system, respectively, and $k = \frac{2\pi}{\lambda}$ is the wavenumber. The expression can be made computationally convenient by factorizing into $x'$, $(x' - x)$, and $x$ terms.

$$G(x', x) = \left( i \frac{2\pi B}{k} \right)^{\frac{1}{2}} e^{\frac{ik}{2} \left( \frac{D-1}{B} \right) x'^2} e^{\frac{ik}{2B} (x'-x)^2} e^{\frac{ik}{2} \left( \frac{A-1}{B} \right) x^2} \tag{B.3}$$

Employing this form, propagation through the first order system can be expressed as a multiplication, followed by a convolution, and another multiplication,

$$\psi' (x') = \left( i \frac{2\pi B}{k} \right)^{\frac{1}{2}} e^{\frac{ik}{2} \left( \frac{D-1}{B} \right) x'^2} \int e^{\frac{ik}{2B} (x'-x)^2} e^{\frac{ik}{2} \left( \frac{A-1}{B} \right) x^2} \psi (x) \, dx \tag{B.4}$$

## B.2    Implementation

In terms of operators, (B.4) can be written as

$$\psi' = \left( i \frac{2\pi B}{k} \right)^{\frac{1}{2}} Q \left[ \frac{D-1}{B} \right] R [B] Q \left[ \frac{A-1}{B} \right] \psi. \tag{B.5}$$

where $Q [c]$ represents a multiplication with the function $\exp(\frac{1}{2} ikcx^2)$, and $R [d]$ is a convolution with the function $\exp(\frac{ik}{2d} \Delta x^2)$, which is equivalent to a propagation if $d$ is a real number. The form of (B.5) is not one of the fundamental representations given by Nazarathy and Shamir [50]. The reason for not using the fundamental representations is that they contain scaling operators, which in the general case could contain a complex argument. Computation of a complex scaling/rotation is circumvented by using (B.5), which contains only the $Q$ and $R$ operators, both of which are easily implemented numerically using only multiplication and Fourier transforms.

There are several ways to implement the propagation operation. As the real part of $B$ will typically be small for microscopy, a reasonable choice is to use

$$R [B] = \mathcal{F}^{-1} Q \left[ -\frac{B}{k^2} \right] \mathcal{F}. \tag{B.6}$$

As an X-ray microscope will typically magnify the beam, a straight forward implementation of (B.5) could therefore imply the risk that the numerical field of view could be too small to cover the beam at the output plane. To prevent this from occurring, it is helpful to demagnify the output image multiplying the RTM with a scaling matrix, to obtain

$$M_{\text{scaled}} = \begin{bmatrix} 1/m & 0 \\ 0 & m \end{bmatrix} \begin{bmatrix} A & B \\ C & D \end{bmatrix} = \begin{bmatrix} A/m & B/m \\ mC & mD \end{bmatrix}, \qquad \text{(B.7)}$$

where $m$ is a real number that should more or less correspond to the magnification of the system. If the imaginary part of the argument of the first $Q$-operator, on the right hand side in (B.5) is positive, it has the potential to cause computational issues due to large real values in the exponent. It is always possible to cancel the imaginary part by choosing

$$m = \text{Re}(A) - \text{Re}(B)\frac{\text{Im}(A)}{\text{Im}(B)} \qquad \text{(B.8)}$$

When the microscope is in focus, i.e. when $\text{Re}(B) = 0$, this reduces to $m = \text{Re}(A)$. It is important to note that when $\text{Re}(B)$ is zero, even small deviations from (B.8) will cause the algorithm to fail.

## B.3 Calculating aperture and defocus from the complex RTM parameters

The numerical aperture can by estimated using Gaussian beam propagation [40], but also by considering (B.2), with a $\delta$-function as input. Doing so results in a Gaussian output function with root mean square parameter $\sqrt{\text{Im}\left(\frac{B}{Dk}\right)}$, which corresponds to

$$\sigma_{\text{N.A.}}^2 = \frac{\mathcal{M}^2}{2k}\text{Im}\left(\frac{D}{B}\right) \qquad \text{(B.9)}$$

where $\mathcal{M}$ is the magnification of the system. The defocus distance can be calculated from the RTM by taking the real part of (2.32)

$$d = \text{Re}\left(\frac{B}{A}\right). \qquad \text{(B.10)}$$

## B.4 Simulation results

Figure B.1 demonstrates that lateral chromatic aberration is accounted for with this method. The sample object is a hexagonal grid of circular holes. The images
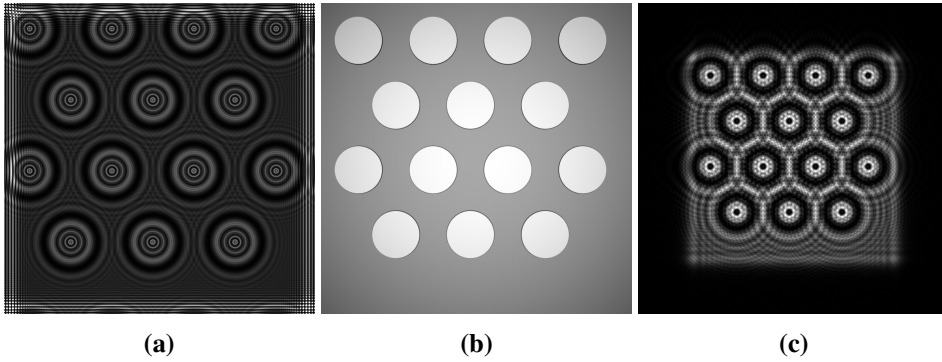
<div align="center">(a)                    (b)                    (c)</div>

**Figure B.1:** Demonstaration of scaling of defocused images. The values of $\alpha$ was 0.95, 1, and 1.2 in (a), (b), and (c), respectively, with $E_0 = 17$ keV.

show simulations results where $m$ have been selected to properly scale the in-focus image shown in B.1(b). Figure B.1(a), and B.1(c) shows the same system, but defocused by choosing lower and higher photon energy, respectively, relative to B.1(b). This may be utilized to evaluate the severity of lateral chromatic aberration.

Longitudinal chromatic aberration is also evident in the images, as near field fringes are plainly visible. The defocus distances were $d = 2.5$ cm and $d = -8.5$ cm in B.1(a) and B.1(a), respectively.

In B.1(a) it can be seen that in the case of magnification, the periphery of the original image will disappear over the boarders of the numerical field of view and reappear on the opposite side, giving rise to interference fringes. This should be cropped away in the final result.

It is possible simulate the effect of objects placed in the aperture plane by modulating with the complex transmission function of that object, after the first Fourier transform in (B.6) have been applied. Lens aberrations, physical aperture stops, etc. can easily be simulated this way.

Figure B.2 demonstrates the ability to evaluate vignetting effects caused by both a combination of the Gaussian and the geometrical aperture. The parameters for the objective CRL corresponded to 100 Si lenslets with $R = 5$ $\mu$m, $T = 125$ $\mu$m, and $R_0 = 25$ $\mu$m. These parameters are similar to the one presented suggested by Simons et al. [72]. An opaque circular, 50 $\mu$m diameter aperture was inserted in the aperture plane to represent the geometrical aperture. As expected, the field of view is largest when $g$ is chosen according to (3.24), and can be several times larger than the physical lens aperture. Fringing related to the aperture stop can be seen
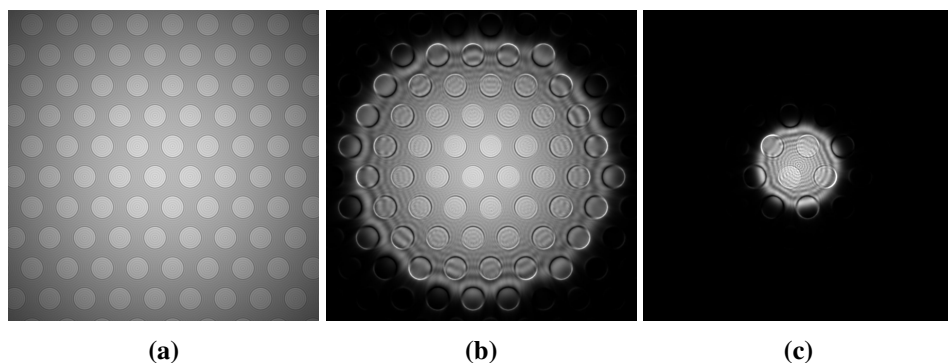
**(a)**                **(b)**                **(c)**

**Figure B.2:** Standard monochromatic imaging. The sample object is a 3 $\mu$m thick sheet of copper with circular holes with diameter 2.6 $\mu$m, spaced 4 $\mu$m between hole centres. The simulation was performed on a $2048 \times 2048$ pixel grid.

in the periphery of image B.2(b) and B.2(c). The exact appearence of the fringes depends on the sharpness of the aperture edge. In this simulation, a Gaussian blur of 50 nm r.m.s. was applied to the aperture stop, mainly to avoid aliasing.

It is also possible to simulate other microscopy techniques, such as differential interference contrast[17], spiral phase contrast[29], or Zernike phase contrast[87]. Figure B.3(b) demonstrates a simulation of Zernike phase contrast with a monochromatic beam. The phase element was a 10 $\mu$m diameter quarter wave plate inserted in the aperture plane. A concern when it comes to ZPC with a pink beam is that the chromaticism of the condenser could cause loss of ZPC for parts of the bandwidth. The effect of severe longitudinal misalignment of the source image, with respect to the phase element, can be seen in Figure B.3(a) and B.3(c). A projection image of the phase object appears when $g$ is too far away from its ideal value. ZPC is present inside the projection image, while only faint absorption contrast is visible outside it. A concern when it comes to ZPC with a pink beam is that the chromaticism of the condenser could cause loss of ZPC for parts of the bandwidth. Figure B.4 shows the results of a pink beam ZPC simulation, using 1.5% bandwidth. The image was simulated by adding (with appropriate weighting) images formed at 60 different energies. The convergence was assumed to be produced by a CRL condenser, and the value of $g$ was changed for each energy to reflect the energy dependence of the condenser focal length. The objective and condenser lens consisted of 90 and 32 beryllium lenslets, respectively, each with $R = 50\,\mu$m and $T = 1.6$ mm. The photon energy was $E = 17$ keV. No projection image can be seen in the image with these parameters.
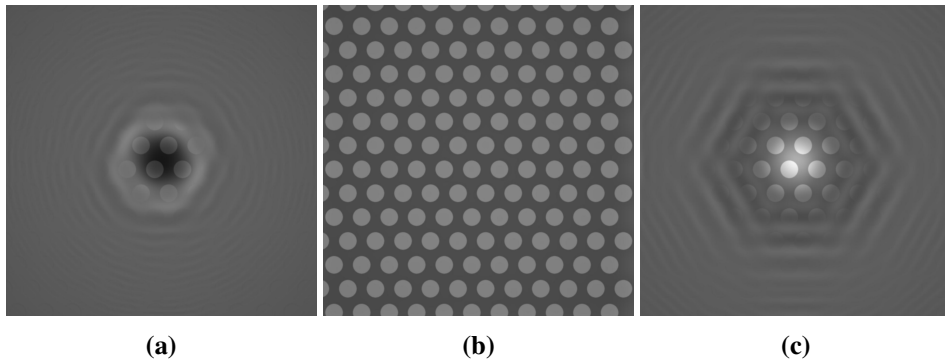
**Figure B.3:** Monochromatic ZPC with perfect non-absorbing quarter wave plate. The values of $g$ that were used were $g = \infty$, $g = g_{\text{ideal}}$, and $g = 0.65g_{\text{ideal}}$ for (a), (b), and (c), respectively. The sample object is as in Figure B.2, differing only in that the material is Beryllium rather than copper.

Some distance from the center of the star , where the spokes are thicker, the shade-off effect described in 5.2 becomes visible. This illustrates another point that can be evaluated with this type of simulation.
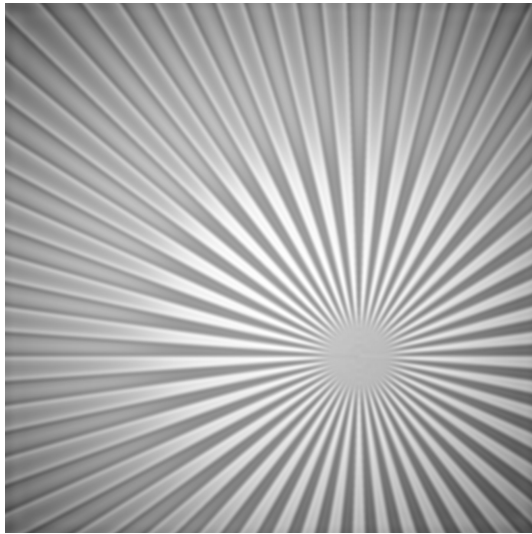
**Figure B.4:** Pink beam ZPC with non-absorbing quarter wave plate. The sample object is
as a Siemens star pattern with refractive indices corresponding to that of Al and Si.

# Bibliography

[1] J. Als-Nielsen, M. Altarelli, J. Baruchel, R. Currat, B. Fåk, A. Fontaine, V. T. Forsyth, A. Freund, G. Krill, M. Lambert, G. McIntyre, F. Mezei, J. Morse, J. Pannetier, D. Raoux, R. Scherm, M. Schlenker, G. Schmahl, C. Williams, and H. Zabel. *Neutron And Synchrotron Radiation For Condensed Matter Studies, Volume I: Theory, Instruments And Methods*, book section 2, pages 37–77. Springer and Les Editions de Physique, 1993. doi: citeulike-article-id:3727344.

[2] Jens Als-Nielsen and Des McMorrow. *Elements of Modern X-ray Physics*, book section 2, pages 29–68. John Wiley & Sons, Inc., 2011. ISBN 9781119998365. doi: 10.1002/9781119998365.biblio. URL `http://dx.doi.org/10.1002/9781119998365.biblio`.

[3] Jens Als-Nielsen and Des McMorrow. *Elements of Modern X-ray Physics*, book section 3, pages 69–112. John Wiley & Sons, Inc., 2011. ISBN 9781119998365. doi: 10.1002/9781119998365.biblio. URL `http://dx.doi.org/10.1002/9781119998365.biblio`.

[4] Jens Als-Nielsen and Des McMorrow. *Elements of Modern X-ray Physics*, book section 6, pages 207–239. John Wiley & Sons, Inc., 2011. ISBN 9781119998365. doi: 10.1002/9781119998365.biblio. URL `http://dx.doi.org/10.1002/9781119998365.biblio`.

[5] U. W. Arndt and D. J. Gilmore. X-ray television area detectors for macromolecular structural studies with synchrotron radiation sources. *Journal of Applied Crystallography*, 12(Feb):1–9, 1979. ISSN 0021-8898. doi: Doi10.1107/S0021889879011663.

[6] M. Asta, C. Beckermann, A. Karma, W. Kurz, R. Napolitano, M. Plapp,

G. Purdy, M. Rappaz, and R. Trivedi. Solidification microstructures and solid-state parallels: Recent developments, future directions. *Acta Materialia*, 57(4):941–971, 2009. ISSN 1359-6454. doi: 10.1016/j.actamat.2008.10.020.

[7] S. A. Belyakov, J. W. Xian, K. Sweatman, T. Nishimura, T. Akaiwa, and C. M. Gourlay. Influence of bismuth on the solidification of sn-0.7cu-0.05ni-xbi/cu joints. *Journal of Alloys and Compounds*, 701:321–334, 2017. ISSN 0925-8388. doi: 10.1016/j.jallcom.2016.12.404.

[8] C. Bergemann, H. Keymeulen, and J. F. van der Veen. Focusing x-ray beams to nanometer dimensions. *Physical Review Letters*, 91(20), 2003. ISSN 0031-9007. doi: ARTN20480110.1103/PhysRevLett.91.204801.

[9] Max Born and Emil Wolf. *Principles of Optics*, book section 1, pages 1–70. Pergamon, 1980. ISBN 978-0-08-026482-0. doi: http://dx.doi.org/10.1016/B978-0-08-026482-0.50008-6. URL http://www.sciencedirect.com/science/article/pii/B9780080264820500086.

[10] Max Born and Emil Wolf. *Principles of Optics*, book section 10, pages 554–632. Pergamon, 1980. ISBN 978-0-08-026482-0. doi: http://dx.doi.org/10.1016/B978-0-08-026482-0.50008-6. URL http://www.sciencedirect.com/science/article/pii/B9780080264820500086.

[11] Max Born and Emil Wolf. *Principles of Optics*, book section 3, pages 116–141. Pergamon, 1980. ISBN 978-0-08-026482-0. doi: http://dx.doi.org/10.1016/B978-0-08-026482-0.50008-6. URL http://www.sciencedirect.com/science/article/pii/B9780080264820500086.

[12] Max Born and Emil Wolf. *Principles of Optics*, book section 9, pages 517–553. Pergamon, 1980. ISBN 978-0-08-026482-0. doi: http://dx.doi.org/10.1016/B978-0-08-026482-0.50008-6. URL http://www.sciencedirect.com/science/article/pii/B9780080264820500086.

[13] R. N. Bracewell and A. C. Riddle. Inversion of fan-beam scans in radio astronomy. *Astrophysical Journal*, 150(2p1):427–+, 1967. ISSN 0004-637x. doi: Doi10.1086/149346.

[14] A. E. Burgess. The rose model, revisited. *Journal of the Optical Society of America a-Optics Image Science and Vision*, 16(3):633–646, 1999. ISSN 0740-3232. doi: Doi10.1364/Josaa.16.000633.

[15] W. H. Carter and E. Wolf. Coherence and radiometry with quasihomogeneous planar sources*. *Journal of the Optical Society of America*, 67(6):785–796, 1977. doi: 10.1364/JOSA.67.000785.

[16] D. Casari, W. U. Mirihanage, K. V. Falch, I. G. Ringdalen, J. Friis, R. Schmid-Fetzer, D. Zhao, Y. Li, W. H. Sillekens, and R. H. Mathiesen. alpha-mg primary phase formation and dendritic morphology transition in solidification of a mg-nd-gd-zn-zr casting alloy. *Acta Materialia*, 116:177–187, 2016. ISSN 1359-6454. doi: 10.1016/j.actamat.2016.06.035.

[17] C. Chang, A. Sakdinawat, P. Fischer, E. Anderson, and D. Attwood. Single-element objective lens for soft x-ray differential interference contrast microscopy. *Optics Letters*, 31(10):1564–1566, 2006. ISSN 0146-9592. doi: Doi10.1364/Ol.31.001564.

[18] W. L. Chao, B. D. Harteneck, J. A. Liddle, E. H. Anderson, and D. T. Attwood. Soft x-ray microscopy at a spatial resolution better than 15nm. *Nature*, 435(7046):1210–1213, 2005. ISSN 0028-0836. doi: 10.1038/nature03719.

[19] J. Chen, W. J. Li, Y. J. Liu, Z. B. Yue, J. P. Tian, L. H. Liu, Y. Xiong, G. Liu, C. R. Wane, Z. Y. Wu, H. G. Yu, and Y. C. Tian. Fresnel zone-plate based x-ray microscopy in zernike phase contrast with sub-50 nm resolution at nsrl. *9th International Conference on X-Ray Microscopy*, 186, 2009. ISSN 1742-6588. doi: Artn01200510.1088/1742-6596/186/1/012005.

[20] J. Cho, S. Mallampati, H. Schoeller, L. Yin, and D. Shaddock. Developments of bi-sb-cu alloys as a high-temperature pb-free solder. *2015 Ieee 65th Electronic Components and Technology Conference (Ectc)*, pages 1251–1256, 2015. ISSN 0569-5503.

[21] CXRO. X-ray interactions with matter. url: http://henke.lbl.gov/optical_constants/. [Accessed 1 January]. URL http://henke.lbl.gov/optical\_constants/.

[22] C. G. Darwin. Xxxiv. the theory of x-ray reflexion. *Philosophical Magazine Series 6*, 27(158):315–333, 1914. ISSN 1941-5982. doi: 10.1080/14786440208635093.

[23] V. P. Dhamgaye, M. K. Tiwari, K. J. S. Sawhney, and G. S. Lodha. Microfocussing of synchrotron x-rays using x-ray refractive lens developed at indus-2 deep x-ray lithography beamline. *Pramana-Journal of Physics*, 83 (1):119–129, 2014. ISSN 0304-4289. doi: 10.1007/s12043-014-0757-y.

[24] C. J. Edgcombe. Imaging by zernike phase plates in the tem. *Ultramicroscopy*, 167:57–63, 2016. ISSN 0304-3991. doi: 10.1016/j.ultramic.2016.05.003.

[25] K. V. Falch, C. Detlefs, A. Snigirev, and R. Mathiesen. Analytical transmission cross-coefficients for pink beam x-ray microscopy based on compound refractive lenses. *Ultramicroscopy*, To be submitted, 2016.

[26] K. V. Falch, M. Lyubomirskij, D. Casari, C. Detlefs, A. Snigirev, I. Snigireva, M. Di Michiel, and R. Mathiesen. Zernike phase contrast in high-energy x-ray transmission microscopy based on refractive optics. *Ultramicroscopy*, Under Review, 2016.

[27] Ken Vidar Falch, Daniele Casari, Marco Di Michiel, Carsten Detlefs, Anatoly Snigireva, Irina Snigireva, Veijo Honkimäki, and Ragnvald H. Mathiesen. In situ hard x-ray transmission microscopy for material science. *Journal of Materials Science*, 2016. ISSN 1573-4803. doi: 10.1007/s10853-016-0643-8.

[28] Ken Vidar Falch, Carsten Detlefs, Marco Di Michiel, Irina Snigireva, Anatoly Snigirev, and Ragnvald H. Mathiesen. Correcting lateral chromatic aberrations in non-monochromatic x-ray microscopy. *Applied Physics Letters*, 109 (5):054103, 2016. doi: doi:http://dx.doi.org/10.1063/1.4960193.

[29] S. Furhapter, A. Jesacher, S. Bernet, and M. Ritsch-Marte. Spiral phase contrast imaging in microscopy. *Optics Express*, 13(3):689–694, 2005. ISSN 1094-4087. doi: Doi10.1364/Opex.13.000689.

[30] Joseph W Goodman. *Introduction to Fourier optics*, book section 5. Roberts & company, 2005. ISBN 0974707724.

[31] Joseph W Goodman. *Statistical optics*, book section 5, pages 152–227. John Wiley & Sons, 2015. ISBN 1119009456.

[32] C. M. Gourlay, S. A. Belyakov, Z. L. Ma, and J. W. Xian. Nucleation and growth of tin in pb-free solder joints. *Jom*, 67(10):2383–2393, 2015. ISSN 1047-4838. doi: 10.1007/s11837-015-1582-6.

[33] Heinz Graafsma and Thierry Martin. *DETECTORS FOR SYNCHROTRON TOMOGRAPHY*, book section 10. Oxford University Press, Oxford, 2008. ISBN 9780199213245. doi: 10.1093/acprof:oso/9780199213245.003.0010. URL `http://www.oxfordscholarship.com/view/10.1093/acprof:oso/9780199213245.001.0001/acprof-9780199213245-chapter-10`.

[34] G.C. Holst. *CCD arrays, cameras, and displays*, book section 4. JCD Publishing, 1998. ISBN 9780964000049. URL `https://books.google.no/books?id=QyVLAQAAIAAJ`.

[35] H. H. Hopkins. On the diffraction theory of optical images. *Proceedings of the Royal Society of London Series a-Mathematical and Physical Sciences*, 217(1130):408–432, 1953. doi: DOI10.1098/rspa.1953.0071.

[36] K. A. Jackson and J. D. Hunt. Lamellar and rod eutectic growth. *Transactions of the Metallurgical Society of Aime*, 236(8):1129–1142, 1966. ISSN 0543-5722.

[37] Avinash C. Kak and Malcolm Slaney. *Principles of computerized tomographic imaging*, book section 3, pages 49–110. Society for Industrial and Applied Mathematics, Philadelphia, 2001. ISBN 9780898719277 0898719275. URL `http://www.books24x7.com/marc.asp?bookid=23044`.

[38] A. Koch, C. Raven, P. Spanne, and A. Snigirev. X-ray imaging with sub-micrometer resolution employing transparent luminescent screens. *Journal of the Optical Society of America a-Optics Image Science and Vision*, 15(7): 1940–1951, 1998. ISSN 0740-3232. doi: Doi10.1364/Josaa.15.001940.

[39] F. J. Koch, C. Detlefs, T. J. Schroter, D. Kunka, A. Last, and J. Mohr. Quantitative characterization of x-ray lenses from two fabrication techniques with grating interferometry. *Optics Express*, 24(9):9168–9177, 2016. ISSN 1094-4087. doi: 10.1364/Oe.24.009168.

[40] H. Kogelnik. On propagation of gaussian beams of light through lenslike media including those with a loss or gain variation. *Applied Optics*, 4(12): 1562–&, 1965. ISSN 0003-6935. doi: Doi10.1364/Ao.4.001562.

[41] V. G. Kohn. On the theory of x-ray refractive optics: Exact solution for a parabolic medium. *Jetp Letters*, 76(10):600–603, 2002. ISSN 0021-3640. doi: Doi10.1134/1.1541043.

[42] V. G. Kohn. An exact theory of imaging with a parabolic continuously refractive x-ray lens. *Journal of Experimental and Theoretical Physics*, 97(1): 204–215, 2003. ISSN 1063-7761. doi: Doi10.1134/1.1600812.

[43] B. Lengeler, C. G. Schroer, B. Benner, T. F. Gunzler, M. Kuhlmann, J. Tummler, A. S. Simionovici, M. Drakopoulos, A. Snigirev, and I. Snigireva. Parabolic refractive x-ray lenses: a breakthrough in x-ray optics. *Nuclear Instruments & Methods in Physics Research Section a-Accelerators*

*Spectrometers Detectors and Associated Equipment*, 467:944–950, 2001. ISSN 0168-9002. doi: Doi10.1016/S0168-9002(01)00531-9.

[44] P. Magnin and W. Kurz. An analytical model of irregular eutectic growth and its application to fe-c. *Acta Metallurgica*, 35(5):1119–1128, 1987. ISSN 0001-6160. doi: Doi10.1016/0001-6160(87)90059-9.

[45] P. Magnin and R. Trivedi. Eutectic growth - a modification of the jackson and hunt theory. *Acta Metallurgica Et Materialia*, 39(4):453–467, 1991. ISSN 0956-7151. doi: Doi10.1016/0956-7151(91)90114-G.

[46] S. Matsuyama, Y. Emi, H. Kino, Y. Kohmura, M. Yabashi, T. Ishikawa, and K. Yamauchi. Achromatic and high-resolution full-field x-ray microscopy based on total-reflection mirrors. *Optics Express*, 23(8):9746–9752, 2015. ISSN 1094-4087. doi: 10.1364/Oe.23.009746.

[47] W. U. Mirihanage, K. V. Falch, I. Snigireva, A. Snigirev, Y. J. Li, L. Arnberg, and R. H. Mathiesen. Retrieval of three-dimensional spatial information from fast in situ two-dimensional synchrotron radiography of solidification microstructure evolution. *Acta Materialia*, 81:241–247, 2014. ISSN 1359-6454. doi: http://dx.doi.org/10.1016/j.actamat.2014.08.016.

[48] T. Narayanan. High brilliance small-angle x-ray scattering applied to soft matter. *Current Opinion in Colloid & Interface Science*, 14(6):409–415, 2009. ISSN 1359-0294. doi: 10.1016/j.cocis.2009.05.005.

[49] M. Nazarathy and J. Shamir. Fourier optics described by operator algebra. *Journal of the Optical Society of America*, 70(2):150–159, 1980. ISSN 0030-3941. doi: Doi10.1364/Josa.70.000150.

[50] M. Nazarathy and J. Shamir. 1st-order optics - a canonical operator representation - lossless systems. *Journal of the Optical Society of America*, 72(3): 356–364, 1982. ISSN 0030-3941. doi: Doi10.1364/Josa.72.000356.

[51] M. Nazarathy and J. Shamir. 1st-order optics - operator representation for systems with loss or gain. *Journal of the Optical Society of America*, 72(10): 1398–1408, 1982. ISSN 0030-3941. doi: Doi10.1364/Josa.72.001398.

[52] M. Nazarathy, J. Shamir, and A. Hardy. Nonideal phase-conjugate resonators - a canonical operator analysis. *Journal of the Optical Society of America*, 73 (5):587–593, 1983. ISSN 0030-3941. doi: Doi10.1364/Josa.73.000587.

[53] M. Nazarathy, A. Hardy, and J. Shamir. Misaligned 1st-order optics - canonical operator-theory. *Journal of the Optical Society of America a-Optics*

*Image Science and Vision*, 3(9):1360–1369, 1986. ISSN 0740-3232. doi: Doi10.1364/Josaa.3.001360.

[54] E. Nazaretski, W. Xu, N. Bouet, J. Zhou, H. Yan, X. Huang, and Y. S. Chu. Development and characterization of monolithic multilayer laue lens nanofocusing optics. *Applied Physics Letters*, 108(26), 2016. ISSN 0003-6951. doi: Artn26110210.1063/1.4955022.

[55] E. Nazaretski, H. Yan, K. Lauer, X. Huang, W. Xu, S. Kalbfleisch, Hui Yan, Li Li, N. Bouet, J. Zhou, D. Shu, R. Conley, and Y. S. Chu. Nm-scale spatial resolution x-ray imaging with mll nanofocusing optics: Instrumentational requirements and challenges. *AIP Conference Proceedings*, 1764(1):040001, 2016. doi: doi:http://dx.doi.org/10.1063/1.4961143.

[56] U. Neuhausler, G. Schneider, W. Ludwig, M. A. Meyer, E. Zschech, and D. Hambach. X-ray microscopy in zernike phase contrast mode at 4 kev photon energy with 60 nm resolution. *Journal of Physics D-Applied Physics*, 36(10a):A79–A82, 2003. ISSN 0022-3727. doi: PiiS0022-3727(03) 60188-9Doi10.1088/0022-3727/36/10a/316.

[57] S. Niese, P. Krueger, A. Kubec, S. Braun, J. Patommel, C. G. Schroer, A. Leson, and E. Zschech. Full-field x-ray microscopy with crossed partial multilayer laue lenses. *Optics Express*, 22(17):20008–20013, 2014. ISSN 1094-4087. doi: 10.1364/Oe.22.020008.

[58] NIST. X-ray mass attenuation coefficients. url: http://physics.nist.gov/PhysRefData/XrayMassCoef/tab3.html. [Accessed 1 January]. URL http://physics.nist.gov/PhysRefData/ XrayMassCoef/tab3.html.

[59] G. A. Ozin and S. M. Yang. The race for the photonic chip: Colloidal crystal assembly in silicon wafers. *Advanced Functional Materials*, 11(2):95–104, 2001. ISSN 1616-301x. doi: Doi10.1002/1616-3028(200104)11:2<95:: Aid-Adfm95>3.0.Co;2-O.

[60] D. M. Paganin. *Coherent X-Ray Optics*, book section 1, pages 1–63. Oxford University Press, 2006. doi: 10.1093/acprof:oso/9780198567288.001.0001.

[61] D. M. Paganin. *Coherent X-Ray Optics*, book section 2, pages 64–135. Oxford University Press, 2006. doi: 10.1093/acprof:oso/9780198567288.001. 0001.

[62] D. M. Paganin. *Coherent X-Ray Optics*, book section 3, pages 136–227. Oxford University Press, 2006. doi: 10.1093/acprof:oso/9780198567288. 001.0001.

[63] J. M. Park, T. E. Kim, S. W. Sohn, D. H. Kim, K. B. Kim, W. T. Kim, and J. Eckert. High strength ni-zr binary ultrafine eutectic-dendrite composite with large plastic deformability. *Applied Physics Letters*, 93(3):031913, 2008. ISSN 0003-6951. doi: Artn03191310.1063/1.2952755.

[64] L. G. Parratt. Surface studies of solids by total reflection of x-rays. *Physical Review*, 95(2):359–369, 1954. ISSN 0031-899x. doi: DOI10.1103/PhysRev. 95.359.

[65] M. V. Petoukhov and D. I. Svergun. Applications of small-angle x-ray scattering to biomacromolecular solutions. *International Journal of Biochemistry & Cell Biology*, 45(2):429–437, 2013. ISSN 1357-2725. doi: 10.1016/j.biocel.2012.10.017.

[66] A. Rose. The sensitivity performance of the human eye on an absolute scale. *Journal of the Optical Society of America*, 38(2):196–208, 1948. ISSN 0030-3941. doi: Doi10.1364/Josa.38.000196.

[67] P. Schall, I. Cohen, D. A. Weitz, and F. Spaepen. Visualization of dislocation dynamics in colloidal crystals. *Science*, 305(5692):1944–1948, 2004. ISSN 0036-8075. doi: DOI10.1126/science.1102186.

[68] P. Schall, I. Cohen, D. A. Weitz, and F. Spaepen. Visualizing dislocation nucleation by indenting colloidal crystals. *Nature*, 440(7082):319–323, 2006. ISSN 0028-0836. doi: 10.1038/nature04557.

[69] C. G. Schroer and B. Lengeler. Focusing hard x rays to nanometer dimensions by adiabatically focusing lenses. *Physical Review Letters*, 94(5), 2005. ISSN 0031-9007. doi: ARTN05480210.1103/PhysRevLett.94.054802.

[70] C. G. Schroer, B. Lengeler, B. Benner, T. F. Gunzler, M. Kuhlmann, A. S. Simionovici, S. Bohic, M. Drakopoulos, A. Snigirev, I. Snigireva, and W. H. Schroder. Microbeam production using compound refractive lenses: Beam characterization and applications. *X-Ray Micro- and Nano-Focusing: Applications and Techniques Ii*, 4499:52–63, 2001. ISSN 0277-786x. doi: Doi10.1117/12.450222.

[71] F. Seiboth, A. Schropp, R. Hoppe, V. Meier, J. Patommel, H. J. Lee, B. Nagler, E. C. Galtier, B. Arnold, U. Zastrau, J. B. Hastings, D. Nilsson, F. Uhlen, U. Vogt, H. M. Hertz, and C. G. Schroer. Focusing xfel sase pulses

by rotationally parabolic refractive x-ray lenses. *22nd International Congress on X-Ray Optics and Microanalysis*, 499, 2014. ISSN 1742-6588. doi: Artn01200410.1088/1742-6596/499/1/012004.

[72] H. Simons, F. Stohr, J. Michael-Lindhard, F. Jensen, O. Hansen, C. Detlefs, and H. F. Poulsen. Full-field hard x-ray microscopy with interdigitated silicon lenses. *Optics Communications*, 359:460–464, 2016. ISSN 0030-4018. doi: 10.1016/j.optcom.2015.09.103.

[73] A. Snigirev, I. Snigireva, M. Lyubomirskiy, V. Kohn, V. Yunkin, and S. Kuznetsov. X-ray multilens interferometer based on si refractive lenses. *Optics Express*, 22(21):25842–25852, 2014. ISSN 1094-4087. doi: 10.1364/ Oe.22.025842.

[74] I. Snigireva, G. B. M. Vaughan, and A. Snigirev. High-energy nanoscale-resolution x-ray microscopy based on refractive optics on a long beamline. *10th International Conference on X-Ray Microscopy*, 1365:188–191, 2011. ISSN 0094-243x.

[75] I. I. Snigireva, V. G. Kohn, and A. A. Snigirev. Hard x-ray focusing with extremely long compound refractive lens. *Design and Microfabrication of Novel X-Ray Optics Ii*, 5539:218–225, 2004. ISSN 0277-786x. doi: 10. 1117/12.564269.

[76] M. Stanton, W. Phillips, Y. L. Li, and K. Kalata. The detective quantum efficiency of ccd and vidicon-based detectors for x-ray crystallographic applications. *Journal of Applied Crystallography*, 25:638–645, 1992. ISSN 0021-8898. doi: Doi10.1107/S0021889892005211.

[77] K. Suganuma. Advances in lead-free electronics soldering. *Current Opinion in Solid State & Materials Science*, 5(1):55–64, 2001. ISSN 1359-0286. doi: Doi10.1016/S1359-0286(00)00036-X.

[78] M. Sugawara, M. Kondo, S. Yamazaki, and K. Nakajima. Exact determination of superlattice structures by small-angle x-ray-diffraction method. *Applied Physics Letters*, 52(9):742–744, 1988. ISSN 0003-6951. doi: Doi10.1063/1.99342.

[79] A. Takeuchi, K. Uesugi, and Y. Suzuki. Zernike phase-contrast x-ray microscope with pseudo-kohler illumination generated by sectored (polygon) condenser plate. *9th International Conference on X-Ray Microscopy*, 186, 2009. ISSN 1742-6588. doi: Artn01202010.1088/1742-6596/186/1/012020.

[80] S. Terentyev, V. Blank, S. Polyakov, S. Zholudev, A. Snigirev, M. Polikarpov, T. Kolodziej, J. Qian, H. Zhou, and Y. Shvyd'ko. Parabolic single-crystal diamond lenses for coherent x-ray imaging. *Applied Physics Letters*, 107 (11), 2015. ISSN 0003-6951. doi: Artn11110810.1063/1.4931357.

[81] J. H. J. Thijssen, A. V. Petukhov, D. C. 'T Hart, A. Imhof, C. H. M. van der Werf, R. E. I. Schropp, and A. van Blaaderen. Characterization of photonic colloidal single crystals by microradian x-ray diffraction. *Advanced Materials*, 18(13):1662–1666, 2006. ISSN 0935-9648. doi: 10.1002/adma.200502732.

[82] G. B. M. Vaughan, J. P. Wright, A. Bytchkov, M. Rossat, H. Gleyzolle, I. Snigireva, and A. Snigirev. X-ray transfocators: focusing devices based on compound refractive lenses. *Journal of Synchrotron Radiation*, 18:125–133, 2011. ISSN 0909-0495. doi: 10.1107/S0909049510044365.

[83] J. W. Xian, S. A. Belyakov, M. Ivier, K. Nogita, H. Yasuda, and C. M. Gourlay. Cu6sn5 crystal growth mechanisms during solidification of electronic interconnections. *Acta Materialia*, 126:540–551, 2017. ISSN 1359-6454. doi: 10.1016/j.actamat.2016.12.043.

[84] G. C. Yin, Y. F. Song, M. T. Tang, F. R. Chen, K. S. Liang, F. W. Duewer, M. Feser, W. B. Yun, and H. P. D. Shieh. 30 nm resolution x-ray imaging at 8 kev using third order diffraction of a zone plate lens objective in a transmission microscope. *Applied Physics Letters*, 89(22), 2006. ISSN 0003-6951. doi: Artn22112210.1063/1.2397483.

[85] J. X. You, L. L. Wang, Z. J. Wang, J. J. Li, J. C. Wang, X. Lin, and W. D. Huang. Interfacial undercooling in solidification of colloidal suspensions: analyses with quantitative measurements. *Scientific Reports*, 6:28434, 2016. ISSN 2045-2322. doi: ARTN2843410.1038/srep28434.

[86] F. Zernike. The concept of degree of coherence and its application to optical problems. *Physica*, 5(8):785–795, 1938. ISSN 0031-8914. doi: http://dx.doi.org/10.1016/S0031-8914(38)80203-2.

[87] F. Zernike. Phase contrast, a new method for the microscopic observation of transparent objects. *Physica*, 9(7):686–698, 1942. ISSN 0031-8914. doi: http://dx.doi.org/10.1016/S0031-8914(42)80035-X.